Ordering of Nanoparticles by Wrinkle-Assisted Self-Assembly

Controlling Plasmonic Coupling Effects

Dissertation

zur Erlangung des akademischen Grades eines Doktors der Naturwissenschaften (Dr. rer. nat.) im Fach Chemie der Fakultät für Biologie, Chemie und Geowissenschaften der Universität Bayreuth

vorgelegt von

Alexandra Schweikart

geboren in Schramberg

Bayreuth im Januar 2011

Die vorliegende Arbeit wurde in der Zeit von Dezember 2007 bis Januar 2011 am Lehrstuhl Physikalische Chemie II unter der Betreuung von Prof. Dr. Andreas Fery an der Universität Bayreuth angefertigt.

Vollständiger Abdruck der von der Fakultät Biologie, Chemie und Geowissenschaften der Universität Bayreuth genehmigten Dissertation zur Erlangung des akademischen Grades eines Doktors der Naturwissenschaften (Dr. rer. nat.).

Dissertation eingereicht: 18.01.2011

Zulassung durch die Prüfungskommission: 19.01.2011

Wissenschaftliches Kolloquium: 03.05.2011

Amtierender Dekan: Prof. Dr. Stephan Clemens

Prüfungsausschuss:

Prof. Dr. Andreas Fery	(Erstgutachter)
Prof. Dr. Thomas Scheibel	(Zweitgutachter)
Prof. Josef Breu	(Vorsitz)
Prof. Matthias Schmidt	

Am besten scheinen sich die Menschen zu konzentrieren, wenn sie ein bisschen stärker als gewöhnlich gefordert werden und wenn sie mehr als gewöhnlich geben können. Werden sie zu wenig gefordert, langweilen sie sich, sind sie den Anforderungen nicht gewachsen, werden sie ängstlich. Das Fließen ereignet sich in dem heiklen Bereich zwischen Langeweile und Angst.

Aus „Flow“ von *Mihály Csíkszentmihályi,*

Psychologe an der Universität Chicago

Contents

Chapter 1 Summary

Structures of spatial scale between 10Å and 1000Å are known as nanomaterials and have attracted immense interest over the last decades (Nobel Prize in physics in 2010 was awarded for the nanomaterial graphene). Materials within this scale show a large surface-to-volume ratio and amplify surface-related properties. Governing and manipulating material on this almost atomic level is one of the most active fields in modern natural science. Nanoscale technology, such as some of the processes involved in steel production and painting, has been empirically utilized in human society for centuries, however, a scientific investigation of phenomena on this spatial scale only began in 1857 when Michael Faraday reported on the synthesis and colors of gold colloids. In 1959 interest in the nanoscale was stimulated by an American physicist, Richard Feynman, in his famous "There's plenty of room at the bottom" address, and the term nanotechnology first appeared in 1974 from the Japanese Norio Taniguchi. Since these pioneering works, thousands of publications have been focused on the synthesis, modification, properties and assembly of nanoparticles. Great progress has been attained in the preparation of nanoparticles of any desired size, shape and composition.

Metal nanoparticles are particularly attractive due to their spectacular size and shape dependent optical and electronic properties. Color variations of nanoparticle suspension for example arise from changes in the composition, size and shape of nanoparticles, as well as from the proximity of other metal nanoparticles. The average distances of nanoparticles in thin films influence the spectral features because of inter-nanoparticle coupling. These effects are often the result of changes in the so-called surface Plasmon resonance, the frequency at which conduction electrons oscillate in response to the alternating electric field. Provided nanoparticles form ordered arrays, they can additionally have unique and fascinating optical properties because of photonic band gap effects with potential applications such as detectors, circuits, light sources, polymeric opals or meta-materials.

The present work deals with the controlled placement of nanoparticles by physical constraints. Exact placement of nanoparticles allows for the control of the inter-nanoparticle distance and thus determines the coupling effects (here: Plasmon coupling) which arise upon interaction with electromagnetic radiation. Different coupling leads to different distance-

dependent signals and such substrates can serve as sensors if, for example, Raman spectroscopy is carried out for detection of the signal.

Currently, most templates are created using lithographic techniques. Particularly if structures on the sub-micron scale are desired, electron beam lithography has to be used which involves environmentally harmful etching processes. Within this work we show how *controlled wrinkling* of a thin rigid film on a soft, elastomeric substrate, can be used as an alternative to fabricate nano-templates without using any lithography. As a substrate, a silicon elastomer poly (dimethylsiloxane) (PDMS) was used. Upon stretching such substrates uniaxially, an enlarged surface was exposed to oxygen plasma and converted to silica by oxidation. After releasing the strain, periodic wrinkles appeared perpendicular to the applied strain. Under defined conditions, such wrinkles have a regular sinusoidal topology featuring a single dominant wavelength and amplitude. The formation process could easily be tuned by tuning the plasma exposure to generate periodically structured templates between few hundreds of nanometers and several microns.

In this work, wrinkled templates were tailored such that suitably sized nanoparticles could be arbitrarily assembled into a hierarchical structure by drying colloids out of suspension in a channel-like confinement offered by wrinkles in contact with a flat substrate. Using the same template geometry (same wavelength and amplitude of wrinkles) but different particle concentration of spherical polystyrene beads (r = 55nm) we found parallel particle-structures ranging from single parallel lines at low particle concentration to dense prismatic ridges at high particle concentration. The wavelength of the wrinkled template defined the spacing between the particle lines.

Moreover, we performed Monte Carlo (MC) computer simulations in collaboration with the theoretical physics department (*Prof. Dr. Matthias Schmidt* and *Dr. Andrea Fortini*) at the University of Bayreuth to assess the dominant driving forces during the assembly process. Be using MC, colloidal particle assemblies can be characterized in terms of their equilibrium configuration that minimizes the free energy. Simulations were performed on particles in a box delimited by a flat hard wall and a sinusoidal hard wall according to our experimental system. These simulations precisely predicted the exact assembled geometry in thermal equilibrium. Comparing results of simulation and experiment we found perfect agreement between the equilibrium structures. We discovered the confinement itself to be mainly responsible for the assembled morphology of nanoparticle, which makes the process independent of the detailed chemistry of particles.

In addition we obtained very similar structures with the same assembly strategy but using gold nanoparticles (r = 33 nm) instead of polymeric particles. We fabricated lines of gold nanoparticles assembled in a single file and lines two particles wide using similar particle concentration but different sizes of the confinement template. The different morphologies of the lines give rise to different optical signals as collective oscillation of conduction electrons result in different interaction with electromagnetic radiation. Surface Plasmon resonance due to Plasmon coupling between adjacent particles arises. Different morphology-dependent signals of nanoparticles in contact within the lines were detected by surface enhanced Raman spectroscopy (SERS).

The electromagnetic field was measured to be randomly distributed along the particle lines with strong enhancements at so-called hot spots located at gaps between neighboring nanoparticles. To confirm the measured signal we compared theoretical simulations using the finite-difference time-domain (FDTD) method and experimentally measured dark-field spectroscopy signal along differently shaped lines of particles within a collaboration with *Weihai Ni* and *Dr. Ramón Alvarez-Puebla* at the University of Vigo in Spain. Good agreement between theory and experiment indicated that indeed plasmonic coupling of the individual nanoparticles is responsible for the observed SERS effects: Using wrinkle-assisted self-assembly it is possible to control the organization of the colloidal particles on the substrate, with a consequent control over the formation of hot spots and the resulting SERS intensity. Such ordered multiplicities of hot spots give rise to quantitative SERS signals with high sensitivity which has applications as diverse as biological detectors, optical filters and sensors.

In addition, this work deals with chemical modification of the wrinkled structure to render it accessible to different solvents as PDMS tends to swell in organic solvents and suffers from poor mechanical stability. Additionally, wrinkles fabricated through a buckling instability of a stiff supported layer under compression are not tension free on the microscopic level and suffer from relaxation on a longer time scale. We introduce in this work two different methods to replicate wrinkles by molding. In micro thermoforming, the wrinkled surface was used as a mold (or caliber) to structure different kinds of polymers (polystyrene and poly (methylmethacrylate)) by pressing the originally wrinkled structure onto a ductile material which preserves the nanostructure after curing. The second methodology was carried out in collaboration with *PD. Dr. Kerstin Koch* and *Michael Bennemann* at the Nees institute in Bonn and employed a two-step molding process, where wrinkles were molded against wax and in a second step, the structured wax was cast against epoxy resin. Both methods revealed perfect

copies of the wrinkled original with high fidelity even at dimensions as small as a few hundred nanometers and hold no residual stresses because there is only one component. Wrinkles made of tough polymers are now accessible to various solvents which make them potential substrates for microfluidics.

In the last part of this work, wrinkles are used as stamps in so-called micro contact printing (μCP). In this technique, a structured elastomeric stamp is used to transfer a surface-active molecule out of solution to a flat substrate by mechanical contact. Patterns of different charge density can be created which have applications in the field of biosensors, diagnostic immunoassays and cell culturing. Traditionally, stamps for μCP are prepared by a two step process where a lithographically fabricated structured silicon master serves as mold. An elastomeric polymer is cast against the caliber and preserves the structure after curing and detaching. As already mentioned lithography is expensive and involves environmentally harmful etching processes. Within this work we introduce the one step wrinkling process to fabricate structured stamps. Even though the diversity of stamp geometries created by wrinkling is limited, the simplicity compared to lithographic techniques is evident. The process of wrinkle formation includes plasma oxidation, which renders the topmost surface hydrophilic. Therefore, charged macromolecules out of aqueous solution were adsorbed onto the surface. The coated relief structure was used as a stamp to transfer the molecules selectively from the elevated parts of the wrinkles to another flat, oppositely charged surface by means of μCP. The topography of the resulting pattern was characterized by Atomic Force Microscopy (AFM) imaging as alternating charged pattern of printed (elevated) and non-printed areas. By varying the geometry of the wrinkled stamp (amplitude and wavelength) we studied the limits in which successful μCP with wrinkles can be carried out. We found the limits for wavelength of the wrinkles below 355nm and amplitudes below 40nm at which the printed structure disappeared because material was transferred from the wrinkles' hills as well as from the bottom parts. The height of the transferred structure increase with increasing wavelength and amplitude of the wrinkles but tended to a limit of 6-7nm, even though the topology of the stamp increases. The smallest structure found in lateral dimensions was as small as 50nm, appearing as areas where no material was transferred.

Chapter 2 Zusammenfassung

Nanomaterialien bestehen aus Bausteinen, die zwischen 10Å und 1000Å groß sind, also von Einzelatomen bis hin zu einer Strukturgröße von 100nm. Völlig neuartige Eigenschaften entstehen bei Materialien dieser Größenordnung wegen des großen Oberfläche-zu-Volumen-Verhältnisses. Die Erforschung von Nanomaterialien hat sich in den letzten Jahrzehnten dank neuartiger, hochauflösender Messtechnik zu einem viel beachteten Gebiet entwickelt (Nobelpreis für Physik im Jahre 2010 für das Nanomaterial Graphen). Die gezielte Steuerung und Manipulation von Materie auf dieser Größenskala ist eine der großen Herausforderungen der modernen Naturwissenschaft. Ohne es zu wissen nutzten Menschen schon seit Jahrhunderten Nanotechnologie, beispielsweise in der Stahlproduktion und für Kolorierungen. Die wissenschaftliche Erforschung von Phänomenen auf der Nanoskala begann jedoch erst 1857 als Michel Faraday eine wissenschaftliche Studie über die Herstellung und die außergewöhnliche Farbe von kolloidalem Gold publizierte. Hundert Jahre danach, 1959 hielt der Amerikaner Richard Feynman seine berühmte Ansprache „There's plenty of room at the bottom", zu Deutsch „ganz Unten ist eine Menge Platz" und 1974 prägte der Japaner Norio Tanigucho den Begriff der Nanotechnologie. Seit diesen Pionierarbeiten wurden tausende von Studien veröffentlicht, die sich mit der Synthese, Modifikation, Eigenschaften und Anordnung von Nanopartikeln beschäftigen. Nanopartikel jeder vorstellbaren Größe, Form und Zusammensetzung konnten bereits synthetisiert und charakterisiert werden.

Metall-Nanopartikel sind besonders beliebte Forschungsobjekte da sie spektakuläre Größen- und formabhängige optische Eigenschaften besitzen. Die Farbe von Nanopartikel-Suspensionen zum Beispiel variiert mit verschiedener Größe, Gestalt oder Zusammensetzung der einzelnen Partikel. Dünne Nanopartikel-Filme zeigen unterschiedliche Farbmuster, je nachdem, in welchem Abstand die einzelnen Partikel zueinander angeordnet sind, da eine Kopplung zwischen den Partikeln stattfindet. Für diese Effekte sind Änderungen der sogenannten Oberflächenplasmonenresonanz verantwortlich. Sie bezeichnet diejenige Frequenz, bei der Leitungselektronen im elektromagnetischen Feld oszillieren.

Werden Nanopartikel in periodischen Strukturen angeordnet, können Effekte beobachtet werden, die als photonische Bandlückeneffekte bekannt sind. Solche Strukturen werden in Sensoren, Schaltungen, Lichtquellen, polymeren Opalen oder Meta-Materialien eingesetzt.

Die vorliegende Arbeit beschäftigt sich mit der Anordnung von Nanopartikeln mit Hilfe von strukturierten Oberflächen (Template). Template werden benutzt um Nanopartikel in kontrollierter Art und Weise auf Oberflächen anzuordnen. Damit wird es möglich, den Abstand zwischen einzelnen Nanopartikeln und somit die Kopplung zwischen den Partikeln (hier: Plasmon-Kopplung) zu kontrollieren. Durch die Kopplung entsteht ein Abstandsabhängiges Signal, welches als Indikator verwendet werden kann, wenn das Signal beispielsweise mittels Raman-Spektroskopie detektiert wird.

Momentan werden die meisten strukturierten Oberflächen mittels lithographischen Techniken hergestellt. Werden Strukturen auf der Nanoskala gewünscht, muss Elektronenstrahl-Lithographie verwendet werden. Dabei kommen Ätzverfahren zum Einsatz, die teuer und umweltschädlich sind. Im Gegensatz dazu zeigen wir in dieser Arbeit, wie kontrollierte Faltenbildung einer dünnen, starren Schicht auf einem weichen, elastischen Substrat verwendet werden kann um nanostrukturierte Template herzustellen. Hierbei wird keinerlei Lithographie benötigt. Als Substrat wurde zunächst ein Silikonelastomer, Poly (dimethylsiloxan) (PDMS) verwendet. Durch Strecken eines PDMS-Substrats wurde eine vergrößerte Oberfläche erzeugt und anschließend mit Sauerstoffplasma zu einer glasartigen Schicht an der Oberfläche oxidiert. Entspannung des Substrats auf seine Originallänge führte zur Entstehung von periodischen Falten in der harten Schicht, die sich senkrecht zur angelegten Kraft orientierten. Unter definierten Bedingungen zeigten solche Falten eine sinusförmige Topologie mit einheitlicher Wellenlänge und Amplitude. Durch die Plasmabehandlungszeit kann der Faltenbildungsprozess kontrolliert werden und bietet die Möglichkeit, periodisch strukturierte Oberflächen im Bereich zwischen einigen hundert Nanometern und mehreren Mikrometern herzustellen.

Im Rahmen dieser Arbeit wurden Falten hergestellt, die als Template für die Anordnung von Nanopartikeln dienten. Faltige Substrate in Kontakt mit einer planaren Oberfläche bildeten parallele Kanäle. In diesen Kanälen wurde eine Suspension von Nanopartikeln (Polystyrol, r =55nm) eingetrocknet. Unter Verwendung von gleicher Wellenlänge und Amplitude der Falten aber unterschiedlicher Partikelkonzentration erhielten wir unterschiedliche Strukturen dicht gepackter, paralleler Linien von Nanopartikel. Für sphärische Partikel fanden wir Strukturen von einzelnen parallelen Linien bei geringer Partikelkonzentration bis hin zu pyramida-

len Strukturen bei hoher Partikelkonzentration. Die Wellenlänge der verwendeten Faltenstruktur fand sich im Abstand der Partikellinien wieder.

Um den Anordnungsmechanismus zu untersuchen führten wir Monte Carlo (MC) Computersimulationen durch, in Kooperation mit dem Lehrstuhl für theoretische Physik II (*Prof. Dr. Matthias Schmidt* und *Dr. Andrea Fortini*) an der Universität Bayreuth. Mittels MC können Anordnungen von Partikeln hinsichtlich ihres thermischen Gleichgewichts untersucht werden, wobei die freie Energie minimiert wird. Bei der Simulationen wird ein Modell starrer Kugeln in einer Box verwendet: Die Box ist von unten durch eine flache Wand und oben durch eine sinusförmige Wand begrenzt, analog zu unserem experimentellen Aufbau. Bei der Simulation wird nun diejenige Gleichgewichtsstruktur bestimmt, bei denen die Partikel minimale Energie besitzen. Die Ergebnisse der Gleichgewichtsstrukturen in Simulation und Experiment stimmten ausgezeichnet überein. Daraus lässt sich schließen, dass die Form der Kanäle maßgeblich für die Ausbildung der gefundenen Strukturen verantwortlich ist. Der Prozess ist damit unabhängig von der chemischen Beschaffenheit der Teilchen.

Tatsächlich erhielten wir gleiche Strukturen mit Gold-Nanopartikel (r = 33nm) unter Verwendung des bereits beschriebenen Anordnungsprinzips. In diesem Fall zeigte sich, dass bei Verwendung konstanter Partikelkonzentration aber unterschiedlicher Größe der Kanäle (unterschiedliche Wellenlänge und Amplitude der Falten) Einzellinien aus Gold-Nanopartikeln und Linien mit zwei Partikeln pro Reihe entstanden. Die unterschiedlichen Linien ergaben unterschiedliche optische Signale, da kollektive Schwingung der Leitungselektronen zu unterschiedlichen Wechselwirkung mit elektromagnetischer Strahlung in den verschiedenartigen Linien führen. Sind diese Teilchen genügend nahe zusammen, kann je nach Morphologie der Partikellinien ein anderes Signal erzeugt und mittels „Surface Enhanced Raman Spektroskopie“ (SERS) detektiert werden.
Das elektromagnetische Feld wurde mittels Dunkelfeldspektroskopie in Kooperation mit *Dr. Ramón Alvarez-Puebla* an der Universität Vigo in Spanien gemessen. Entlang der Partikellinien fanden wir eine statistische Verteilung der Feldstärke. An Stellen genau zwischen zwei Partikeln wurde ein sogenannter Hot Spot erzeugt, der durch Kopplung der Oberflächenplasmonen zweier Partikel entsteht und dadurch eine Verstärkung des elektromagnetischen Felds hervorruft. Bei den unterschiedlichen Partikellinien entstanden unterschiedliche Anordnungen der Hot Spots, welche als Verschiebung des Signals in der Dunklefeldspektroskopie gemessen wurde. Um das gemessene Signal zu bestätigen, führten wir in Kooperation mit *Weihai Ni* von er Universität Vigo in Spanien Simulationen mit der Finite-Difference Time-

Domain (FDTD) Methode durch. Die berechneten Spektren stimmten sehr gut mit den gemessenen Spektren überein was bedeutet, dass tatsächlich eine Oberflächenplasmonenkopplung zwischen einzelnen Nanopartikeln verantwortlich ist für die beobachteten SERS-Effekte. Mit Hilfe von Falten bei der Partikelanordnung können also Substrate erzeugt werden, bei denen ein quantitatives SERS-Signal gemessen werden kann. Solche Substrate könnten in Zukunft als biologische Detektoren, optische Filter oder Sensoren verwendet werden.

Weiterhin wird in dieser Arbeit gezeigt, wie die Struktur der Falten auf andere Materialien übertragen werden kann. PDMS neigt dazu, in organischen Lösungsmitteln aufzuquellen und verhält sich wenig formstabil. Bei der Herstellung von Falten mittels einer mechanischen Instabilität entstehen Strukturen, die zwar makroskopisch entspannt, jedoch nicht spannungsfrei sind auf der Mikroskala. Falten sind daher nicht langzeitstabil und die Höhe der Struktur geht nach einiger Zeit verloren. In dieser Arbeit stellen wir zwei Methoden vor, die es ermöglichen langzeitstabile und lösungsmittelbeständige Falten herzustellen.

Beim sogenannten mikro-Thermoformen wurde die faltige Oberfläche als eine Schablone verwendet. Thermoplastische Polymere (Polystyrol und Poly (methylmethcrylat)) wurden dazu über ihre Glastemperatur erwärmt und somit formbar gemacht. Mit Hilfe einer hydraulischen Presse wurde die Faltenstruktur in das weiche Polymer gedrückt. Das so strukturierte Polymer wurde abgekühlt und von der ursprünglichen Faltenstruktur getrennt. Die zweite Methode bestand aus einem Zwei-Schritt-Formverfahren, welchen in Zusammenarbeit mit *PD Dr. Kerstin Koch* und *Micheal Bennemann* am Nees-Institut in Bonn entwickelt wurde. Zunächst wurden Falten mit Wachs abgeformt und das strukturierte Wachs in einem zweiten Schritt mit Epoxidharz abgegossen. Mit beiden Methoden erhielten wir perfekte Kopien der gefalteten Struktur selbst bei Wellenlängen und Amplitude von nur wenigen hundert Nanometern. Die Abgeformten Falten besaßen keine inneren Spannungen mehr, da sie aus nur einer Komponente bestehen. Die hergestellten nanostrukturierten Polymere sind resistent gegenüber vielen Lösemitteln und formstabil, sie sollen als Substrate in der Mikrofluidik benutz werden.

Im letzten Teil dieser Arbeit, wurden Falten als Stempel im sogenannten Mikro-Kontaktdruck- Verfahren (μCP) verwendet. Bei dieser Technik wird ein topographisch strukturiertes Elastomer (Stempel) verwendet, um ein oberflächenaktives Molekül auf ein flaches Substrat zu übertragen. Dabei entstehen chemisch strukturierte Oberflächen mit unterschiedlicher Ladungsdichte, welche Anwendungen auf dem Gebiet der Biosensorik, diagnostischen Immunoassays und für Zellkulturen finden. Üblicherweise werden Stempel für μCP durch

ein zweistufiges Verfahren, bei welchem ein lithographisch hergestellter strukturierter Silizium-Master als Schablone dient, hergestellt. Ein Elastomer wird nun benutzt um die Struktur des Masters abzuformen. Dadurch erhält man einen meist mikroskopisch strukturierten Stempel. Wie bereits erwähnt ist die Herstellung von Strukturen mittels Lithographie äußerst kostenintensiv und beinhaltet umweltschädliche Ätzverfahren. Im Rahmen dieser Arbeit stellen wir die bereits beschriebene kontrollierte Faltenbildung als ein einstufiges Verfahren zur Herstellung von nanostrukturierten Stempeln vor. Die Vielfalt der Stempelstrukturen, die mittels Faltenbildung hergestellt werden können, ist begrenzt, jedoch besticht dieses Verfahren durch seine Einfachheit im Vergleich zu Lithographie-basierten Herstellungsverfahren. Der Prozess der Faltenbildung selbst involviert Plasmaoxidation, welche die Oberfläche hydrophilisiert. Daher konnten geladene Polyelektrolyte an der Oberfläche adsorbiert werden. Diese strukturierte Oberfläche wurde nun mit einer entgegengesetzt geladenen Oberfläche kontaktiert und Material selektiv an den Kontaktstellen vom Stempel übertragen. Mittels Rasterkraftmikroskopie (AFM) konnte eine Struktur von abwechselnd Erhöhungen (bedruckte Bereiche) und Vertiefungen (nicht bedruckte Bereiche) gemessen werden.

Ziel dieser Studie war es, die Grenze eines solchen μCP-Prozesses zu bestimmen, also die kleinste Faltenstruktur, ab der kein erfolgreicher Druckprozess mehr stattfindet. Amplitude und Wellenlänge des Stempels wurden systematisch variiert. Das untere Limit für die Wellenlänge der Falten konnte zu 355nm und die Amplituden zu 40nm bestimmt werden, bei denen die gedruckte Struktur nicht mehr zu erkennen war (da Material sowohl von den Erhöhungen der Falten als auch aus den Bereichen der Täler übertragen wurde). Die Höhe der übertragenen Struktur stieg mit zunehmender Wellenlänge und Amplitude der Falten, tendierte aber zu einem Plateauwert von 6-7nm auch bei weiterer Vergrößerung der Topologie der Falten. Die kleinsten lateralen Strukturen (50nm) jedoch konnten in den Bereichen erzeugt werden, in denen kein Material übertragen wurde.

Chapter 3 Introduction

Within this introduction, an overview on research and development of surfaces patterning and wrinkling as a structuring principle will be presented. Techniques including assisted self-assembly of particles as well as characterization methodologies of such assemblies are addressed.

3.1 Patterning and Wrinkling-from the tallest Mountains to Nanostructures

Many of the extraordinary structure-related properties found in biological systems are caused by periodic structures on the micron and sub-micron scale. Examples are special hydrodynamic or aerodynamic properties, like reduction of turbulent drag/hydrodynamic friction as found for sharkskin (Figure 3-1) or dragonfly wings.

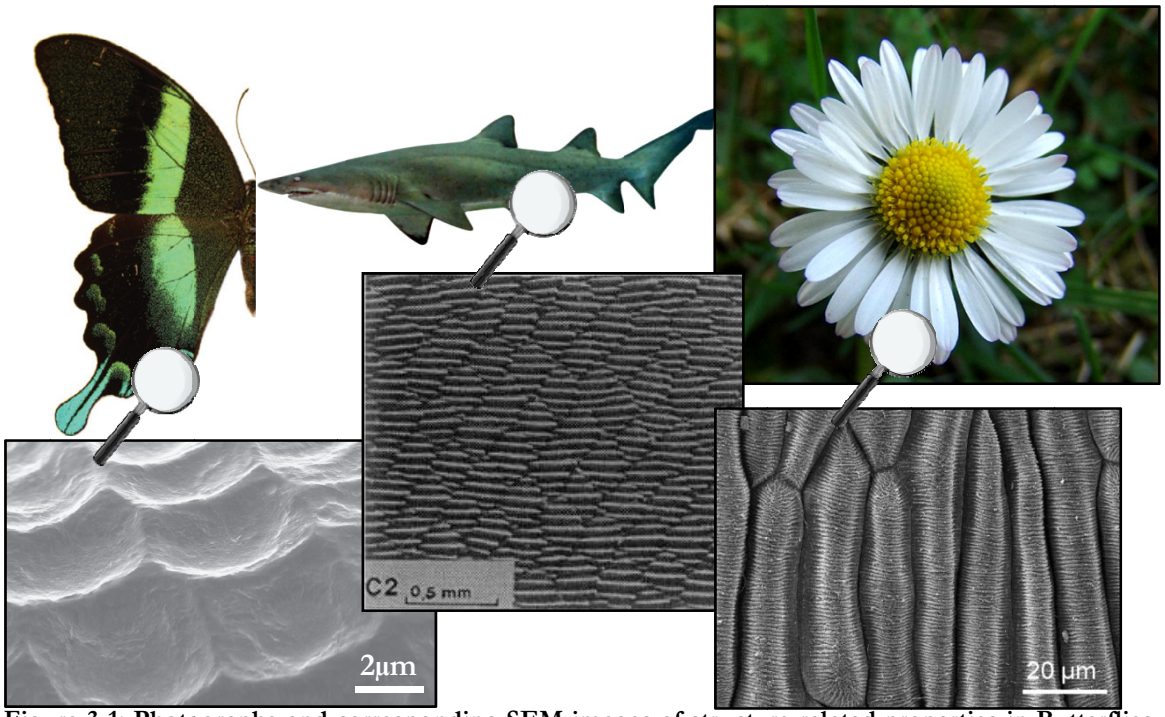

Figure 3-1: Photographs and corresponding SEM images of structure-related properties in Butterflies, Sharks and Daisies. (Left) Beautiful colors in butterfly wings of *P.Blumei* caused by a periodic nanostructure. SEM imaging shows that the surface of a wing scale is covered with concavities (diameter≈ 5–10µm) that are arranged in ordered lines along the scale. These concavities are clad with a multilayer that reflects yellow-green light at their centers and blue at their edge. Reprinted with permission from[1]. Copyright (2010) by the Nature Publishing Group. (Middle) Dusk Shark skin (*Carcharhinus Obscures*) shows periodic ridges that decrease hydrodynamic friction.[2] Copyright (1985) by Elsevier. (Right) Cuticular folds of a petal (flower leaf) of Daisies (*Bellis perennis*) with elongated cells and parallel orientated cuticular folds causing superhydrophobicity. Reprinted with permission from[3]. Copyright (2010) by Wiley-VCH.

Discovering and mimicking such structure-property relations in science and technology opened a broad field known as *biomimetics*.[4] Periodic structures on the micro-and nanoscale develop the brightest and most vivid colors in nature which arises from the interaction of light with such surfaces. In the wings of butterflies, combinations of optical structures give rise to complex color mixing (Figure 3-1).[1] As a last example, hierarchical nanofolds on petals' surfaces of roses or daisies (Figure 3-1) provide a sufficient roughness for superhydrophobicity and yet at the same time a high adhesive force with water. A droplet of water will not roll off such a surface even if the petal is turned upside down. This so called "petal effect"[5] is along with the self-cleaning "lotus-effect"[6] one of the most effective and biologically useful structure-related property developed by nature.

Given this amount and diversity of benefits offered by periodically structured matter, it is not surprising, that a huge variety of technological approaches for the fabrication of such structures has been developed in the past. For a recent review on various patterning approaches we refer to the literature.[7] Different Methods to fabricate periodically structured substrates have appeared and almost all of them are based on the three-step process of conventional lithography, thin film deposition and etching.[8-10]

An alternative approach for topographical structure formation is *wrinkling* which can be found in biological matter as a widely occurring assembly principle. A bucking instability is responsible for the development of wrinkles. However wrinkling is not limited to biological matter: One of the most prominent examples of a monument in nature caused by wrinkling are the Alps, a so-called alpine folded mountain. 80 million years ago, continental drift caused enormous thrust onto Earth's surface and the Alps as we know them nowadays arose (Figure 3-2).

The fundamental mechanism observed, is that the stratum eludes the occurring lateral strain by forming a heightened surface upon folding. Structure formation via folding or wrinkling in nature is rather generic and covers all imaginable length scales. Wrinkling of skin for example occurs during ageing: The human epidermis wrinkles if the soft dermis underneath shrinks and generates a compression force. As human fingerprints are formed according to suchlike principle, *minutiae* are formed as random patterns designed by predisposition and environment. These so called epidermal ridges are unique and allow for authentication of people.

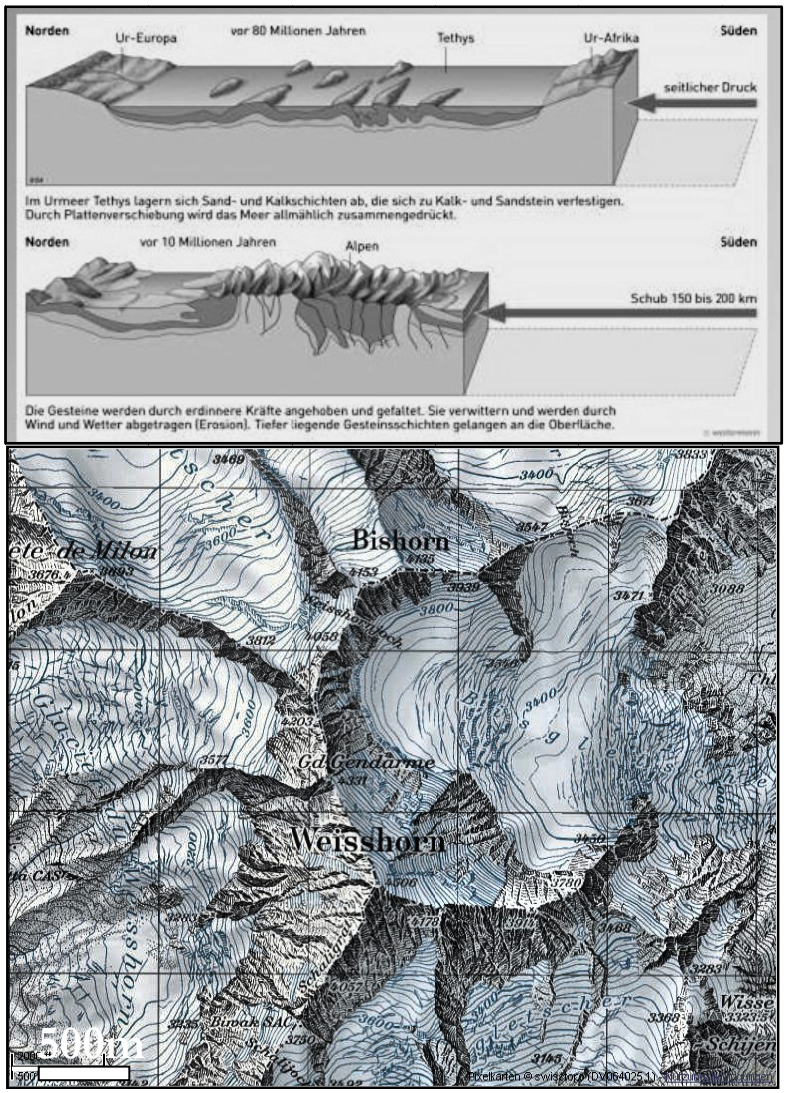

Figure 3-2: (Top) Formation of the Alps 80 Million years ago due to lateral strain caused by continental drift. Reprinted with permission from[11]. © 2011 by Bildungshaus Schulbuchverlage, Westermann, Braunschweig. (Bottom) Typical topographical alpine landscape in the Swiss Alps showing valleys and summits. Blue lines represent contour lines. Reprinted with permissionfrom[12]. © 2011 swisstopo.

Learning from nature, an alternative approach to structure surfaces based on wrinkling has been successfully explored in technology along the last 30 years. Remarkably, no lithography has to be used in this structuring process as the underlying mechanism is based on a buckling instability. By manipulating a silicon elastomer such that a thin hard layer covering the elastomer is exposed to strain, wrinkles can be induced. A detailed physical description will be provided in Chapter 3.2. Silicone rubber can be made by cross linking linear polymeric chains of PDMS (poly (dimethylsiloxane)) (a silicone fluid) under the influence of certain free radical catalysts. Silicone elastomers are particularly convenient substrates for structural manipulation because they are readily cross linked to different Young's moduli. In addition they are highly flexibel. PDMS is durable with a low toxicity and has a broad commercial availability.

Already in 1982, Martin and coworkers observed ordered wrinkles on thermally expanded PDMS upon aluminum evaporation (Figure 3-3a).[13] 16 years later, Bowden and coworkers picked up the idea and coated a thermally expanded PDMS substrate with a thin gold layer, leading to a disordered wavy structure after cooling of the specimen (Figure 3-3b).[14] Shortly after that they recognized the potential of this method to align the wrinkles by generating an anisotropic pre-strain that defines one preferred direction in which the wrinkles line up (Figure 3-3c).[15]

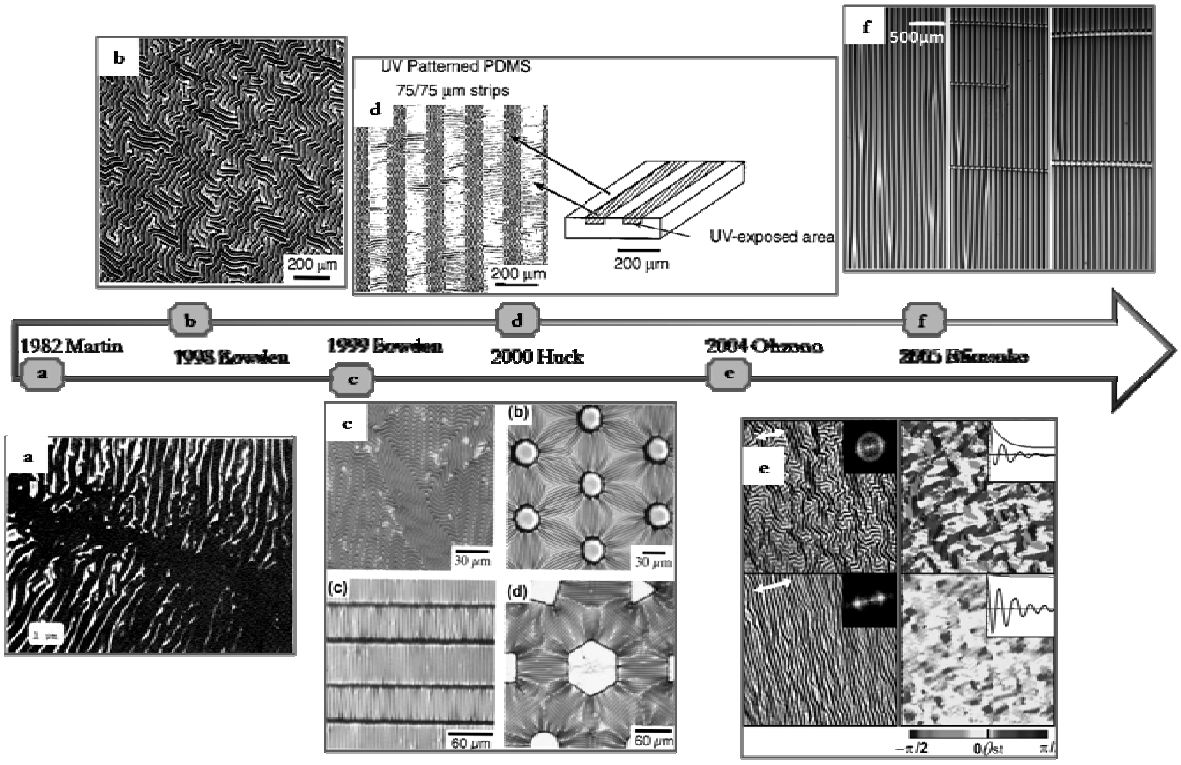

Figure 3-3: History and development of controlled wrinkling during the last decades. (a) Wrinkling of a thin metal film on PDMS discovered by Martin. Reprinted with permission from[13]. Copyright (1982) by AIP. (b,c) Bowden applied a pre-strain on the system to cause local ordering of the wrinkles and applied plasma onto PDMS to render the topmost surface hard. Reprinted with permission from[14,15]. Copyright (1998) and (1999) by the Nature Publishing Group and AIP. (d) Huck refined the idea by partially masking a surface of PDMS during UV-light exposure leading to areas of different coefficient of thermal expansion. Reprinted with permission from[16]. Copyright (2000) by ACS. (e) Ohzono applied a small uniaxial stress and showed that wrinkles aligned perpendicular to the direction of the stress. Reprinted with permission from[17]. Copyright (2004) by APS. (f) Efimenko finally described controlled wrinkling by clamping and stretching a PDMS which was subsequently exposed to UV/ozone. Reproduced with permission from[18]. Copyright (2005) by the Nature Publishing Group. By adjusting the strain and the UV/ozone exposure time, the wrinkling topology could be controlled with high precision.

The directionality was first applied by steps and edges inside the supporting material (PDMS) leading to locally ordered strain upon thermal expansion. In the expanded state, the topmost layer of PDMS was toughened during plasma oxidation by cross linking. The idea was refined by partially masking a surface of an elastomeric material during UV-light exposure lead-

They applied a small uniaxial stress and showed that wrinkles aligned perpendicular to the direction of the stress (Figure 3-3e).

After this experiments published in 2004 it was obvious that the key mechanism in this method is the generation of anisotropy in the pre-buckling or post-buckling stress state, allowing one preferred direction in which the wrinkles line up. This directionality can be induced by clamping and stretching a substrate along one direction (Figure 3-3f); *controlled wrinkling* was invented.[18] The triumphant success of this structuring method is owed to its stunningly easy concept: A slab of PDMS is fixed between two clamps and stretched to 120-150% of its original length. The enlarged surface is oxidized by UV/ozone which was previously identified to convert the topmost surface of PDMS into a stiff film of silica (Figure 3-4).[19,20] During this process, defects like junctions (because they are energetically favored) and cracks may occur due to the brittle nature of the stiff silica layer (Figure 3-3f).

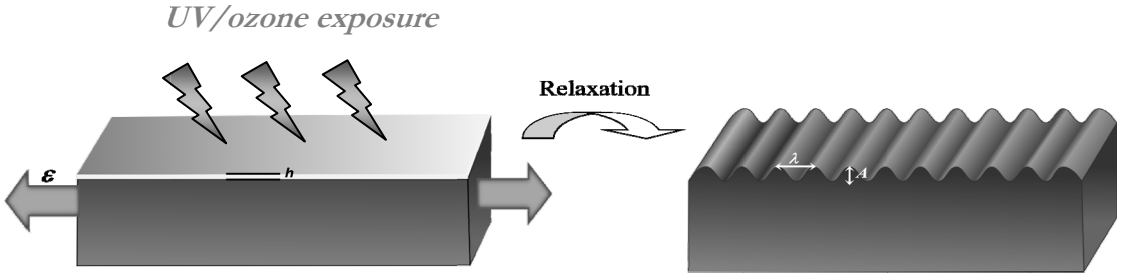

Figure 3-4: Principle of controlled wrinkling according to Efimenko.[18] A thin slab of PDMS is expanded by a certain value ε and exposed to UV/ozone or oxygen plasma. After the topmost layer is rendered a thin hard film (height h) of silica, the system is relaxed and wrinkles with a defined wavelength λ and height A occur.

The surface shape of the pattern was found to depend on the balance between the *bending energy* of the stiff top-layer and the *deformation energy* of the substrate.[21] The theory of wrinkling formation will be described more detailed in Chapter 3.2. Here it shall be highlighted how these two parameters can be addressed as sources of diversity for pattern formation based on wrinkling. The bending energy of the stiff top-layer mainly depends on its material properties. Different materials were considered as already mentioned, for example metals, polymers and inorganic materials like silica. In addition, the strain field was varied to obtain more complex patterns (Figure 3-5). Single-axial strain fields yield line topologies (Figure 3-5a); biaxial strain fields render chevrons topologies (Figure 3-5b).[22,23] Localized strains will result in spoke-like patterns or target-like radial patterns (Figure 3-5c).[24-26] Even more complex patterns with different levels of hierarchy, such as checkerboards, may be as well prepared from pre-patterned surfaces exposed to a second strain field.[27]

terns with different levels of hierarchy, such as checkerboards, may be as well prepared from pre-patterned surfaces exposed to a second strain field.[27]

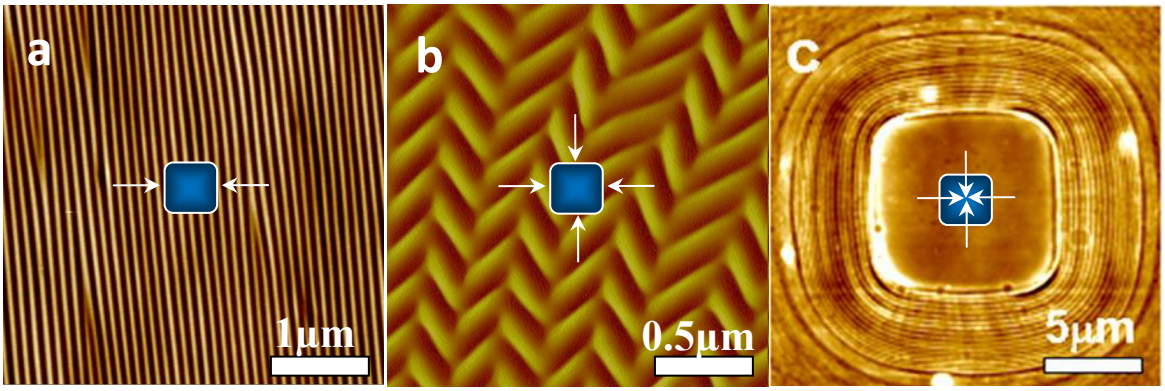

Figure 3-5: Different resulting patterns created by controlled wrinkling. The variable in (a), (b) and (c) is the strain field applied onto the system of stiff layer on soft elastomer. (a) Striped patterns can be found if a linear, uniaxial strain is present. (b) Chevron topology is the result of a biaxial strain and (c), radial pattern evolve if a local strain pointing towards the indicated middle is applied. Reprinted with permission from[26]. Copyright (2008) by ACS.

3.2 Theory and Physics of Wrinkling

Any free-standing plate or rod, subjected to compressive stress, will spontaneously buckle if a certain critical stress *T* is exceeded (Figure 3-6a). The plate (or rod) expands by bending out of the normal film plane. Two competing mechanisms will determine the wavelength of the buckle: the relaxation of the in-plane strain and the elastic stresses associated with bending. In this simple case, the buckling wavelength will scale with the length of the rod. If other external forces are present, the wavelength is influenced. These external forces can be caused by a surrounding elastic medium. In this case, the wavelength is a result of balancing the *bending energy* of the plate and the *deformation energy* of the surrounding medium.[21] One nice example of this is shown in Figure 3-6c, where rails buckle due to thermal expansion. The rails ought to become elongated but they are compressed back as the support of rails inhibits expansion. This compressive strain causes the rail to buckle and can be serious enough to cause derailment.

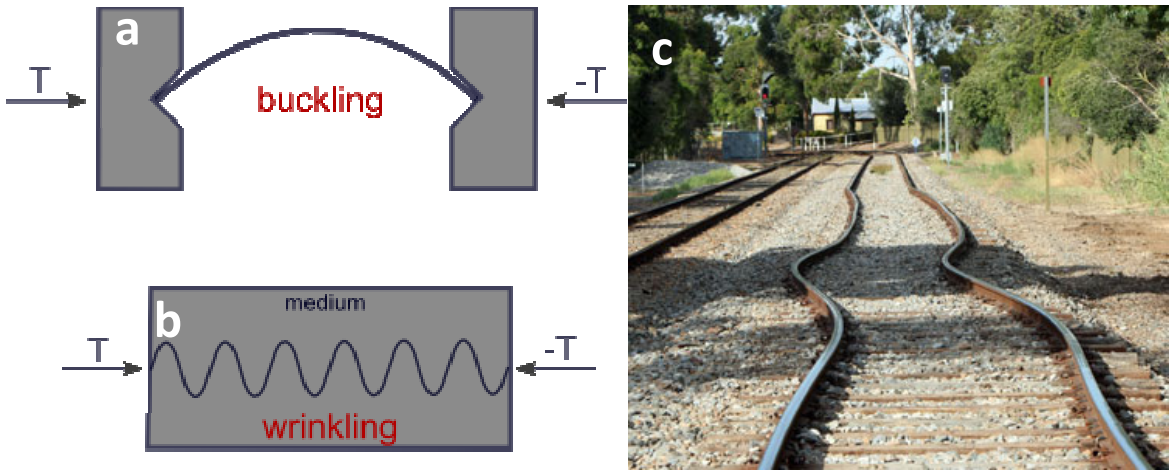

Figure 3-6: (a) Euler instability: above a critical pressure force T buckling of a rod is observed. (b) Wrinkling of a plate surrounded by an elastic medium. (c) Failure of rails due to the buckling instability caused by thermal expansion of rails.[28]

In elasticity, buckling of a stiff supported layer under compression is a well studied phenomenon which dates back to Euler and Biot.[29] For wrinkling -which is referred to if smaller wavelengths emerge- a lot of theoretical work has been done to describe and predict the geometry of wrinkles.[14,30,16,31,32] An additional surrounding medium provides forces which suppress long wavelength buckling (Figure 3-6b).[33,34] If a strain is applied, the elastic energy has to be minimized by the fundamental wrinkling mode. Wrinkling of the film requires continuous deformation of the substrate while delaminating of the film is avoided. A stationary solution of a plate surrounded by an elastic medium, as in Figure 3.6b, can be described by

$$EX''''+TX''+\alpha X+\beta X^3=0\ , \tag{3.1}$$

where T is the compression force, X the deformation of the plate, E is the Young's modulus of the plate, α is linear spring constant of the elastic medium and β the non-linear elasticity coefficient.[35] If we assume a linear problem ($\beta = 0$) we see that the spring constant depends linearly on the wave vector k; $\alpha = a(k) = a_0 k$, and (3.1) becomes

$$EX''''+TX''+\alpha_0 kX+\beta X^3=0. \tag{3.2}$$

We assume the following boundary conditions: $X(0) = X(L) = 0$ and $X''(0) = X''(L) = 0$ (with L being the length of the plate). The ends of the plate rest and no torque has to be considered. We take the following ansatz:

$$X = A\sin(kz) \quad \text{with} \quad k=\frac{n}{L}\pi. \tag{3.3}$$

First the critical values are estimated. Therefore β is neglected. From (3.1) with (3.3) we obtain

$$Ek^4 - Tk^2 + \alpha_0 k = 0 \qquad T(k) = \frac{Ek^3 + \alpha_0}{k}\,. \tag{3.4}$$

To find a minimum, we differentiate with respect to the wave number

$$\frac{dT}{dk} = 0 \rightarrow k_c = (\alpha_0 / 2E)^{1/3} \qquad T_c = T(k_c) = \frac{3}{2}(2E\alpha_0{}^2)^{1/3}\,. \tag{3.5}$$

The critical wave number is dependent on the elastic properties of the medium (α) and of the plate (E) and independent of L. The amplitude A can also be calculated as a function of the critical wave number, in which case we can write

$$X^3 = A^3 \sin^3(kz) = \frac{A^3}{4}\left[3\sin(kz) - \sin(3kz)\right]. \tag{3.6}$$

If we consider the ground mode $\sin(kz)$ and neglect the higher mode $\sin(3kz)$ we obtain from (3.1)

$$\left[Ek^4 - Tk^2 + (\alpha_0 k + \frac{3}{4}\beta A^2)\right]A = 0\,. \tag{3.7}$$

One solution would be $A = 0$ (no wrinkles); the second solution is

$$A^2(k) = \frac{4}{3\beta}(Tk^2 - Ek^4 - \alpha_0 k)\,. \tag{3.8}$$

Implementing the relative distance to the critical value

$$\eta = \frac{T - T_c}{T_c} \;\rightarrow\; T = T_c(1+\eta)\,, \tag{3.9}$$

leads, after replacement in (3.8) at the critical wave number, to

$$A_c^{\,2}(k_c) = \frac{4}{3\beta} T_c k_c^{\,2} \eta\,, \tag{3.10}$$

which shows that the amplitude increases with $\eta^{1/2}$. To examine the stability of wrinkles we use the potential which can be derived from (3.1)

$$V = \frac{1}{L}\int_0^L dz\left[\frac{1}{2}EX''^2 - \frac{1}{2}TX'^2 + \frac{1}{2}\alpha X^2 + \frac{1}{4}\beta X^4\right]. \tag{3.11}$$

We use the ansatz (3.3) and (3.8) to solve the potential

$$\begin{aligned} V &= \frac{1}{4}A^2\left[Ek^4 - Tk^2 + \alpha_0 k + \frac{3}{8}\beta A^2\right] \\ &= -\frac{3}{32}\beta A^4(k) \\ &= -\frac{1}{6\beta}(Tk^2 - Ek^4 - \alpha_0 k)^2\,. \end{aligned} \tag{3.12}$$

If T is replaced by (3.4) we see that V has a change in sign at $T = T_c$ and V turns negative for $T > T_c$. This shows clearly that the periodic structure of the plate has a smaller potential energy compared to a flat plate. If we examine a plate with given Young's modulus, transversal contraction (Poisson's ratio) ν, and thickness h, we obtain according to Tarasovs[36] and Biot[29] from (3.1)

$$\frac{E_f I}{1-\nu_f^{\,2}}\frac{\partial^4 X}{\partial z^4} + T\frac{\partial^2 X}{\partial z^2} + \alpha X = 0. \tag{3.13}$$

E_f is the Young's modulus of the film, ν_f the Poisson's ratio of the film and $I=d^3/12$ the moment of inertia per length, h is the film thickness. X is the deflection, T the longitudinal force and α is the spring constant of the elastic medium. Following,[29] the spring constant can be written as

$$\alpha = \frac{E_s \pi}{(1-\nu_s^{\,2})\lambda}\ . \tag{3.14}$$

E_s and ν_s are Young's modulus and Poisson's ratio of the substrate, respectively, and λ describes the resulting wavelength. To solve (3.13) we use (3.3) and $k=2\pi/\lambda$:

$$T = \frac{E_f h^3}{12(1-\nu_f{}^2)}\left(\frac{2\pi}{\lambda}\right)^2 + \frac{E_s \lambda}{4\pi(1-\nu_s{}^2)}. \tag{3.15}$$

To obtain the critical wavelength we proceed according to (3.5)

$$\lambda_c = 2\pi h \sqrt[3]{\frac{E_f(1-\nu_s{}^2)}{3E_s(1-\nu_f{}^2)}}. \tag{3.16}$$

The critical amplitude is[30]

$$A_c = h\sqrt{\frac{\varepsilon}{\varepsilon_c}-1}. \tag{3.17}$$

These equations suggest a linear dependence of the wavelength as well as the amplitude with respect to the film thickness h. This was experimentally approved by several groups as well as the dependence of the amplitude on the applied strain ε. Efimenko and others also proved that the wavelength can be reduced by increasing the strain.[27,18] The aspect ratio A/λ scales as

$$\frac{A}{\lambda} = \frac{1}{\pi}\sqrt{\Delta\varepsilon}, \tag{3.18}$$

where $\measuredangle\varepsilon$ is ε-ε_0.

The critical stress ε_c required to observe wrinkling after (3.16) and (3.17)[34,30]

$$\varepsilon_c = \sqrt[3]{\frac{3E_s(1-\nu_f{}^2)}{8E_f(1-\nu_s{}^2)}}. \tag{3.19}$$

If we want to consider wavelength and amplitude beyond the critical values we have to consider the non-linear term β again. According to Jiang and coworkers additionally a non-linear strain-displacement relation and a modified strain-displacement configuration between the film and the substrate has to be taken into account.[31] Importantly, the initial strain free (or

stress free) state for the film and the substrate are different as the film is free of forces when mounted onto the strained substrate, while the substrate is free of strain after releasing the stress. However, the interface between substrate and film is not affected by this. Thus, wavelength λ and amplitude A of a wrinkled patter can be described as

$$\lambda = \frac{\lambda_c}{(1+\varepsilon)(1+5\varepsilon(1+\varepsilon)/32)^{1/3}} \tag{3.20}$$

and

$$A = \frac{A_c}{\sqrt{1+\varepsilon}(1+5\varepsilon(1+\varepsilon)/32)^{1/3}}. \tag{3.21}$$

For small values of the strain, λ approximate (3.16).

As mentioned, the substrate is free of strain if the macroscopic stress acting on the system is released and the film wrinkles in a sinusoidal manner to minimize its bending energy. This implies that the film is *not* completely free of stress and might be subject to subsequent relaxation.

3.3 Diversity and Applications of Wrinkles-State of the Art

What really makes wrinkles a great tool in nanotechnology is its simple and inexpensive fabrication. Numerous publications take advantage of the highly uniform periodicity of the wrinkles such as stress-sensitive diffraction grating.[15,37] Another method named SIEBIMM (strain induced elastic buckling instability for mechanical measurements) uses the occurrence of a single dominant wavelength to solve equation (3.16) for the elastic modulus E_f. Any thin film that can be elastically deformed e.g. Polystyrene (PS)[38] and polyelectrolyte multilayer[39,40] as well as hybrid materials containing nanoparticles and biomacromolecules[41-43] can be used. If the thin film can be gradual in thickness, the wrinkling wavelength shifts linearly with the film dimensions. Different wavelength yield different iridescent colors when illuminated with white (Figure 3-7).

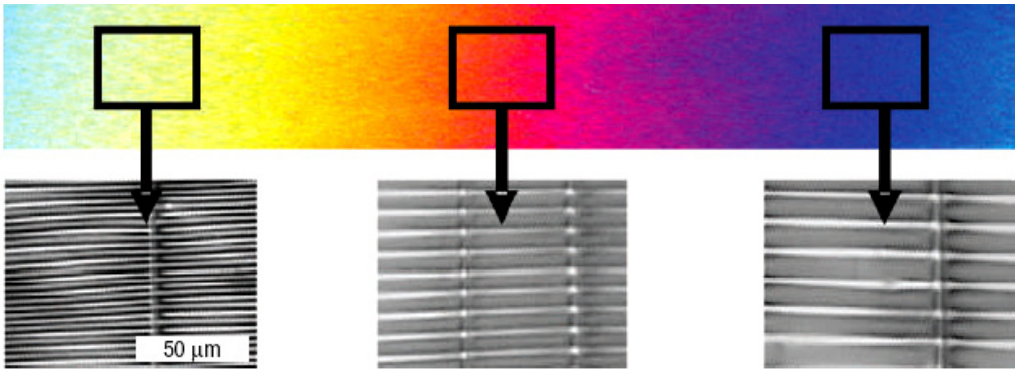

Figure 3-7: Modulus measurements of a thickness gradient film of PS. (a) Optical micrograph of a PS-thickness gradient on silicon wafer (140nm to 280nm). Grayscale insets show optical micrographs of the film after transfer to PDMS and application of strain to induce buckling. The doubling of the film thickness from left to right results in a doubling of the buckling period. Reprinted with permission from[38]. Copyright (2004) by the Nature Publishing Group.

As highlighted in Chapter 3.2, the geometry of surface wrinkles is readily adjustable in terms of wavelength and amplitude by controlling the thickness of the stiff film and the strain, respectively. Wrinkles are reported to have tunable wetting and adhesion properties[44-47] which can be anisotropic because of the anisotropic nature of the troughs. These interesting properties have been successfully tested in coatings for marine antifouling.[48]

3.4 Wrinkle-Assisted Self-Assembly of Nanoparticles

For a complete introduction to the subject of template-assisted self-assembly we refer the reader to our recently published article "Controlled wrinkling as a novel method for the fabrication of patterned surfaces"[49] and to the references therein.[50,51] In this section, without any pretence to completeness, we give a short overview over controlled placement of nanoscale building blocks.

Ordered arrays made from colloidal particles have various applications such as optical band gap materials and they can trigger epitactic growth of three-dimensional crystals.[52-57] If the assembled colloidal particles are of nanoscale dimensions, they can serve as electronic functional units or sensors or for data storage.

Not only the order within different assemblies but also the interaction *between* two or more particles opens various applications in the fields of sensors if a corresponding optical or electronic signal can be detected. Optical properties of metal nanoparticles are governed by col-

lective oscillation of conduction electrons causing localized surface Plasmon resonance (LSPR), the frequency at which conduction electrons oscillate in response to the alternating electric field of incident electromagnetic radiation.[58] So- called hot spots, where the interaction of the electromagnetic field of two or more particles on a surface is extremely high, can be used to enhance the efficiency of analytical techniques. Among others, surface enhanced Raman spectroscopy (SERS) is preferably used to characterize the response of metal nanoparticles (mainly gold, silver and copper because of the presence of free conduction electrons) located at surfaces when irradiated with light. As the enhancement factor is independent from the particle density on the substrate even single particles or molecules can be detected. To create films of nanoparticles, where hot spots are randomly distributed, physical vapor deposition is mainly used to create gold or silver island films.[59] Still, controlling the exact geometry or number of hot spots within an illuminated area would be required to perform quantitative SERS analysis on a plasmonic substrate.

Basic strategies for templating colloidal assemblies can be divided into deposition techniques where particles are spontaneously self- assembled into organized superstructures or obligated to adopt the desired conformation by using confining geometries. In all cases, either *chemical*[60,61] or *physical*[62,63] contrast of surfaces are used to guide the controlled arrangement of particles into one or more-dimensional supercrystals.

The term "template-assisted self-assembly" (TASA) is used if a physical constraint is applied to guide the self assembly of nanoparticles. TASA minimizes the total number of defects in the final assembly. Exact location of particles can be provided as well as size and shape of the arrangement. TASA is the technique of choice once nanoscale building blocks have to be linked to defect free mesoscopic structures. For example this is required to build up efficient optical or electronic devices, where size and shape control are indispensable. The colloidal crystallization into periodic lattices (supercrystals) gives rise to unique and fascinating optical properties with potential applications as detectors, circuits, light sources, polymeric opals and meta materials. Structures with periodicities comparable to the wavelength of visible light are interesting as these enable one to make use of their optical band structure. In particular, linear assemblies, such as particle wires possess high potential for photonic applications.[64,65]

As described in Chapter 3.1, topographic templates can be fabricated using photolithographic[50,51] and soft lithographic[66-68] techniques or, in contrast, by controlled wrinkling revealing a sinusoidal topology with a defined as well as tunable wavelength and amplitude. The emergence of a sinusoidal topology involves not only the appearance of periodic waves but also

the formation of countless interjacent channels. Efimenko and coworkers were the first to use these channels as microfluidic sorters for spherical particles.[18] Liquids can be shaped into regular arrays of liquid filaments as shown by Ohzono. They decreased the thickness of a liquid film to the height of the wrinkles height.[69] Lu and coworkers exploited a method to arrange colloidal particles into wrinkles' grooves out of suspensions by means of dip-coating.[70] To avoid random particle attachment, repulsive interactions between particles and substrate had to be chosen as well as matching dimensions of particles and topology of the wrinkles. If this is the case, particles are driven to assemble in the wrinkles' grooves by capillary forces upon drying. Dense lines of particles are formed. These lines represent one- and two-dimensional colloidal crystals with tunable spacing between the lines according to the periodicity of the wrinkled template (Figure 3-8).

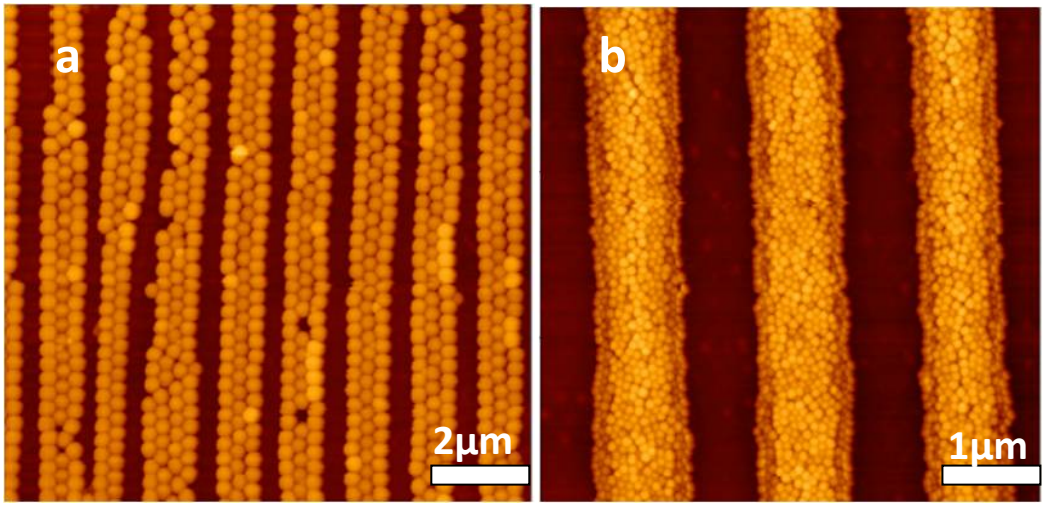

Figure 3-8: AFM images of selective deposition of (a) 380nm and (b) 80nm-sized colloidal particles on wrinkled films made from polyelectrolyte multilayer.

Nevertheless, dip-coating is a rather slow assembly method done at retraction speeds as slow as 10µms^{-1}. Horn and coworkers showed however, how a faster spin coating experiment can trap rod-like bionanoparticles (Tobacco Mosaic Virus (TMV)) into grooves of wrinkled substrates.[71] The use of radial forces to guide the assembly process reduces the parameters for successful selective coverage of the wrinkled surface. Such assemblies trapped in wrinkles troughs can be transferred onto hydrophilic flat surfaces by using the reversible nature of the wrinkles. Hyun and coworkers stretched a particle decorated wrinkled surface to smoothen the wrinkles and contacted it to a glass substrate. The particles migrate to the glass surface and the process could be repeated.[72] In contrast, Horn and coworkers showed how flattening upon stretching of the originally wrinkled surface is not necessary to transfer bionanopar-

ticles out of the troughs if liquid is still apparent around the particles directly after spin coating. They described a low pressure technique where the particles-filled wrinkles were just pressed against a hydrophilic substrate.[73] Capillary forces accomplishes the migration and striped geometries with different spacing of the stripes of TMV can be designed (Figure 3-9).

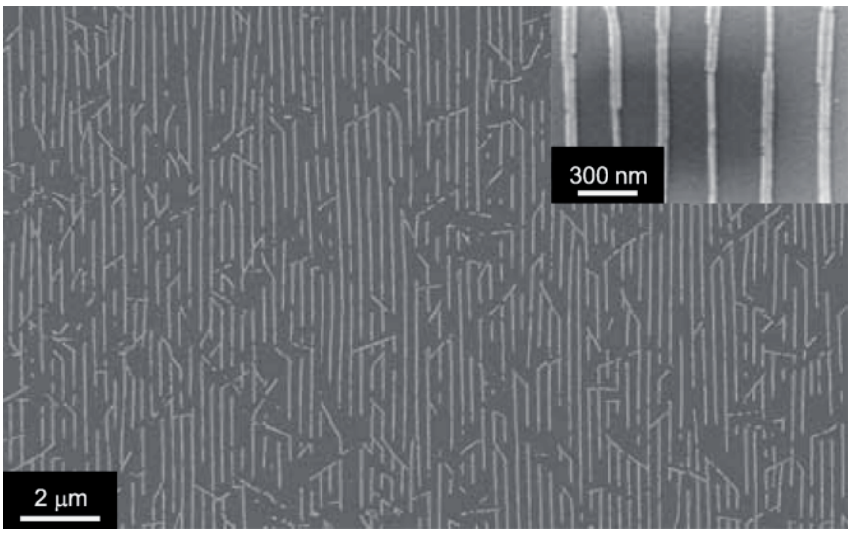

Figure 3-9: SEM image of TMV printed on silicon wafer. The distance between the single stripes is approximately 290nm. Reprinted with permission from[73]. Copyright (2010) by Wiley-VCH.

3.5 Understanding Assembly Mechanisms of Nanoparticles by Monte Carlo computer simulation

Monte Carlo (MC) computer simulation has been proven to describe soft condensed matter systems with high precision. Especially colloidal suspensions can be characterized in terms of their equilibrium configuration that minimizes the free energy. MC uses the tools of statistical physics where colloidal particles play the role of atoms or molecules to describe their capability to self-assemble into a particular configuration. A complete introduction of molecular simulations can be found in the literature.[74-77] Here, only a small overview will be given. The Metropolis Monte Carlo method is performed within the canonic ensemble (constant number of particles N in a constant volume V at a fixed temperature T) and the thermodynamics can be extracted from the Helmholtz free energy

$$F = -k_B T \log Q, \tag{3.22}$$

with the partition function

$$Q = \frac{1}{h^{3N} N!} \int d\vec{p}^{\,N} d\vec{r}^{\,N} \exp\left[- H(\vec{r}^{\,N}, \vec{p}^{\,N}) / k_B T \right], \tag{3.23}$$

where h is the Plack constant, k_B the Boltzmann constant, $\vec{r}$ the position of the particles, $\vec{p}$ describes the moments and $H(\vec{r}^{\,N}, \vec{p}^{\,N})$ is the Hamiltonian of the system. Unfortunately, direct computation of the free energy is prohibited because the number of configurations in the integral is almost unlimited. Metropolis and coworkers proposed an indirect method to compute the thermal average of an observable A ($\langle A \rangle$).[78] The idea behind the so called Metropolis Monte Carlo algorithm is to generate configurations randomly that obey the Boltzmann distribution. The observable A is sampled for a number of these configurations. N particles in a Volume V are simulated in the canonic ensemble. One particle i is selected and its position r_i is changed by a random distance Δr_i. If the trial move is accepted or not is determined by the difference in energy $\Delta U = U(r_i + \Delta r) - U(r_i)$ between the new and the former configuration. The particle is moved to the new position, if $\Delta U < 0$ or with a probability $\exp(-\Delta U / k_B T)$ if $\Delta U > 0$. The particle i stays in the former position r_i if the move is rejected. The cycle is repeated and the value A_k of the observable A is calculated for the instantaneous configuration k. The average over M independent and uncorrelated configurations has to be equal to the result of the average $\langle A \rangle$:

$$\langle A \rangle = \sum_{k=1}^{M} \frac{A_k}{M}. \tag{3.24}$$

With this algorithm, the average value of an equilibrium observable can be determined and compared to experiments. MC simulations are not limited to the canonic ensemble; other quantities can be kept constant like pressure or chemical potential.

For colloidal particles, a hard sphere model is proposed where perfect hard spheres are not allowed to interact with each other except when two spheres overlap. In this case, the interaction is infinity. The inter-sphere potential is

$$\upsilon_{ij}(R_{ij}) = \begin{cases} \infty & \text{if } R_{ij} < 0 \\ 0 & \text{otherwise,} \end{cases}$$

where R_{ij} is the distance between two colloidal particles and σ the diameter of the sphere. The volume fraction (also called packing fraction) is variable. For a system with volume V and number of particles N the volume fraction is defined as $\eta = \pi/6\sigma^3 N/V$. A phase diagram has been established where the fluid phase is stable for $\eta < 0.4915$. Crystal and fluid phase coexist at $0.4915 < \eta < 0.5428$ and for $\eta > 0.5428$ a face centered cubic (f.c.c.) phase is stable.[79,80] The crystal phase is stabilized by entropy only if the interaction energy of hard spheres is always zero. Interestingly, spheres in the crystal phase have more free volume compared to the disordered phase (at the same density).[81]

3.6 MC of hard Spheres confined between two Hard Walls

The model system introduced here was conceived by *Andrea Fortini* during his Dissertation at Utrecht University.[81] The aim is to study the phase behavior of hard spheres confined between two hard parallel plates using MC computer simulations. The physics of confined systems is important in various fields of modern technology such as lubrication and adhesion. Hard sphere systems in which a hard wall is inserted decrease the number of hard-sphere configurations compared to the ordered phases described in Chapter 3.5 and the equilibrium crystal structure can be changed dramatically. Spontaneous formation of crystalline layers with triangular symmetry at the wall gives rise to increasing entropy, whereas the bulk is still a fluid. The model consists of N hard spheres with diameter σ confined between two hard plates of the area $A = L_x L_y$ (Figure 3-10). H is the distance between the two plates and the packing fraction is $\eta = \pi\sigma^3 N/(6AH)$.

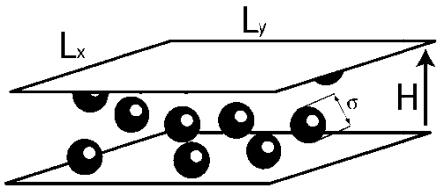

Figure 3-10: Illustration of hard spheres with diameter σ , confined between parallel hard plates of area $A = L_x L_y$ and a separation distance H. Reprinted with permission from[82]. Copyright (2006) by IOP.

The ration L_x/L_y may vary while A and H are fixed. This allows changing the shape of the box, in which MC simulations are performed. Finally, the full equilibrium phase diagram is determined. The free energy F for the resulting equilibrated structures was calculated as a

function of η and H. Figure 3-11 displays the full phase diagram based on free energy calculations in the H-η representation. The white regions of the phase diagram represent the stable one-phase regions. The shaded regions indicate coexistence between fluid and solid or two solid phases, and the dotted region is forbidden as it exceeds the maximum packing fraction of confined hard spheres. At low densities, a stable fluid phase followed by a fluid-solid transition upon increasing the density is observed. The different phases are denoted according to Pieranski[83], where nΔ is a stack of n triangular layers and n□ a stack of n square layers. If $H/\sigma \rightarrow 1$, the stable phase consists of a single triangular layer 1Δ which was found to pack more efficiently than the square layer. The right side of Figure 3-11 depicts the stable solid structures of confined hard spheres corresponding to the phase diagram.

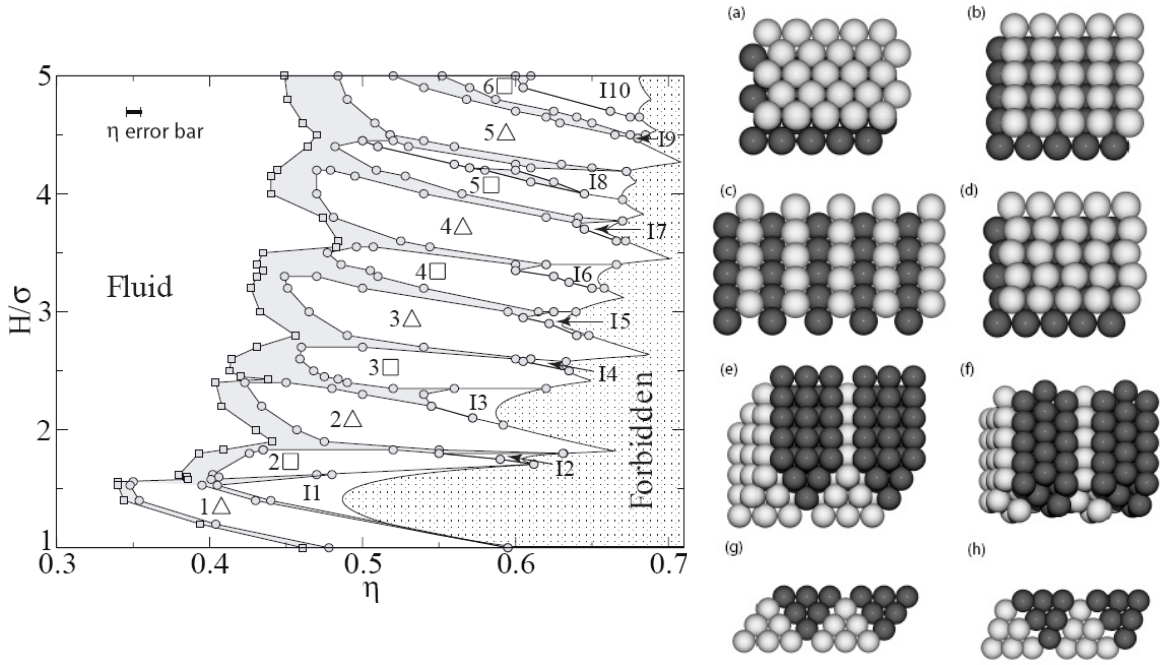

Figure 3-11: (Left) Equilibrium phase diagram of hard spheres with diameter σ confined between two parallel hard walls in the plate separation H - packing fraction η representation. The white, shaded and dotted regions indicate the stable one-phase region, the two-phase coexistence region, and the forbidden region, respectively. (Right) Stable solid structures of confined hard spheres. (a) The triangular phase 2Δ (b) The square phase 2□ (c) The buckling phase 2B (d) The rhombic phase 2R (e),(g) The prism phase with square symmetry 3P□ (f),(h) The prism phase with triangular symmetry 3PΔ. In (a)-(f) the point of view is at an angle of 30° to the z direction. In (g),(h) the point of view is at an angle of 90°. Different shades indicate particles in different planes ((a)-(d)) or particles belonging to different prism structures ((e)-(h)). Reprinted with permission from[82]. Copyright (2006) by IOP.

3.7 Objective of this Thesis

The aim of this thesis is focused on using wrinkled pattern as substrates to guide the self-assembly of nanoparticles. Ordered arrays of nanoparticles form excellent candidates for components of future optical, electronic and magnetic devices. To understand the driving forces of the assembly process we wish to implicate a theoretical model. Monte Carlo computer simulations, carried out in collaboration with the theoretical physics department at the University of Bayreuth (*Prof. Dr. Matthias Schmidt* and *Dr. Andrea Fortini*) aim at determining equilibrium states of a model designed according to the experiments. Given the case that the investigated assembly strategy is general and versatile it can be anticipated that we can widen it to different classes of materials, especially metallic nanoparticles.

Ordered arrays of metal nanoparticles are requested to enhance the signal in surface enhanced Raman spectroscopy (SERS). Such arrays are reckoned to amplify the Raman signal in a predictable way and serve as sensors if adsorbed to a surface. Nanoparticles in regular contact evince an ordered multiplicity of hot spots which can be detected by dark filed microscopy along arrays of nanoparticles and compared to theoretical calculations in cooperation with University of Vigo in Spain (*Weihai N*i and *Dr. Ramón Alvarez-Puebla*).

The second part of this work aims at widening the diversity of wrinkles in terms of materials. Therefore it has to be explored, how the wrinkled structure can be made of a chemically different material than the conventionally used two layer system composed of PDMS and silica in collaboration with the Nees institute in Bonn (*PD Dr. Kerstin Koch* and *Michael Bennemann*). This system suffers from several drawbacks such as dimensional instability and poor resistance against organic solvents. Wrinkles consisting of diverse polymers can open new application fields for example as substrates in microfluidic devices. The present work also aims at elimination of residual stress in the two layer system that occurs within the buckling instability of stiff supported layers under compression.

Not only can the entire material be changed but also the upper surface by coating with hydrophilic molecules out of solution. The aim of this study is to transfer the topographical structure of wrinkles to a chemical structure by means of micro contact printing (μCP). Patterned deposition of polymers is commonly believed to be one of the key steps in the development of novel functional elements and devices in optics, sensorics, electronics and biotechnology. Using wrinkles instead of conventional lithographically fabricated nanostructures

should eliminate environmentally harmful etching processes. The sinusoidal shaped structure consisting of periodic alternating elevations and troughs is expected to provide perfect stamp characteristics. As wrinkles are tunable in terms of wavelength and amplitude, their limits within the μCP process ought to be investigated.

References

1. Kolle, M.; Salgard-Cunha, P. M.; Scherer, M. R. J.; Huang, F. M.; Vukusic, P.; Mahajan, S.; Baumberg, J. J.; Steiner, U. *Nature Nanotechnology* **2010,** *5*, 511-515.
2. Reif, W. E. *Fortschritte der Zoologie* **1985,** *30*, 483-485.
3. Schweikart, A.; Zimin, D.; Handge, U. A.; Bennemann, M.; Altstadt, V.; Fery, A.; Koch, K. *Macromolecular Chemistry and Physics* **2010,** *211*, 259-264.
4. Bhushan,B. *Philosophical Transactions of the Royal Society A* **2009**, *367*, 1445-1486.
5. Feng, L.; Zhang, Y. A.; Xi, J. M.; Zhu, Y.; Wang, N.; Xia, F.; Jiang, L. *Langmuir* **2008,** *24*, 4114-4119.
6. Barthlott, W.; Neinhuis, C. *Planta* **1997,** *202*, 1-8.
7. del Campo, A.; Arzt, E. *Chemical Reviews* **2008,** *108*, 911-945.
8. Haneveld, J.; Jansen, H.; Berenschot, E.; Tas, N.; Elwenspoek, M. *Journal of Micromechanics and Microengineering* **2003,** *13*, S62-S66.
9. Stern, M. B.; Geis, M. W.; Curtin, J. E. *Journal of Vacuum Science & Technology B* **1997,** *15*, 2887-2891.
10. Tas, N. R.; Berenschot, J. W.; Mela, P.; Jansen, H. V.; Elwenspoek, M.; van den Berg, A. *Nano Letters* **2002,** *2*, 1031-1032.
11. Universalatlas, *Diercke Drei,* Westermann, Braunschweig **2011**.
12. swisstopo. TYDAC: Bern, **2011**.
13. Martin, G. C.; Su, T. T.; Loh, I. H.; Balizer, E.; Kowel, S. T.; Kornreich, P. *Journal of Applied Physics* **1982,** *53*, 797-799.
14. Bowden, N.; Brittain, S.; Evans, A. G.; Hutchinson, J. W.; Whitesides, G. M. *Nature* **1998,** *393*, 146-149.
15. Bowden, N.; Huck, W. T. S.; Paul, K. E.; Whitesides, G. M. *Applied Physics Letters* **1999,** *75*, 2557-2559.
16. Huck, W. T. S.; Bowden, N.; Onck, P.; Pardoen, T.; Hutchinson, J. W.; Whitesides, G. M. *Langmuir* **2000,** *16*, 3497-3501.

17. Ohzono, T.; Shimomura, M. *Physical Review B* **2004,** *69*, 132202 (1-4).
18. Efimenko, K.; Rackaitis, M.; Manias, E.; Vaziri, A.; Mahadevan, L.; Genzer, J. *Nature Materials* **2005,** *4*, 293-297.
19. Efimenko, K.; Wallace, W. E.; Genzer, J. *Journal of Colloid and Interface Science* **2002,** *254*, 306-315.
20. Ouyang, M.; Yuan, C.; Muisener, R. J.; Boulares, A.; Koberstein, J. T. *Chemistry of Materials* **2000,** *12*, 1591-1596.
21. Yoo, P. J.; Suh, K. Y.; Park, S. Y.; Lee, H. H. *Advanced Materials* **2002,** *14*, 1383-1387.
22. Chen, X.; Hutchinson, J. W. *Journal of Applied Mechanics-Transactions of the Asme* **2004,** *71*, 597-603.
23. Lin, P. C.; Yang, S. *Appl Phys Lett* **2007,** *90*, 241903 (1-3)
24. Chung, J. Y.; Nolte, A. J.; Stafford, C. M. *Advanced Materials* **2009,** *21*, 1358-1362.
25. Huang, J.; Juszkiewicz, M.; de Jeu, W. H.; Cerda, E.; Emrick, T.; Menon, N.; Russell, T. P. *Science* **2007,** *317*, 650-653.
26. Lu, C.; Möhwald, H.; Fery, A. *Chemistry of Materials* **2008,** *20*, 7052-7059.
27. Chiche, A.; Stafford, C. M.; Cabral, J. T. *Soft Matter* **2008,** *4*, 2360-2364.
28. http://www.halcrow.com/Global/Images/climate_change/rail_buckle_512.jpg (16. Januar **2011**)
29. Biot, M. A. *Journal of Applied Mechanics* **1937,** *4*, A-1
30. Huang, R. *Journal of the Mechanics and Physics of Solids* **2005,** *53*, 63-89.
31. Jiang, H. Q.; Khang, D. Y.; Song, J. Z.; Sun, Y. G.; Huang, Y. G.; Rogers, J. A. *Proceedings of the National Academy of Sciences of the United States of America* **2007,** *104*, 15607-15612.
32. Volynskii, A. L.; Bazhenov, S.; Lebedeva, O. V.; Bakeev, N. F. *Journal of Materials Science* **2000,** *35*, 547-554.
33. Genzer, J.; Groenewold, J. *Soft Matter* **2006,** *2*, 310-323.
34. Groenewold, J. *Physica A: Statistical Mechanics and its Applications* **2001,** *298*, 32-45.
35. Zimmermann, W.; Ziebert, F. In *Technische Berechnungen*: Bayreuth, **2009**.
36. Tarasovs, S.; Andersons, J. *International Journal of Solids and Structures* **2008,** *45*, 593-600.
37. Harrison, C.; Stafford, C. M.; Zhang, W. H.; Karim, A. *Applied Physics Letters* **2004,** *85*, 4016-4018.
38. Stafford, C. M.; Harrison, C.; Beers, K. L.; Karim, A.; Amis, E. J.; Vanlandingham, M. R.; Kim, H. C.; Volksen, W.; Miller, R. D.; Simonyi, E. E. *Nature Materials* **2004,** *3*, 545-550.

39. Nolte, A. J.; Cohen, R. E.; Rubner, M. F. *Macromolecules* **2006,** *39*, 4841-4847.
40. Nolte, A. J.; Rubner, M. F.; Cohen, R. E. *Macromolecules* **2005,** *38*, 5367-5370.
41. Jiang, C.; Singamaneni, S.; Merrick, E.; Tsukruk, V. V. *Nano Letters* **2006,** *6*, 2254-2259.
42. Jiang, C. Y.; Wang, X. Y.; Gunawidjaja, R.; Lin, Y. H.; Gupta, M. K.; Kaplan, D. L.; Naik, R. R.; Tsukruk, V. V. *Advanced Functional Materials* **2007,** *17*, 2229-2237.
43. Lu, C. H.; Donch, I.; Nolte, M.; Fery, A. *Chemistry of Materials* **2006,** *18*, 6204-6210.
44. Chung, J. Y.; Youngblood, J. P.; Stafford, C. M. *Soft Matter* **2007,** *3*, 1163-1169.
45. Genzer, J.; Efimenko, K. *Science* **2000,** *290*, 2130-2133.
46. Lin, P. C.; Vajpayee, S.; Jagota, A.; Hui, C. Y.; Yang, S. *Soft Matter* **2008,** *4*, 1830-1835.
47. Yang, S.; Khare, K.; Lin, P. C. *Advanced Functional Materials* **2010,** *20*, 2550-2564.
48. Efimenko, K.; Finlay, J.; Callow, M. E.; Callow, J. A.; Genzer, J. *Acs Applied Materials & Interfaces* **2009,** *1*, 1031-1040.
49. Schweikart, A.; Fery, A. *Microchim Acta* **2009,** *165*, 249-263.
50. Koh, S. J. *Nanoscale Research Letters* **2007,** *2*, 519-545.
51. Sun, Z.; Yang, B. *Nanoscale Research Letters* **2006,** *1*, 46-56.
52. Hoogenboom, J. P.; Retif, C.; de Bres, E.; de Boer, M. V.; van Langen-Suurling, A. K.; Romijn, J.; van Blaaderen, A. *Nano Letters* **2004,** *4*, 205-208.
53. Hoogenboom, J. P.; van Langen-Suurling, A. K.; Romijn, J.; van Blaaderen, A. *Physical Review Letters* **2003,** *90*, 138301 (1-4).
54. Hoogenboom, J. P.; van Langen-Suurling, A. K.; Romijn, J.; van Blaaderen, A. *Physical Review E* **2004,** *69*, 051602 (1-18).
55. Hynninen, A. P.; Thijssen, J. H. J.; Vermolen, E. C. M.; Dijkstra, M.; Van Blaaderen, A. *Nature Materials* **2007,** *6*, 202-205.
56. van Blaaderen, A.; Hoogenboom, J. P.; Vossen, D. L. J.; Yethiraj, A.; van der Horst, A.; Visscher, K.; Dogterom, M. *Faraday Discussions* **2003,** *123*, 107-119.
57. vanBlaaderen, A.; Ruel, R.; Wiltzius, P. *Nature* **1997,** *385*, 321-324.
58. Kreibig, U.; Vollmer, M. *Optical Properties of Metal Clusters*; Springer-Verlag: Berlin, **1996**.
59. Schlegel, V. L.; Cotton, T. M. *Analytical Chemistry* **1991,** *63*, 241-247.
60. Chen, K. M.; Jiang, X. P.; Kimerling, L. C.; Hammond, P. T. *Langmuir* **2000,** *16*, 7825-7834.
61. Maury, P.; Escalante, M.; Reinhoudt, D.; Huskens, J. *Advanced Materials* **2005,** *17*, 2718-2723.

62. Aizenberg, J.; Braun, P.; Wiltzius, P. *Physical Review Letters* **2000,** *84*, 2997-3000.
63. Xia, Y. N.; Yin, Y. D.; Lu, Y.; McLellan, J. *Advanced Functional Materials* **2003,** *13*, 907-918.
64. Masuda, Y.; Itoh, T.; Itoh, M.; Koumoto, K. *Langmuir* **2004,** *20*, 5588-5592.
65. Mitsui, T.; Wakayama, Y.; Onodera, T.; Takaya, Y.; Oikawa, H. *Nano Letters* **2008,** *8*, 853-858.
66. Hung, A.; Stupp, S. *Nano Letters* **2007,** *7*, 1165-1171.
67. Kim, E.; Y., X.; Whitesides, G. M. *Advanced Materials* **1996,** *8*, 245-247.
68. Xia, Y. N.; Whitesides, G. M. *Annual Review of Materials Science* **1998,** *28*, 153-184.
69. Ohzono, T.; Monobe, H.; Shiokawa, K.; Fujiwara, M.; Shimizu, Y. *Soft Matter* **2009,** *5*, 4658-4664.
70. Lu, C. H.; Mohwald, H.; Fery, A. *Soft Matter* **2007,** *3*, 1530-1536.
71. Horn, A.; Schoberth, H. G.; Hiltl, S.; Chiche, A.; Wang, Q.; Schweikart, A.; Fery, A.; Boker, A. *Faraday Discussions* **2009,** *143*, 143-150.
72. Hyun, D. C.; Moon, G. D.; Cho, E. C.; Jeong, U. Y. *Advanced Functional Materials* **2009,** *19*, 2155-2162.
73. Horn, A.; Hiltl, S.; Fery, A.; Boker, A. *Small* **2010,** *6*, 2122-2125.
74. Allen, M. P.; Tildesley, D. J. *Computer Simulation of Liquids* Oxford University Press: New York, **1987**.
75. Frenkel, D.; Smit, B. *Understanding Molecular Simulation 2nd edition*; Academic Press, **2002**; Vol. 1.
76. Landau, D. P.; Binder, K. *A guide to Monte Carlo simulations in statistical physics*; Cambridge University Press: Cambridge, **2000**.
77. Rapaport, D. C. *The art of molecular dynamics simulation* Cambridge University Press: Cambridge, **1995**.
78. Metropolis, N.; Rosenbluth, A. W.; Rosenbluth, M. N.; Teller, A. H.; Teller, E. *Journal of Chemical Physics* **1953,** *21*, 1087-1092.
79. Alder, B.; Wainwright, T. *Journal of Chemical Physics* **1957,** *27*, 340-242.
80. Pusey, P. N.; vanMegen, W. *Nature* **1986,** *320*, 340-242.
81. Fortini, A., Utrecht University, **2007**.
82. Fortini, A.; Dijkstra, M. *Journal of Physics-Condensed Matter* **2006,** *18*, L371-L378.
83. Pieranski, P.; Strzelecki, L.; Pansu, B. *Physical Review Letters* **1983,** *50*, 900-903.
84. Spuch-Calvar, M.; Rodríguez-Lorenzo, L.; Morales, M. P.; Álvarez-Puebla, R. n. A.; Liz-Marzán, L. M. *The Journal of Physical Chemistry C* **2009,** *113*, 3373-3377.

Chapter 4 Overview of the Thesis

The present dissertation contains five individual publications presented as chapter five to nine. Chapter five to eight are already published, Chapter nine is submitted to *Soft Matter* as highlight article. The first part of the thesis (*Chapter 5* and *Chapter 6*) deals with chemical modification of the wrinkles to make them accessible to different solvents and thus applications that are not feasible using the conventional two layer system composed of poly (dimethylsiloxane) PDMS and a thin silica layer on top. *Chapter 5* presents two different replication methodologies. Different polymers, namely poly (methyl methacrylate) PMMA and epoxy resin are structured. Wrinkles composed of these materials are stable against different solvents on one hand and on the other hand provide mechanical stability compared to the rather soft PDMS. In micro thermoforming, the wrinkled surface is used as a mold (or caliber) to structure different kinds of polymers by pressing the originally wrinkled structure onto a ductile material which preserves the nanostructure after curing. The second methodology employs a molding process, where wrinkles are molded against wax and in a second step, the structured wax is cast against epoxy resin. Both methods reveal perfect copies of the wrinkled original with high fidelity even at dimensions as small as a few hundred nanometers. The fact that wrinkles are hydrophilic after plasma oxidation is used in *Chapter 6*. Wrinkles can therefore be superficially modified by covering them with charged macromolecules out of aqueous solution. As the molecule is only *adsorbed* to the surface it can be transferred to another hydrophilic surface of opposite charge upon conformal contact. The elevated parts of the wrinkles, disconnected by parallel troughs contact said surface and material is transferred onto the flat surface by means of so-called micro contact printing (μCP). Striped nanopatterns of macromolecules are observed. The troughs however remain unoccupied and form inflated channels. At a threshold topology of the stamp where the aspect ratio A/λ drops below 0.11, the μCP process fails because of sparse separation between the wrinkled structure and the flat surface at these dimensions. The second part of the thesis starting with *Chapter 7* uses the finding of *Chapter 6*: nanoparticles are trapped inside said channels of wrinkles in contact with flat surfaces by filling them with a nanoparticle suspension and allowing them to dry. Parallel lines of polystyrene nanoparticles (with radius of 55nm) with spacing according to wrinkles' wavelength are formed. The assembled particle geometry can

be precisely controlled by the initial particle concentration. To understand the formation process, Monte Carlo computer simulations are carried out using a hard sphere model with spheres confined in a box with the same wrinkled geometry as implemented in the experiments. Equilibrium states of the particles are determined for different particle densities and found to be in perfect agreement with the experimentally observed structure of polystyrene particles. The simulation results attest the assembly mechanism to be rather generic and mainly controlled by confinement effects. Different spherical nanoparticles are tested, among them gold colloids having a radius of 33nm. *Chapter 8* deals with optical characterization of parallel lines of gold colloids. Gold colloids in contact within the lines are studied as substrates to enhance the signal in surface enhanced Raman spectroscopy (SERS). The optical properties (determined as scattering intensity from uniform regions using a dark field microspectroscopy setup) are affected by the details of the arrangement within each assembly. Plasmon coupling due to interactions between the electromagnetic fields of neighboring particles occurs and is also simulated by means of the finite-difference time-domain (FDTD) method. Extremely high and uniform enhancement of the Raman signal is measured and could be supported by simulations. *Chapter 9* is disposed to establish a connection between *Chapter 7* and *Chapter 8*. The relevance of wrinkles as a tool to assist self-assembly compared to conventionally lithographic structures is highlighted as well as the high potential of structured gold colloids by means of wrinkle-assisted assembly.

Individual Contributions to joint Publications

Chapter 5

This work is published in *Macromolecular Chemistry and Physics* (**2010**, *211*, 259-264) under the title:

"**Fabrication of Artificial Petal Sculptures by Replication of Sub-micron Surface Wrinkles"**
by Alexandra Schweikart, Denys Zimin, Ulrich A. Handge, Michael Bennemann, Volker Altstädt, Andreas Fery and Kerstin Koch

I processed the micro thermoforming experiments and wrote the manuscript. Denys Zimin and Ulrich A. Handge carried out some of the experiments and corrected the manuscript. Michael Bennemann and Kerstin Koch performed the molding experiments and corrected the manuscript. Volker Altstädt and Andreas Fery supervised the project and corrected the manuscript.

Chapter 6

This work is published in *Langmuir* (**2008**, *24*, 12748-12753) under the title:

"A Lithography-Free Pathway for Chemical Microstructuring of Macromolecules from Aqueous Solution Based on Wrinkling"
by Melanie Pretzl, Alexandra Schweikart, Christoph Hanske, Arnaud Chiche, Ute Zettl, Anne Horn, Alexander Böker and Andreas Fery

I fabricated the wrinkled stamps, carried out the AFM measurements, performed the image analysis and wrote the manuscript. Melanie Pretzl and Christoph Hanske carried out the micro contact printing experiments and wrote the manuscript. Arnaud Chiche, Anne Horn, Ute Zettl and Alexander Böker were involved in discussions and corrected the manuscript. Andreas Fery analyzed the results and corrected the manuscript.

Chapter 7

This work is published in *Soft Matter* (**2010**, *6*, 5860-5863) under the title:

"Nanoparticle Assembly by Confinement in Wrinkles: Experiments and Simulations"
by Alexandra Schweikart, Andrea Fortini, Alexander Wittemann, Matthias Schmidt and Andreas Fery

I carried out all the described experiments and wrote the manuscript. Alexander Wittemann synthesized the colloidal particles. Andrea Fortini and Matthias Schmidt conceived the theoretical model. Andrea Fortini performed the computer simulations. Matthias Schmidt and Andreas Fery supervised the project and wrote the manuscript.

Chapter 8

This work is published in *Chemical Science* (**2010**, *1*, 174-178) under the title:

"Highly Uniform SERS Substrates formed by Wrinkle-Confined drying of Gold Colloids"
by Nicolás Pazos-Pérez, Weihai Ni, Alexandra Schweikart, Ramón A. Alvarez-Puebla, Andreas Fery and Luis M. Liz-Marzán

I performed the assembly experiments of nanoparticles, carried out the SEM imaging and corrected the manuscript. Nicolás Pazos-Pérez synthesized the particles and wrote the manuscript. Weihai Ni and Ramón A. Alvarez-Puebla performed the SERS measurements and carried out FDTD simulations. They also wrote the manuscript. Andreas Fery and Luis M. Liz-Marzán supervised the project and corrected the manuscript.

Chapter 9

This work is published in Soft Matter (**2011**, *7*, 4093-4100) as a highlight article under the title:

"Controlling inter-Nanoparticle Coupling by Wrinkle-Assisted Assembly"
by Alexandra Schweikart, Nicolás Pazos-Pérez, Ramón A. Alvarez-Puebla and Andreas Fery

All authors discussed the results and wrote the manuscript.

Fabrication of Artificial Petal Sculptures by Replication of Sub-micron Surface Wrinkles

Poly (dimethylsiloxane) (PDMS) is mainly used as a soft elastomeric support for controlled wrinkling. This material suffers from low dimensional stability and tends to swell in organic solvents. Additionally, wrinkles fabricated through a buckling instability are not tension free on the microscopic level and suffer from relaxation on a longer time scale. Chapter 5 picks up the amount and diversity of drawbacks and focuses on two replication methods; micro thermoforming (or "hot embossing") and molding. We found that surfaces wrinkled on the sub-micron scale can be used as templates for a micro thermoforming process. This allows structural transfer of the nanoscopic pattern onto different materials, especially thermoplastic polymers. As an example, we structured poly (methyl methacrylate) (PMMA) by heating PMMA above its glass transition temperature (T_g) und pressed a wrinkled stamp against the material using a hydraulic lab press (Figure 4-1).

Figure 4-1: Schematic of the micro thermoforming process. A thermoplastic polymer is heated above its glass transition temperature and the wrinkled stamp is pressed against it. The thermoplast adopts the structure and preserves it after removing the stamp and cooling.

The original wrinkled stamp geometry could be preserved and used in several reproduction cycles. Comparison of a wrinkled PDMS stamp and the micro thermoformed PMMA surface showed appropriate mapping of the original onto the new material. As this is a one step process, only a negative of the PDMS original could be obtained which is evident and visible as the former cracks appear as elevated parts as the cracks are filled with the thermoplast during the thermoforming process. If a positive copy of the structure is desired, a two-step process has to be performed. To realize this aim, we carried out a replication process, where the original stamp is molded using a fine-grained wax which is sensitive to adapt the sinusoidal shaped structure of the wrinkles. Subsequently the new structure was mapped onto an epoxy resin material by casting the epoxy onto the structure. Figure 4-2 shows that such a process can copy the wrinkled nanostructure with high fidelity; Figure 4-2a depicts a SEM image of PDMS wrinkles before molding. Figure 4-2b shows wrinkles made of epoxy resin after the molding procedure. Cracks are indicated by arrows.

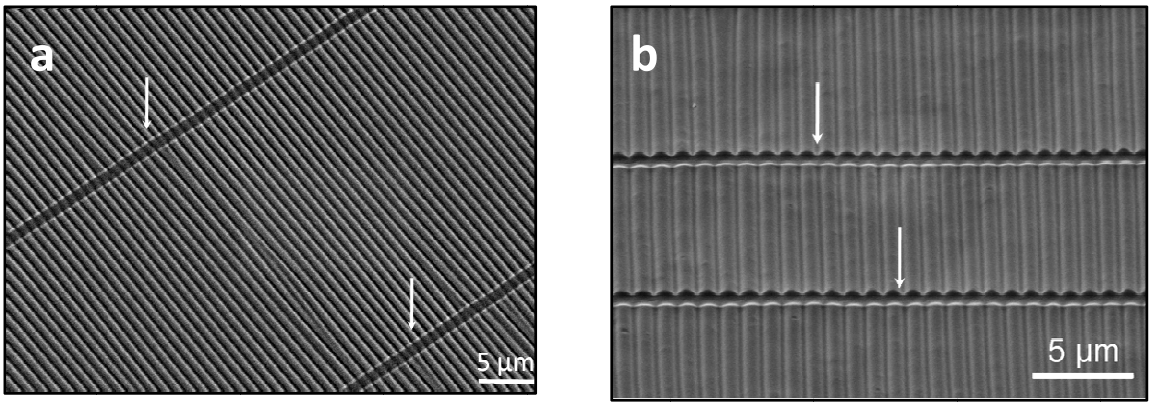

Figure 4-2: (a) SEM image of original wrinkled surface. Cracks appear perpendicular to the wrinkle direction marked by arrows. (b) SEM image of replicated epoxy resin surface. Cracks are visible perpendicular to the sinusoidal shaped wrinkles marked with arrows.

The structure adapted by the wax served as a caliber and could be molded again in additional cycles using epoxy resin. As the final wrinkled structures consist of only one component (either epoxy resin or PMMA), no residual stresses remain and relaxation processes have thus been eliminated.

A Lithography-Free Pathway for Chemical Microstructuring of Macromolecules from Aqueous Solution Based on Wrinkling

The previous chapter investigated how the wrinkled nanostructure can be transferred into different polymers. Chapter 6 focuses on using wrinkled surfaces as stamps for micro contact printing. We explore how the topographical contrast of the wrinkled structure can be used to create a chemical contrast by micro contact printing (μCP). While for classical μCP lithographically produced masters are needed, we show that controlled wrinkling can serve as an alternative pathway to producing such masters. We show that even sub-micron periodicities are feasible. Hydrophilized wrinkled surfaces could be coated with a monolayer of positively charged macromolecules (poly (allylamine hydrochloride) (PAH)) out of aqueous suspensions. Additionally, a glass surface was coated with a polyelectrolyte multilayer terminating in a negatively charged poly (styrene sulfonate), (PSS) layer to smoothen the surface and to provide opposite charging. If the macromolecule-coated wrinkled structure was brought into contact with this multilayer coated surface, material was transferred from the elevated parts of the wrinkles onto the flat surface. Figure 4-3 depicts an AFM height images taken after such micro-contact printing experiment using a wrinkled stamp with 743nm and 150nm wavelength and amplitude, respectively. Atomic Force Microscopy (AFM) measurements proofed the height of the printed structure to be approximately 7nm.

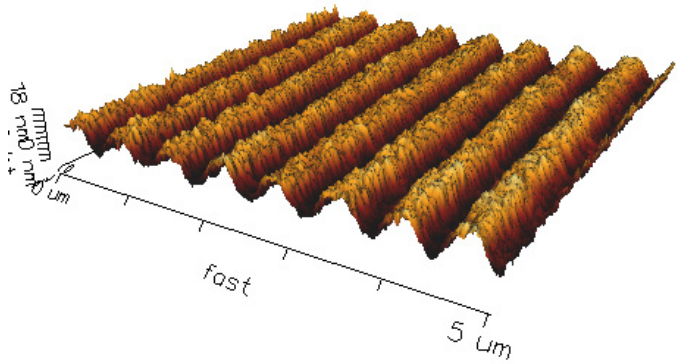

Figure 4-3: AFM 3d height image of a structure prepared by μCP using the polyelctrolyte PAH as ink with wrinkled stamp. Stamp geometry is 743nm wavelength and 150nm amplitude. The height above the substrate of the resulting pattern is approximately 7nm.

As the aspect ratio A/λ was not constant during the experiments but tended to a plateau, the influence of the aspect ratio towards successful printing processes is investigated. As the wavelength and amplitude could be easily adjusted via the height of the thin film h (see equation 3.16) we varied the height by different plasma exposure times. Resulting wavelength and amplitude of the wrinkles ranged from λ = 302nm to 931nm and A = 25nm to 200nm, respectively. Figure 4-4 shows a set of AFM measurements performed on the surfaces after μCP with said stamps. It could be stated that below a critical amplitude of 40nm and wavelengths below 335nm ($A/\lambda < 0.11$) no selective transfer from the wrinkled stamp was possible. The whole surface was covered by macromolecules (Figure 4-4a). With increasing topology, the printed structure was found to broaden and move apart following the periodicity of the wrinkled original (Figure 4b-g).

The reason for the disappearance of the features was examined by taking the ratio of printed areas (areas, where ink is transferred by the stamp represented by bright stripes in Figure 4-4) and non-printed areas (represented by dark stripes in Figure 4-4) on the substrate into account. The size of the non-printed area decreases with decreasing amplitude and wavelength of the PDMS stamp and dropped to 0% for sample *a* (Figure 4-5a).

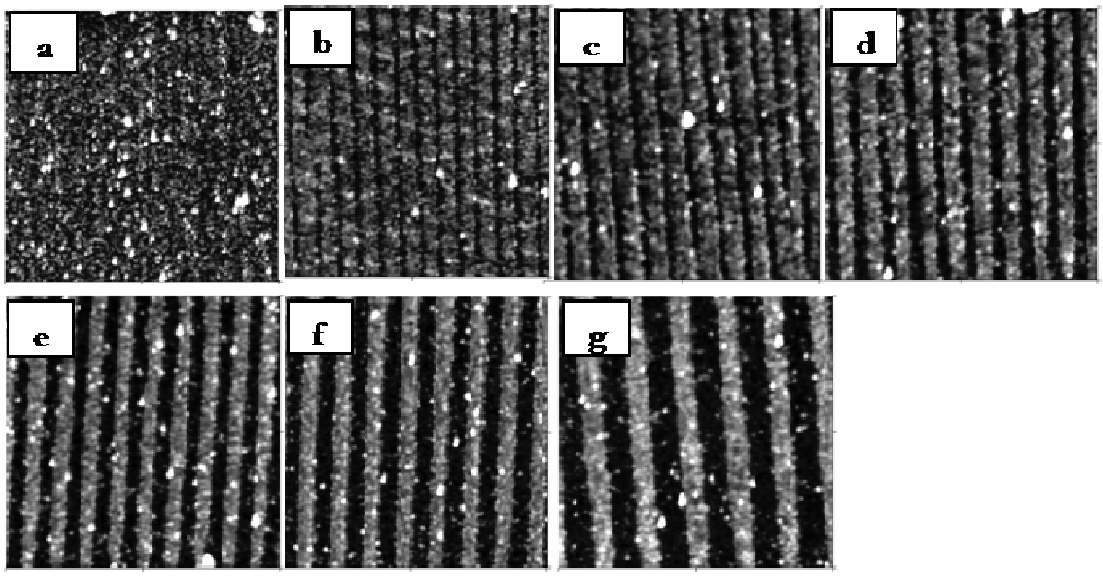

Figure 4-4: AFM height images (scan size 5μm^2) of PAH-Rho as ink on substrates coated with a polyelectrolyte multilayer. The amplitudes and wavelengths of the used PDMS stamps are increasing from (a) to(g) as (A_a) 25nm, (λ_a) 302nm; (A_b) 40nm, (λ_b) 355nm; (A_c) 60nm, (λ_c) 426nm; (A_d) 80nm, (λ_d) 496nm; (A_e) 100nm, (λ_e) 602nm; (A_f) 150nm, (λ_f) 743nm; (A_g) 200nm, (λ_g). For sample (b), it can be clearly seen that the transfer of the pattern starts to fail; the pattern broadens and converges for amplitudes below 40nm and wavelengths below 355nm.

The peaks on the wrinkled stamp approached each other and the height diminished. Thus, more peaks contacted the template and with decreasing amplitude and wavelength, ink was transferred from the peaks as well as from the valleys of the stamp. The non-printed areas vanished below wavelength of 426nm and amplitudes of 40nm (end of the linear regime in Figure 4-5a) which marks the lower limit of our application. It should be marked that thus non-printed areas could be much smaller than the actual λ of the stamp (approximately 50nm, see dark lines in Figure 4-4b). We measured the height of the printed structure above the substrate by AFM and plotted it versus the amplitude of the wrinkled stamp. Figure 4-5b shows increasing height of the structure until a plateau is reached at amplitudes above 80nm with a constant height of the printed structure between 6nm and 7nm. For λ below 355nm and A below 40nm the mean height dropped to zero, indicating again the disappearance of the printed features. The scope of this method can be widened -but is not limited to- different macromolecules like proteins (bovine serum albumin) and thiols.

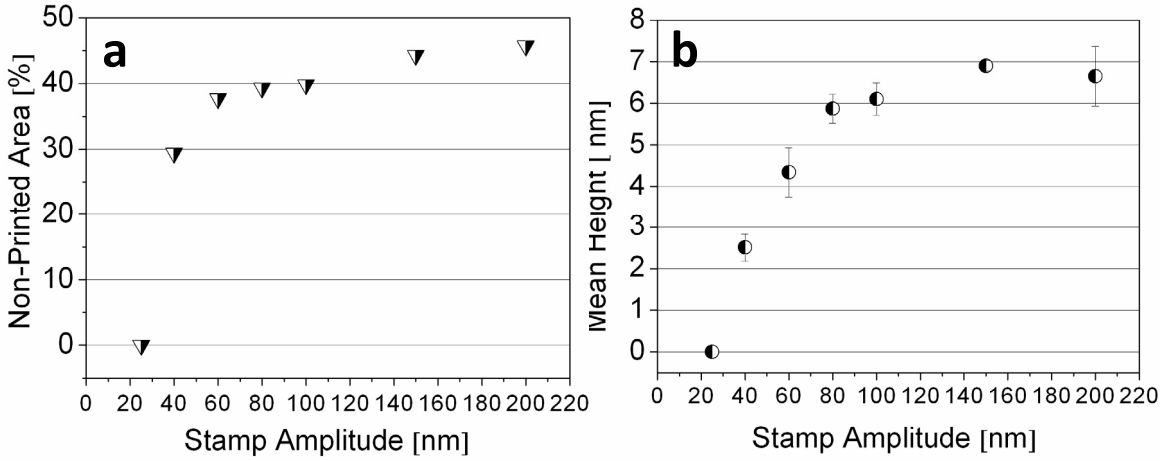

Figure 4-5: (a) Decrease of the non-printed areas as percentage of the template (25μm^2) with decreasing amplitude. Below an amplitude of 60nm (wavelength of 426nm), the end of the linear regime is reached and the non-printed areas vanish to 0% for sample a (A_a) 25 nm, (λ_a) 302 nm). (b) Plot of mean height of each sample against amplitude clearly shows that a constant value is reached for amplitudes above 80nm and above a corresponding wavelength of 496nm.

Nanoparticle Assembly by Confinement in Wrinkles: Experiments and Simulations

In Chapter 7 we benefit from the fact that channels form upon conformal contact between a wrinkled surface and a flat substrate. Such channels were used to confine nanoparticles out of aqueous suspensions. Therefore, a drop of particle suspension containing polystyrene beads with r = 55nm was placed onto a hydrophilic glass substrate. A wrinkled substrate placed on top of the drop formed disconnected channels as soon as the two surfaces touched each other. The system was left to dry and the wrinkled surface is removed. Surprisingly, we found that different patterns can be created from the same stamp when using solutions of different particle concentration. Scanning Electron Microscopy was used to determine the final particle geometry and density of the particles (Figure 4-6, left column). Single parallel lines of particles could be observed at low particle concentration whereas higher particle concentration yielded particle lines with triangular symmetry because of the adjacent, sinusoidal shaped walls and the flat wall. We found the type of observed structure (denoted as the linear density ρ) to be linearly dependent on the on the initial particle concentration Φ (Figure 4-6f).

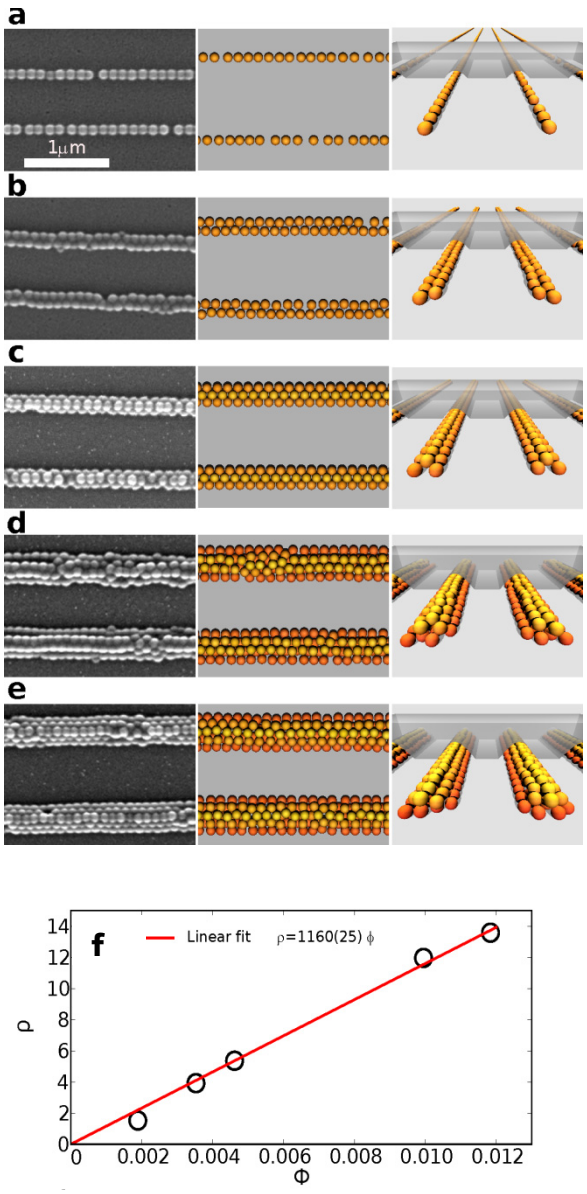

Figure 4-6: (a-e) Sequence of structures found experimentally with SEM (left column) and in simulations, shown from the top (middle column) and along the channels (right column). The concentration increases from (a) to (e), leading to structures that range from single-file wires to prisms with triangular cross section. The transparent grey shape represents the sinusoidal wall and is shown only partially for clarity. (f) Experimental results (symbols) for the dependence of the linear density ρ of assembled particles on the initial volume fraction Φ of particles in the dispersion. The line is a linear fit to the data.

In this paper we carried out Monte Carlo computer simulations to test whether confinement plays a dominant role is the assembly process. Therefore we simulated hard spheres in a box holding similar geometries to the actual channel geometry in the experiments. In fact, after equilibration of the simulation we observed equal particle assemblies shown in Figure 4-6 middle (top-view) and right (perspective-view) column. Because of the sinusoidal shape of the wrinkles, the confining geometry represents triangular cross section (Figure 4-7).

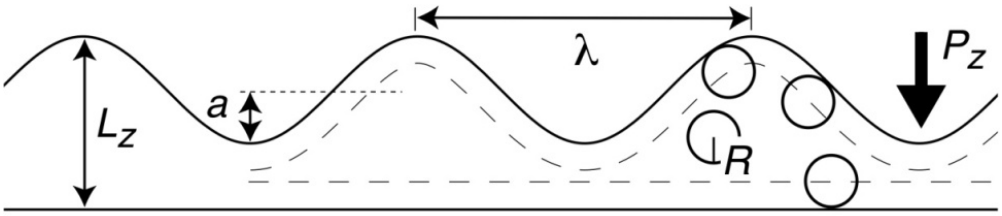

Figure 4-7: Illustration of the theoretical model of hard spheres with radius *R* confined between a (lower) smooth hard wall and an (upper) hard wall with sinusoidal shape of wavelength *λ* and amplitude *a*. The (maximal) distance between both walls is denoted by L_z. The pressure acts on the top wall; the lower wall is kept fixed. The dashed lines indicate the depletion zones that are inaccessible to the particle centers, due to interactions of the particles with the walls.

Depletion between the walls and the trapped particles give rise to pyramidal shaped particle lines with more than two particles within one line. As a consequence, we found prism-like particle assemblies for more than two particles per line in the experiments as well as in simulations leading to the conclusion that confinement plays an eminent role in the assembly mechanism. Finally we compared the relevant geometries, namely the height *h* and the base *b* of the assembled particle lines and compared experimental results and theoretical predictions according to MC simulations. The results are draft in Figure 4-8, where open symbol represent experimental findings and filled symbols obtained by simulations. We found quantitative agreement of the results from the two approaches for the variation of *h* with *ρ*. The height *h* was consistently smaller in the experiments compared to simulations which could be due to shrinking of the particles upon drying while the hard spheres in the simulation remain firm.

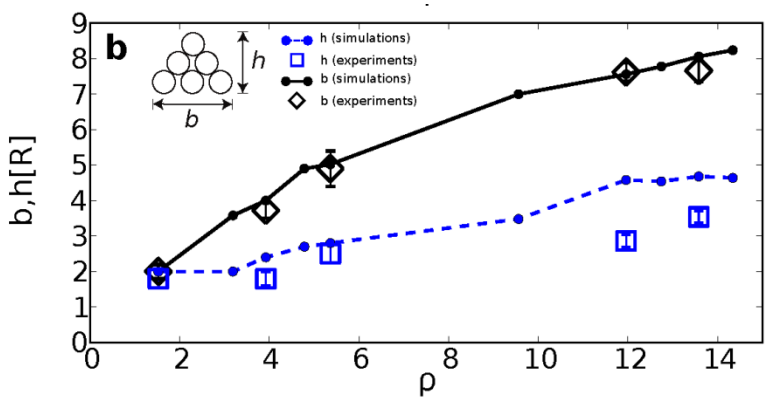

Figure 4-8: Variation of the geometry of the colloidal structures with their density *ρ*. Shown are the height *h* and base *b* of the prism structures (see inset for a cross section) in units of particle radius *R* as obtained in simulations (filled symbols joined by lines to guide the eye) and AFM measurements (open symbols with error bars).

We also showed in this chapter how more complex interconnected grid-like particle assemblies can be created, if two crossed wrinkled surfaces act as confinement that could again be reproduced in simulation. The structures showed interesting chiral nature and their applicability as meatamaterials will be investigated in the future.

Highly Uniform SERS Substrates formed by Wrinkle-Confined drying of Gold Colloids

In this contribution we demonstrate, how parallel assemblies of gold nanoparticles assembled according to the method presented in Chapter 7 can be used to amplify the signal in surface enhanced Raman scattering (SERS). CTAB stabilized gold nanoparticles of r = 33nm in diameter were synthesized and explored. Using different topologies of wrinkles (different wavelength and amplitude) different spacing between the lines as well as different type of lines were obtained. Single lines with a spacing of 340nm as well as lines consisting of two particles with a spacing of 500nm were fabricated following the periodicity of the wrinkled original (Figure 4-9).

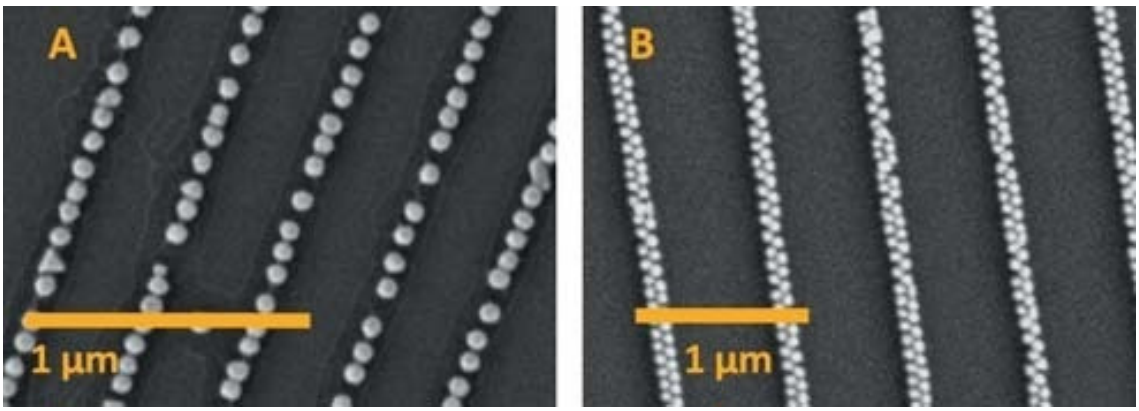

Figure 4-9: Scanning electron microscopy (SEM) images of two different stamped films, comprising single-line (A) and double-line (B) arrays of gold nanoparticles, upon confinement of a monodisperse gold colloid with wrinkled stamps of varying dimensions. Wrinkle wavelength and depth were determined by AFM to be 340 and 23nm in (A); 500nm and 77nm in (B).

The modality of the nanoparticle assembly affects the optical properties. Dark filed microscopy was performed along the lines. The localized surface plasmon resonance was found to be red-shifted (593nm and 601nm for the single-and double-line arrays, respectively) with respect to the dilute gold colloid (539nm), as a consequence of plasmon coupling due to interactions between the electromagnetic fields of adjacent particles. The experimentally measured spectra could be compared to a theoretically calculated model by means of the finite-different time-domain method (FDTD). As the experimental values suggested, the electro-

magnetic field along the particle lines is erratically distributed with strong enhancements exactly located at the gaps between two nanoparticles leading to hot spots. These hot spots are shown as red areas in Figure 4-10C and Figure 4-10D, where results for FDTD simulations are shown for similar line structures like in the experiments.

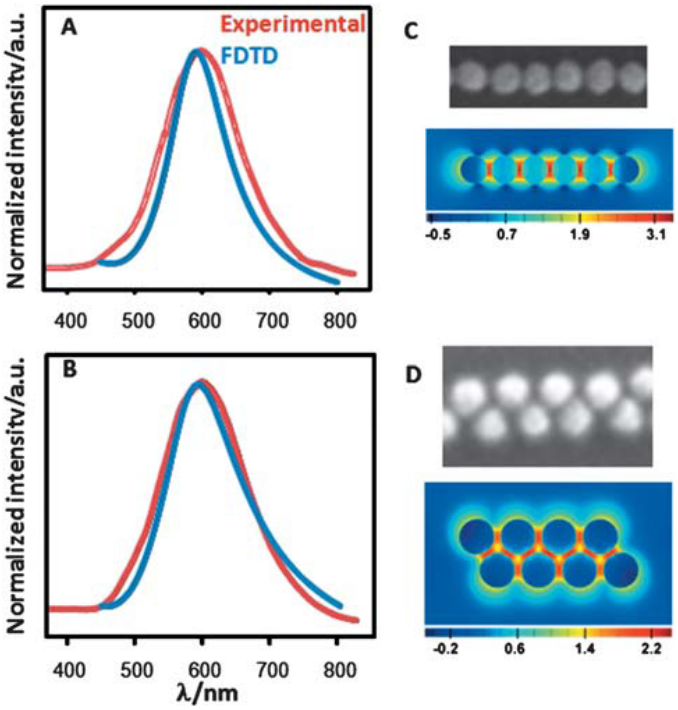

Figure 4-10: (A,B) Normalized experimental and calculated localized surface plasmon resonance bands for single-line (A) and double-line (B) films. (C,D) Electric field intensity enhancement contours at a logarithmic scale for a single-line (C) Au nanoparticle array (excitation polarization along the x axis; mesh size 1 nm) and double-line (D) Au nanoparticle array (the profile was averaged over excitation polarizations at 0, 90, -58, and 58 degrees referred to the x axis; mesh size is 1.5 nm; contours are plotted in the xy plane).

Finally, the optical enhancement properties were investigated using a laser excitation wavelength of 633nm compared to a physically evaporated gold island film which is used as a substrate for SERS by default. In this contribution we show that the intensity of the SERS signal is highly uniform in contrast to the gold island film. Naturally, the average intensity of the gold island films exceeded the intensity of the single and double line array as the total number of particles was much higher in the gold island film. However, counting the total number of particles per unit area and comparing it to the measured intensities, the array of particles had a striking three-fold and two-fold larger intensity, respectively compared to the gold island film. An additional demonstration of the homogenous intensity provided by the substrate was obtained by sampling a large area of the single-line array. Using wrinkle-assisted self-assembly it is possible to control the organization of the colloidal particles on the sub-

strate, with a consequent control over the formation of hot spots and the resulting SERS intensity, thus providing highly-sensitive quantitative platforms.

Controlling inter-Nanoparticle Coupling by Wrinkle-Assisted Assembly

This paper focuses on recent advances in controlling inter-nanoparticle coupling effects by wrinkle-assited self-assembly of nanoparticles. This paper aims to interconnect the experimental and theoretical work done in Chapter 7 with the subsequent application in Chapter 8. We elaborate on the method presented in Chapter 7, where nanoparticles out of suspension can be periodically assembled onto flat surfaces by using wrinkles. The two parameters to control the assembled geometry of particles are either the particle concentration (as shown in Chapter 7) or the size of the wrinkles (Chapter 8). By tailoring the exact placement of metal naoparticles we were able to control coupling effects between nanoparticles. Such distance-dependent effects are for example coupling of the localized surface Plasmon resonance. We show how we can use the method described in Chapter 7 to pre-control the formation of hot spot arrays between ordered gold nanoparticles. Such arrays give rise to a geometry dependent SERS signal and can be used to create substrates for quantitative SERS measurements.

Chapter 5 Fabrication of Artificial Petal Sculptures by Replication of Sub-micron Surface Wrinkles

Full Paper

Macromolecular Journals

Macromolecular Chemistry and Physics

Fabrication of Artificial Petal Sculptures by Replication of Sub-micron Surface Wrinkles

We dedicate this contribution to Prof. Ringsdorf

Alexandra Schweikart, Denys Zimin, Ulrich A. Handge, Michael Bennemann, Volker Altstädt, Andreas Fery,* Kerstin Koch

In this contribution, we discuss wrinkling as a process resulting in well-defined periodic micron-sized structures, as known from the interface of several plant cells. We show possible pathways to transfer this principle to artificial materials such as epoxy resins or polymers. While topographical structuring of surfaces by wrinkling is meanwhile well established for elastomers like poly (dimethyl siloxane), so far the step towards other classes of materials has not been taken. This puts several limitations to potential applications of artificial wrinkled structures, as elastomers show poor dimensional stability, low optical quality, and tend to swell in organic solvents. As well, artificial structures formed by wrinkling are not tension-free on the microscopic level, which makes them metastable. Residual mechanical tensions can affect dimensional stability on long timescales. We introduce two processes, micro thermoforming and molding, as means to overcome these restrictions and to pattern non-elastomeric materials by using wrinkled elastomers as templates. The two approaches allow the formation of negative and positive replicas and allow the transfer of sub-micron features with high fidelity.

Introduction

Wrinkling in Plant Systems and Biomimetic Approaches for Artificial Surfaces

The fabrication of micro- and nanostructured surfaces is of broad interest for the development of functional materials with various outstanding properties. In accordance with the chemical property of the material nanostructures cause low or high wettability,[1] special adhesion properties[2] and possess unique capabilities for the development of bioactive structures for medical use.[3] Nanostructured materials provide specific optical appearances, such as velvety[4] and iridescence.[5,6] In nature, a huge variety of functional surface structures have been developed by evolution. One of the principles underlying structure formation in biological systems is wrinkling – mechanical instability of thin sheets upon in-plane compression. While macroscopic examples

A. Schweikart, D. Zimin, A. Fery
University of Bayreuth, Universitätsstraße 30, D-95440 Bayreuth, Germany
Fax: +(49) 921 55 2059; E-mail: andreas.fery@uni-bayreuth.de
U. A. Handge, V. Altstädt
Department of Polymer Engineering, University of Bayreuth, Universitätsstraße 30, D-95440 Bayreuth, Germany
M. Bennemann
Nees Institute for Biodiversity of Plants, Rheinische Friedrich-Wilhelms University of Bonn, Meckenheimer Allee 170, D-53115 Bonn, Germany
K. Koch
Department of Biology and Nanobiotechnology, University of Applied Science, Rhine-Wall, Kleve, Landwehr 4, D-47533 Kleve, Germany

Macromol. Chem. Phys. **2010**, *211*, 259–264

DOI: 10.1002/macp.200900543

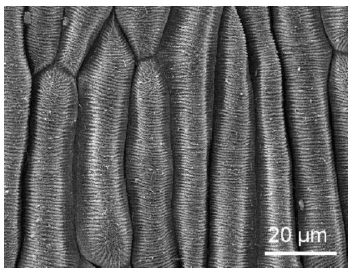

Figure 1. SEM image of cuticular folds of a petal (flower leaf) of Daisies (*Bellis perennis*) with elongated cells and parallel orientated cuticular folds.

like wrinkling of human skin are well known,[7,8] nature provides as well examples of micron- and sub-micron periodic structures that are formed along the same principle: In plants cuticular folds can be found on seed, leaf and most frequently on flower petals.[9] Cuticular folds are sculptures caused by folding of the plant cuticle or caused by a wavy structure of the underlying cell wall.[10] Cuticular folds occur in irregular pattern, but also exist as parallel folds. The number of folds within a line of 20 μm varies from 2 to 35.[11] Figure 1 shows a typical example of cuticular folds of a petal (flower leaf) of Daisies (*Bellis perennis*). In Daisies petals the cuticular folds have an average height of 360 nm with standard deviation (σ) of 40, width of 410 nm ($\sigma = 70$) and a distance of 530 nm ($\sigma = 150$). The average amount of folds is 21 per 20 μm.

In combination with a micro-roughness, formed by papillae shaped cells, cuticular folds can cause superhydrophobicity with static contact angles of about 150°. However, water droplets showed also a large hysteresis, leading to adhering droplets even at 90° tilt angle of the surfaces.[12]

In the last decade, the wrinkling process has been established for creating topographically structured artificial surfaces.[5,13–16] A convenient way of creating oriented wrinkles is preparation of a hard surface layer on stretched elastomers and subsequent release of stretching, as reported in ref. [17–22] and also reviewed in ref.[8,23] Figure 2 illustrates the principle of wrinkle-formation.

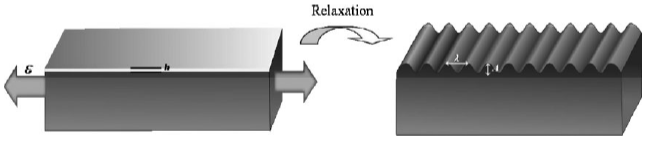

Figure 2. Principle of the formation of periodic surface wrinkles. A soft material provided by a hard film (thickness h) in a stretched state forms wrinkles of the amplitude A and wavelength λ, when the strain is released.

While wrinkle-orientation with similar and even smaller periodicities as in the natural examples can be achieved, application is limited by two factors.

i. Elastomers are not convenient as substrates for many applications due to their poor dimensional stability.
ii. The wrinkles are not tension-free on the microscopic scale. Therefore, they are metastable. Residual mechanical tensions can affect dimensional stability on long timescales. For example, ageing processes are observed, which result in a gradual decrease of the amplitude of the patterns. As well, local stretching can result in a decrease of the amplitude in the vicinity, as tensions can relax when the film is broken at a point.
iii. Elastomers have poor optical properties, which rules out potential application as optical building blocks like gratings. While PDMS is optically clear, it is not homogenous in its refractive index. PDMS is not commonly used for lenses for this reason. PMMA is a material, which is commonly used in lenses.

Here we explore the possibility to eliminate these drawbacks by a molding process. We show that wrinkled structures can serve as templates for molding [24] or micro thermoforming ('hot embossing').[25] The features of the structures can be successfully transferred to different materials, namely epoxy resin and poly (methyl methacrylate) (PMMA). In both methods, the structured original can be used as a flexible stamp for several replication cycles without loss of the features.

By micro thermoforming a stamp is used (usually fabricated from metal) to define the pattern in a polymer that is softened by heating it above its glass transition temperature (T_g). A wide variety of polymers have been micro thermoformed by features on the micron scale and below, especially polycarbonate and PMMA. Most prominent examples for micro thermoformed mass-produced articles are compact discs (CD) where a micro-structured pit-and-land surface is replicated using a metal caliber.[26] By this micro replication process, modifications of the film to be formed remain preserved beyond the forming process. High-resolved micro- and nano-patterns even behind undercuts can be replicated.

Here, we show that both negative (by hot embossing) and positive (by a two-step molding process) replica of wrinkled structures can be formed with high fidelity.

Experimental Part

Fabrication of Sub-micron PDMS Wrinkled Foils

Wrinkles were formed by exposure of a poly (dimethyl siloxane) (PDMS) substrate to an

Macromol. Chem. Phys. **2010**, *211*, 259–264

Macromolecular Journals

DOI: 10.1002/macp.200900543

oxygen plasma which creates a stiff thin silica-like layer on the topmost layer of the PDMS.[5,14,27,28] Before, the PDMS sheet is stretched uniaxially and release of stretching after the plasma treatment. The PDMS elastomer was prepared by mixing Sylgard 184® (purchased from Dow Corning, Midland, USA) with a 10:1 ratio by mass of pre-polymer to curing agent. The mixture was stirred for 10 min and filled in a carefully cleaned, plain glass dishes. After 24 h at RT and baking at 60 °C for 2 h, the cross-linked PDMS with a thickness of 2 mm was cut into 30 mm ×6 mm stripes. These were clamped and stretched uniaxially in a customer-made apparatus to a length of 125% of their original length. The stretched substrates were oxidized between 90 s and 500 s in oxygen plasma at 0.2 mbar using a plasma etcher operating at 0.1 KW (flecto10, Plasma Technology, Germany). After cooling to RT, the samples were relaxed with a strain releasing rate of 33 $\mu m \cdot s^{-1}$. The so structured master foils were examined by AFM and SEM before and after molding.

Negative Replication of the Wrinkled Sculptures by Micro Thermoforming ('Hot Embossing')

Micro thermoforming is a commercially widely used process.[25] The polymer poly(methyl methacrylate) (Plexiglas 6N®, Evonik, Darmstadt, Germany) was first shaped into plates of 3 cm in length, 0.6 cm in width and 1 mm in thickness. A hydraulic lab press PW10 (Paul-Otto Weber GmbH, Remshalden, Germany) was used as shown in Figure 3. The PMMA platelet was placed into a caliber made of brass and the wrinkled stamp was placed onto the PMMA. Subsequently, the two materials were sandwiched between a press and heated by two metal plates to 200 °C (above the T_g of PMMA of 118 °C). Then, a force of 31 kN was applied. After 300 s, the pressure was released and the metal plates were allowed to cool down. Then, the PDMS stamp was separated from the PMMA.

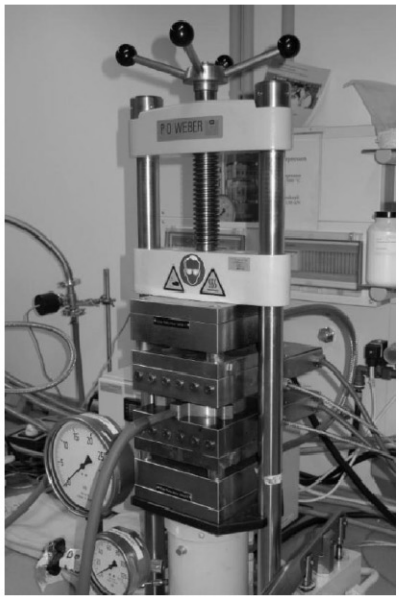

Figure 3. Hydraulic lab press for the micro thermoforming process: the PMMA platelet and the structured PDMS were sandwiched between two metal plates under pressure and heated above the T_g of PMMA to render it soft.

The PDMS stamp and the PMMA duplicate were examined using AFM.

Positive Replication of the Wrinkled Sculptures by Molding with Epoxy Resin

In order to achieve positive replica of wrinkled surfaces, a two-step molding process was used to transfer the surface sculptures of the PDMS substrates into epoxy material.[24] First, poly (vinyl siloxane) dental wax (President Light Body® Gel, ISO 4823, poly (vinyl siloxane) (PLB), Coltene Whaledent, Hamburg, Germany) was applied via a dispenser on the PDMS surface and immediately pressed down with a glass plate. After complete hardening of the dental wax (at 21–23° approximately 5 min), the master surface and the mold (negative) were separated. After a relaxation time of 30 min for the molding material, the produced negative replicas were filled up with an epoxy resin (Epoxydharz L®, No. 236349, Conrad Electronics, Hirschau, Germany), mixed with a hardener (10 parts epoxy, 4 parts hardener) (Härter S, Nr 236365, Conrad Electronics, Hirschau, Germany).

Specimens were immediately transferred to a vacuum chamber at 1 mbar for approximately 1 min to remove trapped air and to increase the resin infiltration through the structures. After hardening (24 h at 22 °C, or 3 h at 50 °C), the positives replica were separated from the negative replica. The last fabrication step can be repeated several times to generate a number of duplicates.

SEM

For scanning electron microscopy (SEM) (Cambride Stereoscan 200 SEM, Zeiss GmbH, Oberkochen, Germany) specimens were fixed on a specimen holder with a double side adhesive tape and coated with an approximately 20 nm thick gold layer in a sputter coater (Balzers Union SCD 040, Balzers-Pfeifer GmbH, Aßlar).

AFM

Atomic force microscope (AFM) images were obtained using a commercial Multimode atomic force microscope (Veeco Instruments Inc., USA) operating in the tapping mode with silicone cantilevers (force constant 34.0–58.7 $N \cdot m^{-1}$) and a typical frequency of 330 kHz was used.

Results and Discussion

The periodic wrinkled surface was first investigated using AFM and SEM to confirm the original structure of the master and to determine the wavelength and amplitude of the pattern. For the sake of simplicity, we report here only on

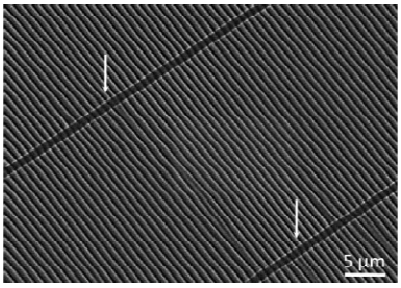

Figure 4. SEM image of original wrinkled surface. Cracks appear perpendicular to the wrinkle direction marked by arrows.

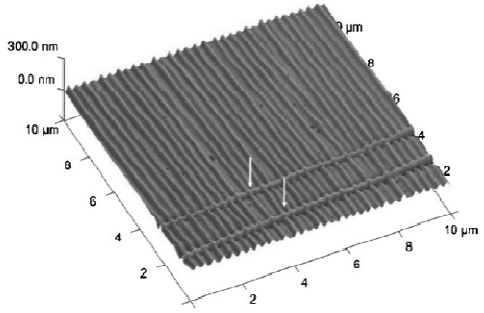

Figure 5. 3D AFM height-image of structured PMMA produced by micro thermoforming. Cracks are visible filled with PMMA of the same height as the structures' amplitude as indicated by arrows.

one dimensional sinusoidal shaped structures but the methodology is rather universal and can be widened towards circular wrinkled structures,[29] herringbone like structures [30,31] or spoke-like radial patterns.[18] A SEM micrograph of the original PDMS structure can be seen in Figure 4.

Cracks occur during the relaxation process due to the brittle nature of the silica-like layer generated by the oxygen plasma. By stretching the PDMS, lateral contraction takes place that cannot be compensated by the hard silica-like layer, when the sample is relaxed after plasma treatment and cracks perpendicular to the wrinkle direction appear.[32] Cracking is one mechanism of the system to release the applied strain.[33,34] In Figure 4, such parallel cracks are imaged and marked by arrows and they serve as a convenient means to discriminate negative from positive replicas. Simultaneously, wrinkles with a dominant single wavelength and amplitudes form to compensate the in-plane strain. The topography can be tuned by changing the applied plasma dose as reported recently.[35,36]

Negative Replication by Hot Embossing

Negative replica of wrinkled PDMS-surfaces in PMMA can be produced using micro thermoforming (hot embossing). Figure 5 shows a typical 3D AFM height image of a replicated structure.

The structured PMMA surface is a negative copy of the wrinkled PDMS surface. In particular, the cracks are filled with PMMA during micro thermoforming and rise up. These structures are of the same height as the pattern height (amplitude of the wrinkled pattern) as shown in Figure 5.

In order to confirm the consistency of the wavelength of the original PDMS master and the structured epoxy resin and PMMA respectively, we applied surface plots averaging the topography along the *x*-axes onto the images taken by AFM and SEM measurements. As SEM measurements provide no height information more detailed AFM images of the PDMS original and the structured PMMA after micro thermoforming were taken as depicted in Figure 6a and b to determine the amplitude of the pattern. From the profile (Figure 6c) it can be seen that the topography of the sinusoidal shaped pattern has been transferred without loss of the sub-micron structure. From these investigations, an average amplitude and wavelength around 32 nm and 280 nm, respectively, was found to be consistent for the original PDMS master and the structured PMMA.

Positive Replication by Molding

While the hot embossing procedure described above is rather simple and can be integrated in modern polymer manufacturing, it is not optimized for creating positive replica of the structures. A direct molding of the PMMA wrinkled surface by epoxy resin is also possible, but the adhesion between the PMMA template and the epoxy replica can cause structural artefacts in the PMMA template. The advantage of the two-step molding process is that the dental wax negative provides a template for replication of large numbers of copies. To achieve this, we used a two step molding process. Poly (vinyl siloxane) dental wax was molded against the original structure. The fine-grained wax is sensitive to adapt the sinusoidal shaped structure with curvatures less than 100 nm, even behind undercuts [24] with high precision and can then be molded again in an additional step using an epoxy resin.

An SEM image of the positive replica of the wrinkled structure can be seen in Figure 7. The topography of the original PDMS master and the structured epoxy resin was determined as described above for the negative PMMA replicas and found to be around 880 nm (wavelength) and 147 nm (amplitude).

Macromol. Chem. Phys. **2010**, *211*, 259–264

Macromolecular Journals

DOI: 10.1002/macp.200900543

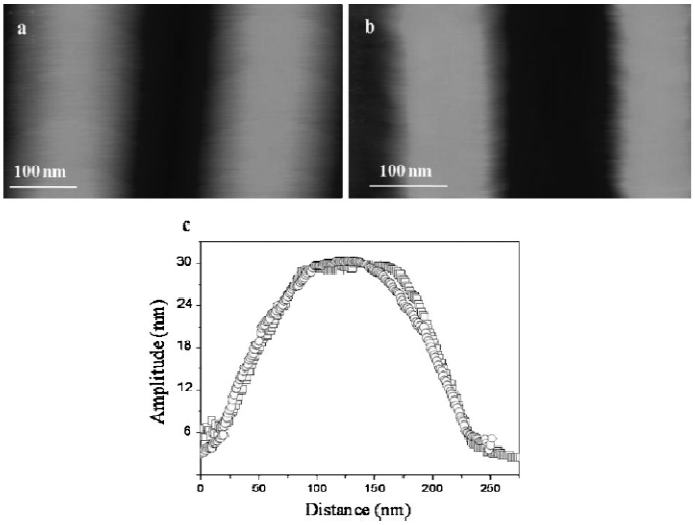

Figure 6. AFM height-images of the used PDMS original (a) and the PMMA duplicate (b). The corresponding profile plot (c) shows, that both wrinkles (PDMS: open circles and PMMA: open squares) feature identical height around 32 nm.

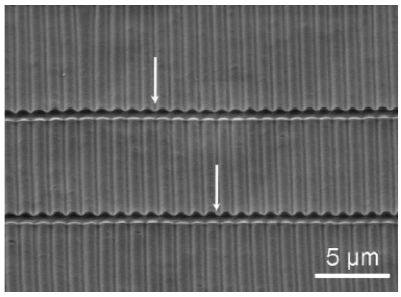

Figure 7. SEM image of replicated epoxy resin surface. Cracks are visible perpendicular to the sinusoidal shaped wrinkles marked with arrows.

In both replication methodologies, the structure of the PDMS original was not destroyed but found to be thermally stable up to 300 °C. Other polymeric materials exhibiting higher T_g, such as high performance polymers[37] could possibly be structured by the micro thermoforming approach.

Micro thermoforming was in our case performed manually, but commercial processes are already known since the second half of the 90s.

Comparing our two approaches we found the molding process using epoxy resin to duplicate the sub-micron pattern in a more detailed manner than the micro thermoforming. Additionally, this method has been proven to be a powerful method to replicate complex natural plant structures like the wax platelets on water repellent leaves of *Iris germanica* as shown in Figure 8.[24]

In contrast, micro thermoforming makes the replication of the structure accessible to a huge variety of different thermoplastic polymers.

Conclusion

In this paper we presented two different approaches to replicate artificial plant sculptures by molding or micro thermoforming of wrinkled surfaces of sub-micron periodicities. The obtained structures are either a duplicate in epoxy resin or a negative of the pattern in PMMA. These two possibilities enable us to make use of different features of the microstructure according to requirements. Especially the arising cracks in the PDMS original structure can be either duplicated or filled by the PMMA polymer. Beside the transfer of the sub-micron structure to technically more reasonable and mechanically stable materials, internal stresses buried in the PDMS original were eliminated. In consequence, stable, sinusoidal shaped nanostructures with improved durability could be fabricated.

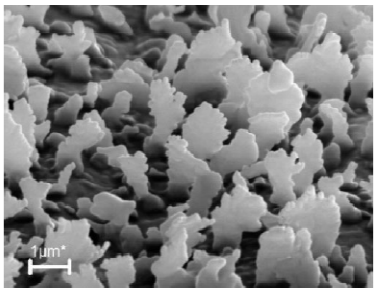

Figure 8. SEM micrograph of a replica of wax platelets made from a water repellent *Iris germanica* leaf (the figure is a part of a SEM micrograph shown in Koch et al. [24]). These structures are a perfect copy in epoxy resin from the living plant leave surface.

The cycle stability of the flexible PDMS original has been proven and can thus be used to fabricate many artificial surface sculptures by an automated process.

Acknowledgements: The authors are grateful for financial support of their work by the *Bundesministerium für Bildung, Forschung und Technologie (BMBF)* and the *German Science Foundation (Deutsche Forschungsgemeinschaft)*, Project 'Biomimetic surfaces' and within SFB 481: 'Complex Macromolecular and Hybrid Systems in Internal and External Fields'.

Received: October 10, 2009; Revised: November 10, 2009; Published online: December 29, 2009; DOI: 10.1002/macp.200900543

Keywords: biomimetic; leaf surfaces; micro molding; microstructure; resins; surface patterning; thermoplastics; wrinkling

[1] P. Roach, N. J. Shirtcliffe, M. I. Newton, *Soft Matter* **2008**, *4*, 224.
[2] S. N. Gorb, *Adv. Insect Physiol.* **2007**, *34*, 81.
[3] R. J. Narayan, P. N. Kumta, C. Sfeir, D. H. Lee, D. Olton, D. W. Choi, *JOM* **2004**, *56*, 38.
[4] A. J. Schulte, K. Koch, M. Spaeth, W. Barthlott, *Acta Biomater.* **2009**, *5*, 1848.
[5] N. Bowden, W. T. S. Huck, K. E. Paul, G. M. Whitesides, *Appl. Phys. Lett.* **1999**, *75*, 2557.
[6] C. Harrison, C. M. Stafford, W. H. Zhang, A. Karim, *Appl. Phys. Lett.* **2004**, *85*, 4016.
[7] C. Bowman, A. C. Newell, *Rev. Mod. Phys.* **1998**, *70*, 289.
[8] J. Genzer, J. Groenewold, *Soft Matter* **2006**, *2*, 310.
[9] W. Barthlott, N. Ehler, *Rasterelektronenmikroskopie der Epidermis-Oberflächen von Spermatophyten*, Franz Steiner Verlag, GmbH Wiesbaden 1977, 19.
[10] K. Koch, B. Bhushan, W. Barthlott, *Soft Matter* **2008**, *4*, 1943.
[11] W. Barthlott, N. Ehler, R. Schill, *Mikroskopie* **1976**, *32*, 35.
[12] L. Feng, Y. A. Zhang, J. M. Xi, Y. Zhu, N. Wang, F. Xia, L. Jiang, *Langmuir* **2008**, *24*, 4114.
[13] N. Bowden, S. Brittain, A. G. Evans, J. W. Hutchinson, G. M. Whitesides, *Nature* **1998**, *393*, 146.
[14] D. B. H. Chua, H. T. Ng, S. F. Y. Li, *Appl. Phys. Lett.* **2000**, *76*, 721.
[15] Z. Y. Huang, W. Hong, Z. Suo, *Phys. Rev. E* **2004**, *70*, 030601.
[16] W. T. S. Huck, N. Bowden, P. Onck, T. Pardoen, J. W. Hutchinson, G. M. Whitesides, *Langmuir* **2000**, *16*, 3497.
[17] D. Y. C. Chan, E. Klaseboer, R. Manica, *Soft Matter* **2009**, *5*, 2858.
[18] J. Y. Chung, A. J. Nolte, C. M. Stafford, *Adv. Mater.* **2009**, *21*, 1358.
[19] J. R. Serrano, Q. Q. Xu, D. G. Cahill, *J. Vac. Sci. Technol. A* **2006**, *24*, 324.
[20] H. Vandeparre, P. Damman, *Phys. Rev. Lett.* **2008**, *101*, 124301.
[21] A. L. Volynskii, S. Bazhenov, O. V. Lebedeva, A. N. Ozerin, N. F. Bakeev, *J. Appl. Polym. Sci.* **1999**, *72*, 1267.
[22] P. J. Yoo, K. Y. Suh, S. Y. Park, H. H. Lee, *Adv. Mater.* **2002**, *14*, 1383.
[23] A. Schweikart, A. Fery, *Microchim. Acta* **2009**, *165*, 249.
[24] K. Koch, A. J. Schulte, A. Fischer, S. N. Gorb, W. Barthlott, *Bioinspir. Biomim.* **2008**, *3*.
[25] M. Heckele, W. K. Schomburg, *J. Micromech. Microeng.* **2004**, *14*, R1.
[26] A. D'Amore, D. Simoneta, W. Kaiser, *Kunststoffe-Plast Europe* **2000**, *90*, 52.
[27] K. Efimenko, W. E. Wallace, J. Genzer, *J. Colloid Interface Sci.* **2002**, *254*, 306.
[28] M. Ouyang, C. Yuan, R. J. Muisener, A. Boulares, J. T. Koberstein, *Chem. Mater.* **2000**, *12*, 1591.
[29] C. Lu, H. Möhwald, A. Fery, *Chem. Mater.* **2008**, *20*, 7052.
[30] X. Chen, J. W. Hutchinson, *J. Appl. Mech. Tech. Phys.* **2004**, *71*, 597.
[31] P. C. Lin, S. Yang, *Appl. Phys. Lett.* **2007**, *90*, 241903.
[32] K. Efimenko, M. Rackaitis, E. Manias, A. Vaziri, L. Mahadevan, J. Genzer, *Nat. Mater.* **2005**, *4*, 293.
[33] S. Frank, U. A. Handge, S. Olliges, R. Spolenak, *Acta Mater.* **2009**, *57*, 1442.
[34] U. A. Handge, *J. Mater. Sci.* **2002**, *37*, 4775.
[35] A. Chiche, C. M. Stafford, J. T. Cabral, *Soft Matter* **2008**, *4*, 2360.
[36] M. Pretzl, A. Schweikart, C. Hanske, A. Chiche, U. Zettl, A. Horn, A. Boker, A. Fery, *Langmuir* **2008**, *24*, 12748.
[37] T. Hoffmann, D. Pospiech, L. Haussler, A. John, P. Friedel, H. Komber, D. Voigt, P. Werner, V. Altstadt, *High Perform. Polym.* **2004**, *16*, 3.

DOI: 10.1002/macp.200900543

Chapter 6 A Lithography-Free Pathway for Chemical Microstructuring of Macromolecules from Aqueous Solution Based on Wrinkling

Langmuir **2008,** *24,* 12748−12753

A Lithography-Free Pathway for Chemical Microstructuring of Macromolecules from Aqueous Solution Based on Wrinkling

Melanie Pretzl,[†] Alexandra Schweikart,[†] Christoph Hanske,[†] Arnaud Chiche,[‡] Ute Zettl,[†] Anne Horn,[†] Alexander Böker,[†] and Andreas Fery*[,†]

Physical Chemistry Department, University of Bayreuth, Universitätsstrasse 30, 95445 Bayreuth, Germany, and DSM - Material Science Centre, Chemelot Gate 2, Urmonderbaan 22, P.O. Box 18, 6160 MD Geleen, The Netherlands

Received July 8, 2008. Revised Manuscript Received August 21, 2008

We report on a novel lithography-free method for obtaining chemical submicron patterns of macromolecules on flat substrates. The approach is an advancement of the well-known microcontact printing scheme: While for classical microcontact printing lithographically produced masters are needed, we show that controlled wrinkling can serve as an alternative pathway to producing such masters. These can even show submicron periodicities. We expect upscaling to larger areas to be considerably simpler than that for existing techniques, as wrinkling results in a macroscopic deformation process that is not limited in terms of substrate size. Using this approach, we demonstrate successful printing of aqueous solutions of polyelectrolytes and proteins. We study the effectiveness of the stamping process and its limits in terms of periodicities and heights of the stamps' topographical features. We find that critical wavelengths are well below 355 nm and critical amplitudes are below 40 nm and clarify the failure mechanism in this regime. This will permit further optimization of the approach in the future.

Patterned deposition of polymers is commonly believed to be one of the key steps in the development of novel functional elements and devices in optics, sensorics, electronics, and biotechnology.[1] The vast majority of approaches toward patterning of functional polymers can be grouped into either top-down (lithography based) or bottom-up approaches. While lithographic approaches offer the advantage that they can be applied to a broad variety of compounds, they are typically difficult to scale up in terms of area, as classical lithography requires exposure of samples through masks and etching steps. "Soft lithography"[2−5] or microcontact printing (μCP) has removed some of these constraints and has consequently developed into a very general approach for deposition of molecularly thin layers of functional molecules. In this technique, a soft elastomeric stamp is used to transfer a solution containing surface active molecules to a flat substrate by mechanical contact. While originally used mainly for low molecular weight molecules forming self-assembled monolayers such as thiols or silanes, the success of this method is meanwhile well established for various macromolecular species including biologically relevant molecules[6−8] and has applications in the field of biosensors, chromatography, diagnostic immunoassays, or cell culturing.[9] While the stamping process in μCP can be carried out under ambient conditions and only requires mechanical contact between the stamp and surface, the bottleneck in cheap upscaling currently is the need of a master that serves as a mold in the fabrication of the elastomeric stamp. This master is so far made by conventional lithographic techniques. In this Letter, we present an alternate approach for the fabrication of microcontact printing stamps that is completely free from lithographic steps. We demonstrate that even submicron periodicity patterns can be stamped using our approach and that it is also compatible with stamping of proteins.[10]

Rather than fabricating the elastomeric stamp by casting the precursor into a lithographic mold and subsequently curing, we form the structured elastomeric surface by controlled wrinkling of the elastomer. The fact that buckling instabilities can result in highly ordered topographically structured surfaces has already been observed by several authors.[11−18] We use a situation in which a hard ultrathin film is formed on a macroscopic elastomeric substrate under strain. Here, wrinkles develop as the elastomer is subsequently relaxed (Figure 1 summarizes the complete stamping process). In our case, the hard film is formed by exposition of a poly(dimethylsiloxane) (PDMS) elastomer to oxygen plasma, which results in the formation of a hard SiO_2-like layer with variable thickness h.[19,20] The thickness h can in this case be fine-tuned by variation of the plasma exposure dose (exposure time in s multiplied by plasma power in kW). Using

* To whom correspondence should be addressed. E-mail: Andreas.Fery@uni-bayreuth.de. Fax: +49(0)921-552059.
† University of Bayreuth.
‡ DSM - Material Science Centre.

(1) Nie, Z. H.; Kumacheva, E. *Nat. Mater.* **2008**, *7*, 277–290.
(2) Kumar, A.; Biebuyck, H. A.; Whitesides, G. M. *Langmuir* **1994**, *10*, 1498–1511.
(3) Kumar, A.; Whitesides, G. M. *Science* **1994**, *263*, 60–62.
(4) Xia, Y. N.; Whitesides, G. M. *Angew. Chem., Int. Ed.* **1998**, *37*, 551–575.
(5) Xia, Y. N.; Whitesides, G. M. *Annu. Rev. Mater. Sci.* **1998**, *28*, 153–184.
(6) Sato, K.; Hibara, A.; Tokeshi, M.; Hisamoto, H.; Kitamori, T. *Adv. Drug Delivery Rev.* **2003**, *55*, 379–391.
(7) Ernst, O.; Lieske, A.; Jager, M.; Lankenau, A.; Duschl, C. *Lab Chip* **2007**, *7*, 1322–1329.
(8) Ruiz, S. A.; Chen, C. S. *Soft Matter* **2007**, *3*, 168–177.
(9) Bernard, A.; Renault, J. P.; Michel, B.; Bosshard, H. R.; Delamarche, E. *Adv. Mater.* **2000**, *12*, 1067–1070.
(10) Dusseiller, M. R.; Smith, M. L.; Vogel, V.; Textor, M. *Biointerphases* **2006**, *1*, 1–4.
(11) Efimenko, K.; Rackaitis, M.; Manias, E.; Vaziri, A.; Mahadevan, L.; Genzer, J. *Nat. Mater.* **2005**, *4*, 293–297.
(12) Groenewold, J. *Phys. A* **2001**, *298*, 32–45.
(13) Lu, C.; Dönch, I.; Nolte, M.; Fery, A. *Chem. Mater.* **2006**, *18*, 6204–6210.
(14) Lu, C. H.; Mohwald, H.; Fery, A. *Soft Matter* **2007**, *3*, 1530–1536.
(15) Huang, J.; Juszkiewicz, M.; de Jeu, W. H.; Cerda, E.; Emrick, T.; Menon, N.; Russell, T. P. *Science* **2007**, *317*, 650–653.
(16) Nolte, A. J.; Cohen, R. E.; Rubner, M. F. *Macromolecules* **2006**, *39*, 4841–4847.
(17) Nolte, A. J.; Rubner, M. F.; Cohen, R. E. *Macromolecules* **2005**, *38*, 5367–5370.
(18) Cerda, E.; Ravi-Chandar, K.; Mahadevan, L. *Nature* **2002**, *419*, 579–580.
(19) Bodo, P.; Sundgren, J. E. *Thin Solid Films* **1986**, *136*, 147–159.
(20) Morra, M.; Occhiello, E.; Marola, R.; Garbassi, F.; Humphrey, P.; Johnson, D. *J. Colloid Interface Sci.* **1990**, *137*, 11–24.

10.1021/la8021694 CCC: $40.75
Published on Web 10/25/2008

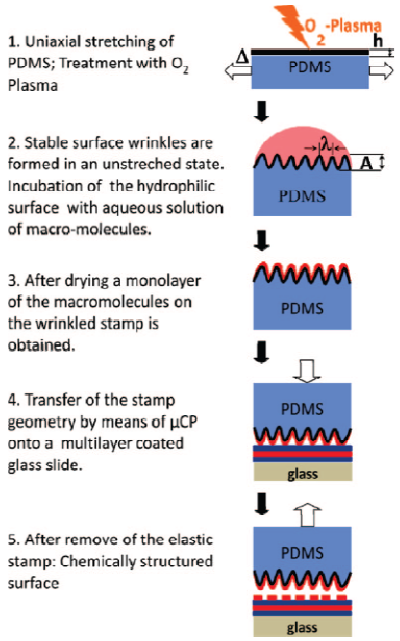

Figure 1. Scheme of wrinkle-assisted microcontact printing. The cross-linked PDMS substrate is stretched uniaxially ($\varepsilon = 20\%$) and exposed to oxygen plasma (1). Stable surface wrinkles with tunable wavelength and amplitude are formed after relaxing. The hydrophilic surface is coated with poly(allylamine hydrochloride) (PAH) or bovine serum albumin (BSA) as ink (2). After drying in a nitrogen gas stream, the monolayer-coated wrinkles (3) are exposed to the substrate which consists of a polyelectrolyte multilayer from poly(diallyldimethyl-ammonium chloride) (PDADMAC) and poly(styrene sulfonate) (PSS) (4). After 15 min, the stamp is removed and a chemical structured surface is obtained (5).

a home-built setup according to Genzer and co-workers,[21] the plasma treatment can be carried out while the PDMS substrate is stretched uniaxially with an external tensile strain ($\varepsilon = 20\%$). In the case of uniaxial strain, one expects that the dominant wrinkle wavelength λ follows an analytical dependency on the substrate's and film's mechanical properties and film thickness:[22,23]

$$\lambda = 2\pi h \left[\frac{(1-\nu_s^2)E_f}{3(1-\nu_f^2)E_s} \right]^{1/3} \quad (1)$$

The wavelength depends in this situation on the thickness h of the hard SiO_2-like film tuned by the plasma exposure dose, its Young's modulus $E_f = 70$ GPa, the Poisson ratio $\nu_f = 0.17$, and the properties of the elastic PDMS substrate (Young's modulus $E_s = 7.1$ MPa and the Poisson ratio of cured network $\nu_s = 0.5$).[19,20] We have first investigated the dependency between the plasma exposure dose and topographic features (A and λ) of the stamps and measured the surface topography using scanning force microscopy. Figure 2A displays the linear dependency of the periodicity and amplitude of the wrinkles on the plasma exposure

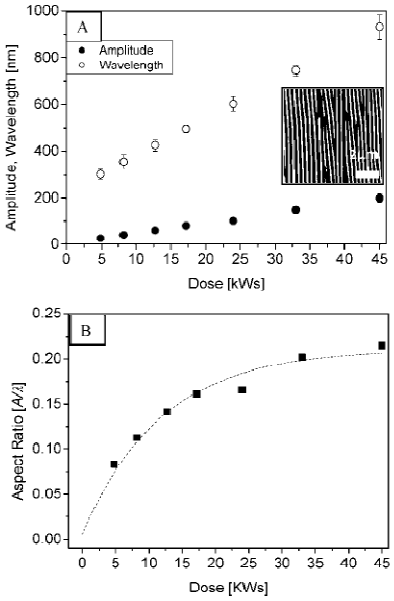

Figure 2. (A) Mechanical wrinkling of a stiff skin on soft PDMS substrate. The wavelength λ of the wrinkles, as measured by scanning force microscopy, increases linearly with oxygen plasma exposure dose. (B) For a constant strain $\varepsilon = 20\%$, the aspect ratio A/λ increases with increasing plasma dose until a plateau is reached. For doses greater than 17.2 kWs the aspect ratio is independent from the applied plasma dose and tends to a constant value of 0.2.

dose in the case explained above. The inset in Figure 2A shows a typical result of a topographical measurement of the wrinkled PDMS stamp. The strain of the substrates was kept constant at $\varepsilon = 20\%$ as well as the plasma power at 0.1 kW. We find that, for plasma doses between 4.8 and 45 kWs, wrinkle periodicities between 302 ± 20 and 931 ± 53 nm develop, while the amplitude varies between 25 ± 2 and 200 ± 19 nm. Thus, periodicities which require advanced lithography techniques such as e-beam lithography[24] are within reach. This linear dependency of the wavelength on exposure time in the observed regime below 1 μm points toward a linear increase of the properties of the SiO_2-like layer with this quantity (increase of either thickness or Young's modulus that makes the SiO_2-like layer harder to bend).[25]

Earlier theoretical considerations of Mahadevan and Cerda predicted that, in such a deformation situation, the amplitude A is expected to depend on the strain ε and wavelength λ via

$$\left(1 + \frac{A^2}{\lambda^2}\right)^{1/2} - 1 \sim \varepsilon \quad (2)$$

and thus, the amplitude of wrinkles should scale as $A \sim \lambda\varepsilon^{1/2}$.[26] Figure 2B shows that the aspect ratio A/λ depends also on the applied plasma dose. For doses between 4.8 and 17.2 kWs we observed increasing aspect ratios, while for doses higher than 17.2 kWs a plateau is reached. In this plateau range the aspect ratio tends to a value of 0.2 and is well described by eq 2. Our results indicate that the aspect ratio is dependent on the plasma

(21) Genzer, J.; Fischer, D. A.; Efimenko, K. *Adv. Mater.* **2003**, *15*, 1545.
(22) Bowden, N.; Huck, W. T. S.; Paul, K. E.; Whitesides, G. M. *Appl. Phys. Lett.* **1999**, *75*, 2557–2559.
(23) Chung, J. Y.; Youngblood, J. P.; Stafford, C. M. *Soft Matter* **2007**, *3*, 1163–1169.
(24) Pompe, T.; Fery, A.; Herminghaus, S.; Kriele, A.; Lorenz, H.; Kotthaus, J. P. *Langmuir* **1999**, *15*, 2398–2401.
(25) Lin, P. C.; Yang, S. *Appl. Phys. Lett.* **2007**, *90*, 241903.
(26) Cerda, E.; Mahadevan, L. *Phys. Rev. Lett.* **2003**, *90*, 074302.

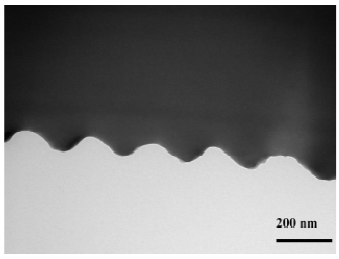

Figure 3. TEM micrograph showing a cross section of an epoxy replica of the PDMS wrinkles ($\lambda = 275 \pm 43$ nm and $A = 63 \pm 6.7$ nm).

dose for values smaller than 17.2 kWs and is more and more independent for doses above 17.2 kWs. For this reason we used the plasma dose as parameter to control quantitatively the wavelength and amplitude of the PDMS stamp over the complete range of plasma doses displayed in Figure 2A.

While we have limited ourselves here to one particular deformation condition (uniaxial strain) for the sake of simplicity and since this is the most widely used case, we would like to stress that other deformation conditions such as multiaxial strain or shear can be employed and will give rise to more complex patterns as reviewed recently.[27] As well, it is worthwhile mentioning that while the substrates used here are only of a few cm^2 in dimensions, the wrinkle process is a result of macroscopic deformation. Thus, upscaling to substrates of much larger sizes should be simple.

To support the results we obtained from scanning force microscopy, we used transmission electron microscopy (TEM) as a further characterization technique. To ensure that the amplitude and the wavelength of the wrinkles were not deformed during the cutting process (microtome), we reproduced the structure with an epoxy resin replica. The sinusoidal topography of the wrinkles can be seen very nicely in the cross section in Figure 3.

In the second step, we carried out μCP of macromolecules using the wrinkle stamp, as indicated in Figure 1. In order to visualize the stamped areas in a simple way, we used fluorescently labeled macromolecules, namely, rhodamine labeled poly(allylamine hydrochloride) (PAH-Rho), in the stamping process. As substrates, we used glass slides coated with a polyelectrolyte multilayer (PEM) consisting of poly(ethylene imine) (PEI), poly(diallyldimethylammonium chloride) (PDADMAC), and poly(styrene sulfonate) (PSS), $PEI(PSS/PDADMAC)_5PSS$, terminated in a negatively charged PSS layer. The stamping conditions were as usual for polymer-on-polymer stamping (POPS)[28,29] with a contact time of 15 min (more details can be found in the Experimental Section). After the stamping process, we obtain a pattern with alternating regions of different charge density; these substrates were characterized using both fluorescence microscopy and scanning force microscopy. Figure 4 shows typical results for both techniques: The fluorescence micrograph (Figure 4A) indicates areas of homogeneous fluorescence intensity which are many tens of micrometers in lateral dimension. On a larger scale, the line defects are visible. These defects are due to cracks of the SiO_2-like layer that formed during the relaxation process. Since SiO_2 is rather brittle, it can crack as the strain is

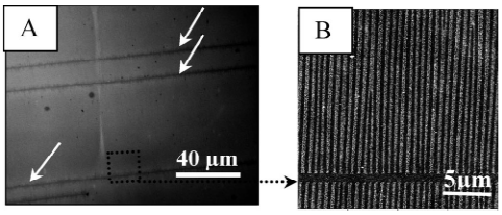

Figure 4. (A) Fluorescence micrograph indicating the homogeneous transfer of the stamped material over a large area as well as the typical surface defects (marked with arrows) arising from the relaxation process of PDMS wrinkles. (B) Corresponding AFM height image (zoom into black square depicted in the fluorescence image) of the chemically patterned surface. The height of the printed PAH-Rho pattern is about 6 nm and highly regular.

released because of lateral elongation of the rubber (PDMS). The cracks appear parallel to the applied external tensile strain.[30] Still, the typical separation (micrometers) of the cracks is 1 order of magnitude larger than the periodicity of the wrinkles (hundreds of nm), and the area occupied by the cracks as compared to the stamped region is negligible. The defects in the printed pattern are visible in both fluorescence microscopy and scanning force microscopy (Figure 4). Fluorescence microscopy gives an overview over larger areas, while atomic force microscopy (AFM) lets us determine the typical width of the cracks. In addition, fluorescence microscopy shows that the typical amount of transferred material is homogeneous over large areas, as differences in coverage would show up as variations in the fluorescence intensity. However, the resolution of fluorescence microscopy is not sufficient to resolve whether the pattern transfer has been successful, as the periodicities are submicron and thus beyond the Rayleigh criterion. Figure 4B displays a scanning force microscopy image that is taken in an arbitrarily selected part of the surface displayed in Figure 4A, as indicated by the square. The AFM image reveals that the surface that appears homogeneous in fluorescence is indeed structured with a submicron periodicity, thus confirming the successful stamping process.

As explained above, both the amplitude and periodicity of the topographical structures can be varied using controlled wrinkling. For both quantities, one expects limits below which stamping fails. In order to determine this lower limit of the stamp geometry, we carried out stamping of identical 0.0193 M solutions of rhodamine labeled poly(allylamine hydrochloride) using stamps of variable amplitudes A and wavelengths λ. Figure 5 displays AFM height images of the stamped structures where a striped pattern can be seen, that is typical for polymer structures in the submicron regime.[31,32] The geometry of the wrinkled PDMS stamps was determined using AFM (Table 1). Our results clearly indicate that the critical conditions are reached for amplitudes below 40 nm and wavelengths below 335 nm (aspect ratio A/λ below 0.11), displayed in Figure 5B. With a further decrease in amplitude and in its proportional wavelength ($A \sim \lambda\varepsilon^{1/2}$), the printed structures start to broaden and converge as indicated in Figure 5A. For this stamp geometry ($\lambda = 302$ nm and $A = 25$ nm), the transfer of the pattern starts to fail.

To further quantify this result, we averaged the height profile over all cross sections perpendicular to the printed pattern. In

(27) Genzer, J.; Groenewold, J. *Soft Matter* **2006**, *2*, 310–323.
(28) Clark, S. L.; Montague, M.; Hammond, P. T. *Supramol. Sci.* **1997**, *4*, 141–146.
(29) Hammond, P. T.; Whitesides, G. M. *Macromolecules* **1995**, *28*, 7569–7571.
(30) Volynskii, A. L.; Bazhenov, S.; Lebedeva, O. V.; Bakeev, N. F. *J. Mater. Sci.* **2000**, *35*, 547–554.
(31) Nolte, M.; Fery, A. *Langmuir* **2004**, *20*, 2995–2998.
(32) Kern, W.; Puotinen, D. A. *RCA Rev.* **1970**, *31*, 187.

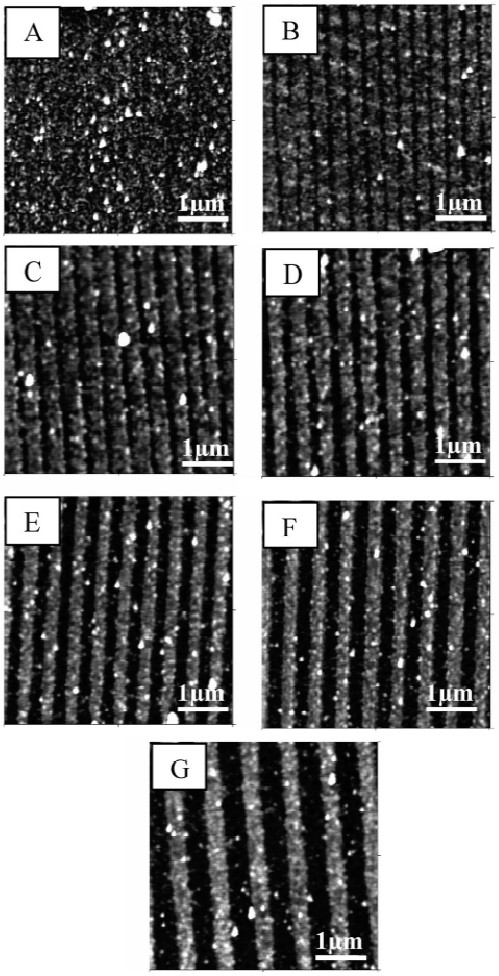

Figure 5. AFM height images (5 μm × 5 μm) of PAH-Rho as ink on substrates coated with a polyelectrolyte multilayer (PEI[PSS/PDADMAC]$_4$PSS). The amplitudes and wavelengths of the used PDMS stamps are increasing from A to G (A_A = 25 nm, λ_A = 302 nm; A_B = 40 nm, λ_B = 355 nm; A_C = 60 nm, λ_C = 426 nm; A_D = 80 nm, λ_D = 496 nm; A_E = 100 nm, λ_E = 602 nm; A_F = 150 nm, λ_F = 743 nm; A_G = 200 nm, λ_G = 931 nm). For sample B, it can be clearly seen that the transfer of the pattern starts to fail; the pattern broadens and converges for amplitudes below 40 nm and wavelengths below 355 nm.

Figure 6A we show an example for a height profile of the printed pattern, extracted from the corresponding AFM height image Figure 5D. The profile is an average over all 512 cross sections perpendicular to the printed pattern. To calculate the mean height of the printed pattern, we used the average peak−valley distances of the height profiles. The results of all prints are summarized in Figure 6B and indicate that the mean height of the printed pattern depends on the PDMS stamps geometry. The plot clearly shows that a constant value for the mean height of 6−7 nm (Figure 6B) is reached for stamp amplitudes greater than 80 nm corresponding to wavelengths greater than 426 nm. For amplitudes smaller than 40 nm and wavelength below 355 nm, the mean

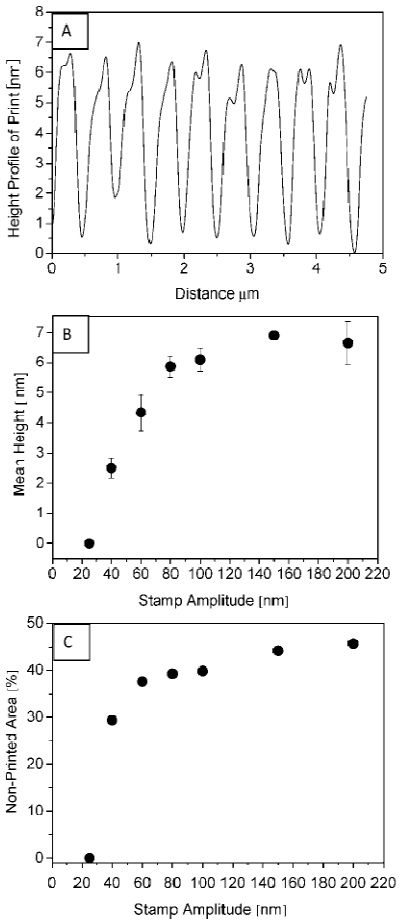

Figure 6. (A) Height profile of printed pattern corresponding to the AFM height image Figure 5D was obtained as average from all 512 cross sections perpendicular to the printed pattern (stamp geometry A_D; 80 nm; λ_D; 496 nm). (B) Plot of mean height of each sample against stamp amplitude clearly shows that a constant value is reached for stamp amplitudes above 80 nm and above a corresponding stamp wavelength of 496 nm. (C) Decrease of the nonprinted areas as percentage of the template (25 μm^2) with decreasing stamp amplitude. Below a stamp amplitude of 60 nm and corresponding wavelength of 426 nm the end of the linear regime is reached and the nonprinted areas vanish to 0% for sample A (A_A, 25 nm; λ_A, 302 nm).

Table 1. Geometry of the Wrinkled PDMS Stamps

sample	A	B	C	D	E	F	G
dose [kWs]	4.8	8.2	12.7	17.2	24	33	45
A [nm]	25	40	60	80	100	150	200
λ [nm]	302	355	426	496	602	743	931
A/λ	0.08	0.11	0.14	0.16	0.17	0.20	0.21

height drops to zero, indicating again the disappearance of the printed features.

The reason for this disappearance of the features can be explained by taking the ratio of printed areas (areas, where ink is transferred by the stamp) and nonprinted areas on the substrate into account. To quantify the nonprinted areas on the substrate, we measured histograms of the AFM images shown in Figure

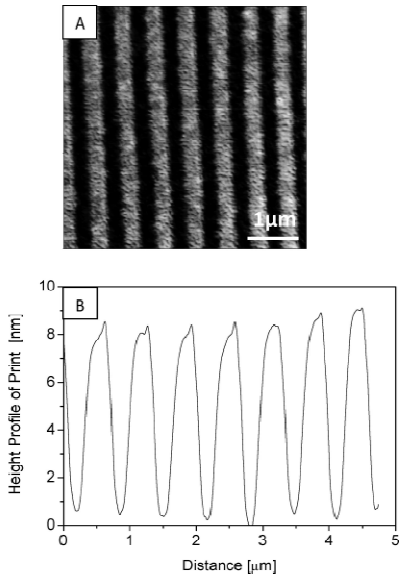

Figure 7. (A) AFM (5 μm × 5 μm) height image of printed BSA on a PEI activated glass surface. (B) Height profile of the printed BSA structures averaged perpendicular to the obtained pattern over all cross sections is found to be about 8 nm.

5, delivering the ratio between printed and nonprinted areas. Figure 6C depicts the nonprinted areas in percent on substrates exhibiting a surface area of 25 μm^2. The size of the nonprinted area decreases with decreasing amplitude and wavelength of the PDMS stamp and drops to 0% for sample A (λ = 302 nm and A = 25 nm). The peaks on the structured stamp approach each other, and the height diminishes. Thus, more peaks contact the template, and with decreasing amplitude and wavelength ink is transferred from the peaks as well as from the valleys of the stamp. The nonprinted areas vanish below wavelengths of 355 nm and amplitudes of 40 nm (end of the linear regime in Figure 6C), which marks the lower limit of our application. It should be marked that thus nonprinted areas can be much smaller than the actual λ of the stamp can be created.

One of the advantages of using plasma oxidation to create a hard top layer is that, at the same time, the originally hydrophobic PDMS surface is rendered hydrophilic. This allows using aqueous solutions as ink for the stamping process and makes the structuring approach suitable for stamping of proteins or other biologically relevant materials. To explore to what extent proteins can be stamped using our approach, we have switched from artificial polyelectrolytes to bovine serum albumin (BSA) as a model protein system. Following the same approach as that for the artificial system, we have used fluorescently labeled BSA in the stamping process and characterized the stamped surfaces using fluorescence microscopy and scanning force microscopy. In order to promote adhesion of BSA, the glass substrates that were used for stamping were precoated with a layer of poly(ethylene imine) (PEI). Figure 7A displays a typical AFM image of the stamped structure as obtained for stamping of BSA. The typical PDMS stamps were oxidized for 360 s using oxygen plasma and exhibited an amplitude of 160 nm and a wavelength of 780 nm (aspect ratio = 0.21). Figure 7B displays the corresponding (averaged) cross sections which show that, for the stamping conditions (as detailed in the Experimental Section), a BSA layer of 8 nm thickness was transferred. This demonstrates that the process can indeed be applied to protein stamping.

In conclusion, we have introduced a novel approach for submicron structuring of polyelectrolytes (including proteins) that builds up on microcontact printing (μCP). While in classical μCP elastomeric stamps are made by casting precursor solution into molds that have to be manufactured using lithographic methods, we demonstrate that for stripe patterns molding is not necessary. Rather, stamps can be made in a one step-process by plasma exposure of strained PDMS, which results in surface topography due to a wrinkling instability. These wrinkled surfaces can serve as stamps for the transfer of ultrathin layers to surfaces. We demonstrate that we can tailor the wavelength and amplitude of the surface topography by adjusting the plasma exposure time, and we find that both parameters follow theoretical predictions. In contrast to lithographic methods, we expect that upscaling of the areas that are structured is greatly simplified, since the wrinkling instability is a result of macroscopic deformations rather than local manipulation. While we have limited ourselves to line patterns (as a commonly used motive in surface patterning), other geometries are well-known to be achievable using the wrinkling approach. We investigated in detail the dependency of the transfer process on the amplitude and wavelength of the wrinkled stamp and identified a critical wavelength of 355 nm and critical amplitude of 40 nm (critical aspect ratio (A/λ) of 0.11) below which structuring fails. For stamp geometries above a wavelength of 496 nm and amplitudes above 80 nm, we found the printed structures to be constant at a height of 6−7 nm. Still, patterns with submicron periodicity can be routinely achieved. In an attempt to generalize our approach and to exploit the fact that the wrinkled surfaces are hydrophilic and thus compatible with stamping of molecules from aqueous solution, we demonstrate that bovine serum albumin can also be used in our stamping process. Thus, our approach will simplify the patterned deposition of not only artificial macromolecules but also proteins and could therefore have an impact on biotechnological applications.

Experimental Section

Fabrication of PDMS Stamps. The PDMS elastomer was prepared by mixing Sylgard 184 (purchased from Dow Corning) with a 10:1 ratio by mass of prepolymer to curing agent. The mixture was stirred and filled in a carefully cleaned, plain Petri dish. After 24 h at RT and baking at 60 °C for 2 h, the cross-linked PDMS was cut into 30 mm × 6 mm stripes. These were stretched uniaxially in a customer-made apparatus to a strain of 20% of their length. The stretched substrates were oxidized between 45 and 400 s in oxygen plasma at 0.2 mbar using a plasma etcher operating at 0.1 kW (flecto10, Plasma Technology, Germany). After cooling, the samples were relaxed with a strain releasing rate of 33 μm/s. The hydrophilic stamps were used directly after plasma treatment.

Film Buildup. Glass slides were cleaned using RCA.[33] For the buildup of polyelectrolyte multilayers on the glass slides, we used the spray coating method (spray bottles "air boy" Carl Roth GmbH, Germany) according to refs 14 and 33. The film consisted of a PEI(PSS/PDADMAC)$_5$PSS multilayer. PEI: poly(ethylene imine), M_W = 25 000 g/mol, 0.0232 M; PSS: poly(sodium-4-styrene sulfonate), M_W = 70 000 g/mol, 0.001 M, 0.5 M NaCl; PDADMAC: poly(diallyldimethylammonium chloride), M_W = 100 000−200 000 g/mol, 0.001 M, 0.5 M NaCl. All chemicals were purchased from Sigma Aldrich (Germany) and were used after filtration of the aqueous solutions.

Contact Printing of PAH-Rho. As ink, rhodamine-labeled poly(allylamine hydrochloride) (PAH-Rho, M_W = 70 000 g/mol,

(33) Izquierdo, A.; Ono, S. S.; Voegel, J. C.; Schaaff, P.; Decher, G. *Langmuir* **2005**, *21*, 7558–7567.

0.0193 M, 0.5 M NaCl, degree of labeling: 1 Rho/670 PAH-Mon) was purchased from Capsulution NanoScience AG, Germany. The incubation time of the PDMS stamp with the ink was 15 min. The PDMS stamp was then rinsed with Millipore water and completely dried under N_2 stream. Afterward, the stamp was brought into contact (without pressing) with an activated glass slide for 15 min. The samples were afterward monitored using fluorescence microscopy and AFM without any further treatment.

Contact Printing of BSA. Fluorescein-labeled bovine serum albumin (BSA-FITC) was purchased from Sigma-Aldrich (M_W = 66 400 g/mol, 1.506×10^{-5} M, degree of labeling: 2.5 mol fluorescein/mol BSA) and dissolved in 0.1 M phosphate buffer. The coating and printing procedure for BSA on polyelectrolyte multilayers was similar to that for PAH-Rho. The samples were afterward monitored using fluorescence microscopy and AFM.

Fluorescence Images. Fluorescence microscopy measurements were carried out on a Zeiss Axiovert 200 microscope (Zeiss, Germany). The light source was a Hg vapor lamp. The excitation and the emission were filtered between 515 and 565 nm, and 450 and 490 nm, respectively. A Zeiss AxiocamHR high-resolution monochromatic camera was used.

AFM Images. AFM images were obtained using a commercial atomic force microscope (NanoWizard, JPK Instruments, Germany) operating in the tapping mode. Silicon cantilevers with a force constant of typically 46 N/m (MikroMash, Estonia NC-W, typical frequency of 300 kHz) were utilized. Also, a Multimode atomic force microscope (Veeco Instruments Inc.) operating in the tapping mode with silicone cantilevers (force constant = 34.0 58.7 N/m) and a typical frequency of 330 kHz was used.

Acknowledgment. This work was supported by the Systems for ImaGing and Healthcare Technologies project (SIGHT) and the German Research Council, Collaborative Research Center SFB 481 TP A14 on Complex Macromolecular and Hybrid Systems in Internal and External Fields. A.H. and A.B. acknowledge support by the Lichtenberg-Program of the Volkswagen Stiftung. We thank C. M. Stafford for the fruitful discussions.

LA8021694

Chapter 7 Nanoparticle Assembly by Confinement in Wrinkles: Experiments and Simulations

COMMUNICATION www.rsc.org/softmatter | Soft Matter

Nanoparticle assembly by confinement in wrinkles: experiment and simulations

Alexandra Schweikart,[a] Andrea Fortini,[b] Alexander Wittemann,[a] Matthias Schmidt[bc] and Andreas Fery*[a]

Received 29th July 2010, Accepted 22nd September 2010
DOI: 10.1039/c0sm00744g

We created hierarchically ordered structures of nanoparticles on smooth planar hydrophilic substrates by drying colloidal dispersions in confinement under macroscopic stamps with microscopically wrinkled surfaces. Experiments were carried out with model nanoparticle suspensions that possess high colloidal stability and monodispersity. The structures ranged from single parallel lines of particles to arrays of dense prismatic ridges. The type of observed structure could be controlled by the particle concentration in the initial dispersion. Confinement between two crossed stamps led to interconnected meshes of particles. The precise morphology could be predicted in all cases by Monte Carlo computer simulations of confined hard spheres. Our findings open up possibilities for versatile nanoparticle assembly on surfaces.

Ordered arrays of nanoparticles form excellent candidates for components of future optical, electronic and magnetic devices,[1,2] for creating biomimetic surfaces,[3] and for exploiting their plasmonic properties.[4,5] Control of the precise placement of the particles on a solid surface is a prerequisite for the technological use of the unique, size-specific properties of the nanoparticles.

Primary strategies for controlling the spatial arrangement of much larger, micron-sized colloids include the deposition of particle monolayers on chemically or topographically structured substrates,[6–9] epitaxial growth[10,11] and confinement.[12,13] Structures with periodicities comparable to the wavelength of visible light are interesting as these enable one to make use of their optical band structure. In particular, linear assemblies, such as particle wires,[14,15] possess high potential for photonic applications. Nevertheless, both structuring on the smaller (nano) scale, as well as obtaining macroscopic coverage of the substrate is desirable in attempting to bridge all length-scales. Both physical[6,9] and chemical[7,8] properties of surfaces can be used in order to create templates for the adsorption of particles. Topographic templates can be produced using photolithographic[1,2] and soft lithographic[16–18] techniques or, alternatively, by controlled wrinkling.[19,20] Wrinkles with well-defined wavelength form if an elastomeric substrate that is coated with a thin, hard layer is exposed to a lateral compressive strain.[21] Significant benefits of this approach are its low cost and the simplicity of scaling up the size of the structured substrate to macroscopic dimensions.

[a]*Physikalische Chemie I & II, Universität Bayreuth, Universitätsstraße 30, D-95440 Bayreuth, Germany. E-mail: andreas.fery@uni-bayreuth.de*
[b]*Theoretische Physik II, Physikalisches Institut, Universität Bayreuth, Universitätsstraße 30, D-95440 Bayreuth, Germany*
[c]*H. H. Wills Physics Laboratory, University of Bristol, Royal Fort, Tyndall Avenue, Bristol, BS8 1TL, United Kingdom*

Here we study model dispersions of nanoparticles (radius 55 nm) under confinement by wrinkled surfaces. Confinement is known to have a dramatic effect on the type of stable crystalline structures. High density states of micron-sized particles between two smooth parallel plates display a rich variety of crystals, as found in experiments[12,13] and in simulations of hard sphere model systems.[22,23] Even stronger spatial confinement is provided by cylindrical pores[24–26] or inside grooves on a planar substrate,[20] where wire-like colloidal arrangements are formed. Here we find that highly ordered one-dimensional structures of nanoparticles form upon drying of aqueous colloidal dispersions when these are confined between a smooth planar hydrophilic surface and a wrinkled elastomer. The wavelength of the wrinkles determines the spacing between the (parallel) linear colloidal assemblies. The particle density of the structures can be tuned by varying the particle volume fraction in the initial suspension. A rich variety of ordered structures is observed. We demonstrate that this originates primarily from packing effects of the confined particles by comparing to results from our Monte Carlo computer simulations of the hard sphere model.

The particles were synthesized by emulsion polymerization of styrene with acrylic acid (5.2 mol% relative to styrene) as the comonomer, sodium dodecylsulfate as the emulsifier, and potassium persulfate as the initiator. They possessed an average radius $R = 55$ nm (as determined from dynamic light scattering) with narrow size distribution. The polydispersity index, given as the weight-average diameter divided by the number-average diameter, was only 1.02 (determined by analytic disk centrifugation). The zeta potential of the particles was -55 ± 5 mV, indicating a well-stabilized suspension.

Wrinkled substrates (stamps) were created by stretching a silicon elastomer, poly(dimethyl siloxane) (PDMS), exposing it to an oxygen plasma in order to convert the surface to silica, and subsequent relaxation of the specimen. Stable wrinkles with one dominant wavelength were obtained. Both the wavelength and the amplitude could be controlled *via* the plasma dose applied.[27] In detail, the PDMS elastomer was prepared by mixing Sylgard 184 (purchased from Dow Corning, USA) with a 10 : 1 ratio by mass of pre-polymer to curing agent. The mixture was stirred and filled in a carefully cleaned, plain glass dish. After 24 h at room temperature and baking at 60 °C for 2 h, the cross linked PDMS was cut into 30 × 6 mm stripes. These were stretched in a customer-made apparatus to a linear strain of $\varepsilon = 0.25$. The stretched substrates were exposed for 500 s to an oxygen-plasma at 0.2 mbar using a plasma etcher operating at 0.1 kW (flecto10, Plasma Technology, Germany) to convert the topmost layer to silica. After cooling, the strain was slowly released from the specimen and stable uniform wrinkles were obtained. The glass slides were cleaned using standard RCA-1, performed with a 1 : 1 : 5 solution of $NH_4OH + H_2O_2 + H_2O$ at 75 °C.

This treatment results in the formation of a thin hydrophilic silicon dioxide layer on the glass surface providing appropriate wettability.

After rinsing in water and blow-drying with nitrogen, a drop of nanoparticle suspension (10 μl) was placed onto a glass slide. Immediately after spreading, the wrinkled substrate was placed onto the drop without applying external pressure. After 12 h of drying, the wrinkled PDMS stamp was removed carefully and both surfaces were dried under vacuum. When illuminated with white light, iridescent colors could be observed on the elastomer stamp. This effect is due to interference of the incident light with the periodic substrate. Very similar interference colors[28] appeared also on the glass substrate. Fig. 1a and b display photographs of this effect for two different samples. Scanning electron microscopy (SEM) revealed that the smooth glass substrate was macroscopically covered by parallel prismatic ridges of nanoparticles, see Fig. 1c. These structures remained stable after thorough rinsing in water. The ridges possessed the same spacing as the wrinkles on the stamp, which explains the origin of the iridescent colors. However, besides this structuring on the micron scale, the nanoparticles ordered in crystal-like structures on the particle scale, see the inset of Fig. 1c. SEM images of the wrinkled PDMS stamps showed no appearance of nanoparticles, indicating that the particles stick to the glass surface. Consistent with this, the aqueous suspension of nanoparticles preferentially wets the clean glass surface. It is known that appropriate wetting of wrinkles is essential for colloidal assembly, as shown in ref. 29 and 30.

In order to test whether confinement plays a dominant role in the structuring process, we wish to compare to high-density equilibrium states of a minimal model. We consider hard spheres of radius R confined between one smooth planar hard wall at $z = 0$ and one sinusoidal hard wall at $z = L_z + a[\sin(2\pi x/\lambda)-1]$. Here z is the coordinate across the slit, L_z is a measure of the distance of the two walls, a is the amplitude of the sinusoidal corrugation, λ is its wavelength, and x is the lateral coordinate perpendicular to the wrinkles. Any direct interactions between the two walls are omitted. Fig. 2 displays an illustration of the model, for which we carried out Monte Carlo computer simulations for a wide range of different values of particle concentrations and for several values of the amplitude a. The wavelength was fixed to the experimentally determined value of $\lambda = 17.38R$. Periodic boundary conditions were applied in the x and y (along the wrinkles) directions, and the box size in the x-direction was chosen as 4λ. We kept the number of particles $N = 800$ constant, as well as the lateral area $L_x \times L_y = const.$ The length L_z was allowed to fluctuate, such that the z component of the pressure, P_z, was kept constant at a finite, but large value of $P_z = 1.875k_BT/R^3$, where k_B is the Boltzmann constant and T is absolute temperature. The simulations were started at a value of $L_z \gg a$, such that the system was in a disordered, low-density fluid state. Then the system was equilibrated for a total of 10^7 MC steps per particle. The linear density $\rho = RN\lambda/(L_yL_x)$ was kept constant throughout the compression procedure. Clearly, all effects due to capillary bridges of the drying solvent as well as due to charges and van der Waals forces are neglected.

The type of experimentally observed particle assemblage could be controlled by varying the volume fraction ϕ of particles in the initial dispersion. Fig. 3 (left column) displays a sequence of SEM pictures of structures for a stamp with $\lambda = 956$ nm. The difference between minima and maxima (*i.e.* twice the value of the amplitude) of the substrate was 148 nm, as obtained by analyzing atomic force microscopy (AFM) height profiles. At low density ($\phi = 0.002$, Fig. 3a) we found parallel lines of particles in single file. For increasing density ($\phi = 0.004$, Fig. 3b) we found two lines of particles, a pyramidal prism with two particles in the base and one on top ($\phi = 0.007$, Fig. 3c), a pyramidal prism with three particles in the base and two on top (Fig. 3d), and finally a larger pyramidal prism with four particles in the base ($\phi = 0.014$, Fig. 3e). The only prismatic structures reported in the literature are, to the best of our knowledge, those of much larger, micron-sized, spheres.[15] By counting particles we obtained the linear density ρ of particles per unit length (taken as the particle radius R) of the particle arrays. We compare to simulation results that we have obtained for the same values of ρ. The resulting hard sphere structures are shown from the top (middle column in Fig. 3) and along the channels (right column). All structures agree very well with their experimental counterparts, even reproducing accurately the types of defects that occur. We expect the defects to originate (i) partly from the kinetics of the compression process, but

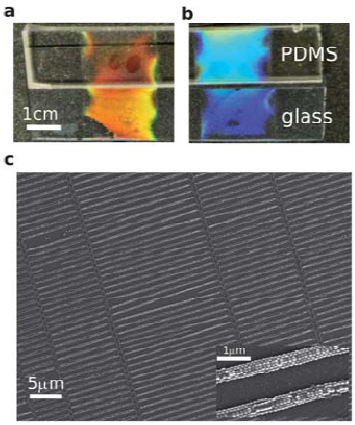

Fig. 1 Digital camera pictures (a and b) of wrinkled PDMS stamps (above) and decorated glass substrates (below). The different iridescent colors in (a) and (b) stem from periodically structured features of the surface with different wavelengths (956 nm and 765 nm, respectively). The SEM image in (c) shows prismatic structures assembled on the glass substrate, with spacing between prisms that matches the wavelength of the wrinkles. Perpendicular bridges of particles originate from cracks on the stamp on a larger length scale. The inset shows a magnified section of the main picture.

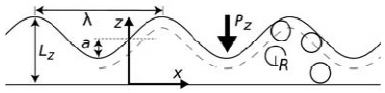

Fig. 2 An illustration of the theoretical model of hard spheres with radius R confined between a (lower) smooth hard wall and an (upper) hard wall with sinusoidal shape of wavelength λ and amplitude a. The (maximal) distance between both walls is denoted by L_z. The pressure P_z acts on the top wall; the lower wall is kept fixed. The dashed lines indicate the depletion zones that are inaccessible to the particle centers, due to interactions of the particles with the walls. z is the coordinate across the slit; x and y are the lateral coordinates; y (not shown) is perpendicular to the image plane.

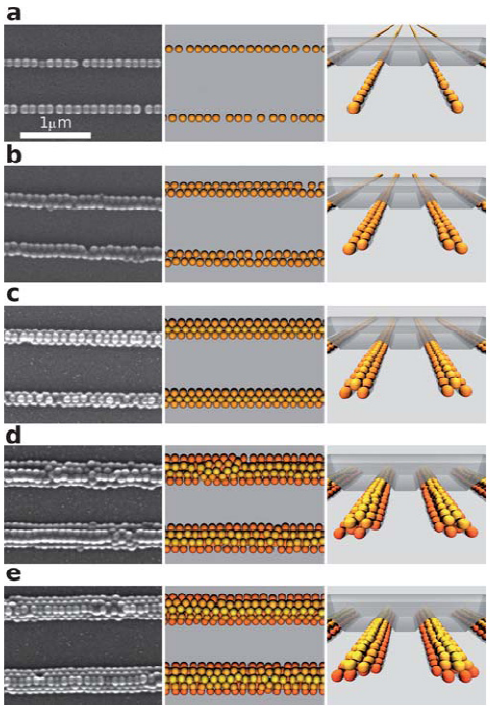

Fig. 3 Sequence of structures found experimentally with SEM (left column) and in simulations, shown from the top (middle column) and along the channels (right column). The concentration increases from (a) to (e), leading to structures that range from single-file wires to prisms with triangular cross section. The transparent grey shape represents the sinusoidal wall and is shown only partially for clarity.

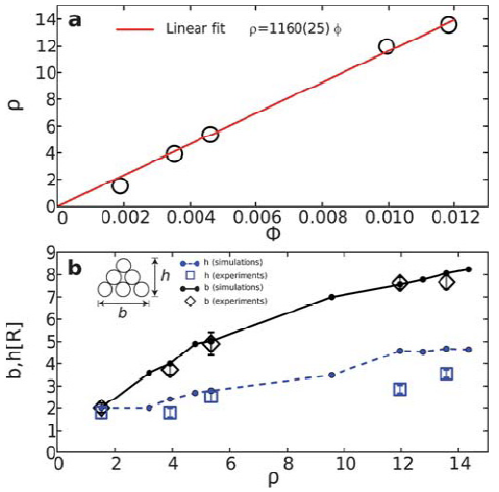

Fig. 4 (a) Experimental results (symbols) for the dependence of the linear density ρ of assembled particles on the initial volume fraction ϕ of particles in the dispersion. The line is a linear fit to the data. (b) Variation of the geometry of the colloidal structures with their density ρ. Shown are the height h and base b of the prism structures (see inset for a cross section) in units of particle radius R as obtained in simulations (filled symbols joined by lines to guide the eye) and AFM measurements (open symbols with error bars).

also (ii) from intrinsic disorder that is of thermal, entropic origin. The structures with more than two lines of particles possess the same triangular, prism-like cross section as were found experimentally. The simulation results were obtained by choosing the amplitude $a = 3.6R$, significantly larger than half of the experimental value for the free stamp, 74 nm $= 1.35R$. However, in our model we allow for overlap of both walls, such that $L_z < 2a$. We take the resulting pore shapes (*cf.* right column of Fig. 3) as a simple model for the real channels, which we expect to be influenced by deformation of the wrinkles when in contact with a hard substrate.[27]

Remarkably, the experimentally observed variation of ρ with the initial packing fraction ϕ is nearly linear, see Fig. 4a. This allows to tune ρ, and hence the type of ordered structure, accurately by simple variation of ϕ. We measured the relevant geometrical dimensions of the structures, namely the base b and height h (see the inset of Fig. 4 b for an illustration). Values for b were determined by image analysis of SEM pictures; those for h were determined from height profiles measured by AFM. In the computer simulations the results for b and h were obtained by measuring density profiles in the direction perpendicular to the prisms and in the z-direction, respectively. We find quantitative agreement of the results from the two approaches for the variation of b with ρ, see Fig. 4b. The values for the height h as a function of ρ as determined in experiment are consistently smaller than those found in simulations. Part of this deviation could be due to shrinking of the particles upon drying; the particle diameter as measured by AFM is 10% smaller than the hydrodynamic value. Nevertheless, the general agreement is very satisfactory, in particular given the simplicity of the model.

Even more complex structures were formed, when the suspension was confined between *two* wrinkled stamps, with channel directions at a right angle. The resulting grid-like structure of particles possessed completely different, strongly interconnected topology, see Fig. 5a for an SEM image. Correspondingly, in simulations we confined the hard sphere model between two sinusoidal walls with crossed orientations, and hence replaced the lower (smooth) wall by $z = a[\sin(2\pi y/\lambda) + 1]$ with $L_x = L_y = 4\lambda$ and chose $N = 2780$ in order to match roughly the experimental situation. The resulting structure, see Fig. 5b, reproduced very well the features of the experimental result. Moreover, crossing two stamps at an angle of 45° creates a chiral grid with ellipsoidal holes (Fig. 5c) that could again be reproduced in simulation (Fig. 5d) by counter-rotating two sinusoidal walls (initially with wave vector in the x-direction) by ±22.5° and choosing $L_x = 2\lambda/\sin(22.5°)$, $L_y = 2\lambda/\cos(22.5°)$ and $N = 1537$.

We proposed a versatile method for hierarchical nanoparticle structuring that allows for easy control of spacing and density of particle arrays on a smooth planar hydrophilic substrate. Macroscopic coverage can be obtained. As the assembly is driven by packing effects, the details of the chemistry play only a minor role: we could obtain very similar structuring using, instead of polystyrene, other organic and gold nanoparticles. Linear

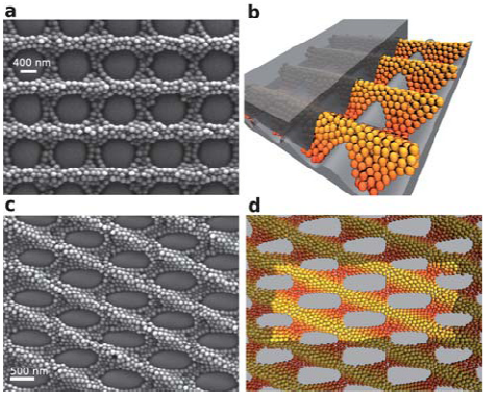

Fig. 5 (a) SEM image of a dried colloidal suspension that was confined between two crossed wrinkled stamps. (b) Perspective view of a simulation configuration of hard spheres confined between two sinusoidal walls with crossed orientations. Half of the upper wall is cut away for clarity. (c) As in (a) but for two stamps that were crossed by an angle of 45°. (d) Top view of the simulation configuration corresponding to (c). Particles that belong to periodic images are shaded grey. Note the chiral nature of the structure in (c) and (d); this cannot be transformed by rotations and translations only into its chiral partner with crossing angle of −45°).

structures of the latter are well suited for optical applications, such as surface enhanced Raman spectroscopy.[31] It would be interesting to investigate the interplay of drying and adhesion under confinement, and the role of dispersion forces in the assembly process in future work. We leave a systematic investigation of the dependence of the type of colloidal structures on the wavelength and amplitude of the wrinkles on the stamp to future work.

Acknowledgements

We thank Moritz Tebbe for helpful assistance in carrying out some of the experimental work and Mark Dennis and Paddy Royall for useful comments on the manuscript. A.S. thanks the German Science Foundation (DFG) for support within the SFB481. A.Fo. and M.S. thank the DFG for support *via* SFB840/A3, A.Fe. and A.W. *via* SFB840/B5.

References

1 Z. Sun and B. Yang, *Nanoscale Res. Lett.*, 2006, **1**, 46–56.
2 S. J. Koh, *Nanoscale Res. Lett.*, 2007, **2**, 519–545.
3 S. Mitragotri and J. Lahann, *Nat. Mater.*, 2008, **8**, 15–23.
4 J. A. Schuller, E. S. Barnard, W. Cai, Y. C. Jun, J. S. White and M. L. Brongersma, *Nat. Mater.*, 2010, **9**, 193–204.
5 H. A. Atwater and A. Polman, *Nat. Mater.*, 2010, **9**, 205–213.
6 Y. Xia, Y. Yin, Y. Lu and J. McLellan, *Adv. Funct. Mater.*, 2003, **13**, 907–918.
7 K. Chen, X. Jiang, L. Kimerling and P. T. Hammond, *Langmuir*, 2000, **16**, 7825–7834.
8 P. Maury, M. Escalante, D. Reinhoudt and J. Huskens, *Adv. Mater.*, 2005, **17**, 2718–2723.
9 J. Aizenberg, P. Braun and P. Wiltzius, *Phys. Rev. Lett.*, 2000, **84**, 2997–3000.
10 A. van Blaaderen, R. Ruel and P. Wiltzius, *Nature*, 1997, **385**, 321–324.
11 J. Hoogenboom, C. Retif, E. de Bres, M. de Boer, A. van Langen-Suurling, J. Romijn and A. van Blaaderen, *Nano Lett.*, 2004, **4**, 205–208.
12 Pa. Pieranski, L. Strzelecki and B. Pansu, *Phys. Rev. Lett.*, 1983, **50**, 900–903.
13 S. Neser, C. Bechinger, T. Palberg and P. Leiderer, *Phys. Rev. Lett.*, 1997, **79**, 2348–2351.
14 Y. Masuda, T. Itoh, M. Itoh and K. Koumoto, *Langmuir*, 2004, **20**, 5588–5592.
15 T. Mitsui, Y. Wakayama, T. Onodera, Y. Takaya and H. Oikawa, *Nano Lett.*, 2008, **8**, 853–858.
16 Y. Xia and G. Whitesides, *Annu. Rev. Mater. Sci.*, 1998, **28**, 153–184.
17 E. Kim, Y. Xia and G. M. Whitesides, *Adv. Mater.*, 1996, **8**, 245–247.
18 A. Hung and S. Stupp, *Nano Lett.*, 2007, **7**, 1165–1171.
19 N. Bowden, S. Brittain, A. G. Evans, J. W. Hutchinson and G. M. Whitesides, *Nature*, 1998, **393**, 146–149.
20 C. Lu, H. Möhwald and A. Fery, *Soft Matter*, 2007, **3**, 1530–1536.
21 J. Genzer and J. Groenewold, *Soft Matter*, 2006, **2**, 310–323.
22 M. Schmidt and H. Löwen, *Phys. Rev. Lett.*, 1996, **76**, 4552–4556.
23 A. Fortini and M. Dijkstra, *J. Phys.: Condens. Matter*, 2006, **18**, L371–L378.
24 G. T. Pickett, M. Gross and H. Okuyama, *Phys. Rev. Lett.*, 2000, **85**, 3652–3655.
25 F. Li, X. Badel, J. Linnros and J. B. Wiley, *J. Am. Chem. Soc.*, 2005, **127**, 3268–3269.
26 M. Tymczenko, L. F. Marsal, T. Trifonov, I. Rodriguez, F. Ramiro-Manzano, J. Pallares, A. Rodriguez, R. Alcubilla and F. Meseguer, *Adv. Mater.*, 2008, **20**, 2315–2318.
27 M. Pretzl, A. Schweikart, C. Hanske, A. Chiche, U. Zettl, A. Horn, A. Böker and A. Fery, *Langmuir*, 2008, **24**, 12748–12753.
28 See, *e.g.*, O. L. J. Pursiainen, J. J. Baumberg, H. Winkler, B. Viel, P. Spahn and T. Ruhl, *Opt. Express*, 2007, **15**, 9553–9561 and references therein.
29 Y. J. Chung, J. P. Youngblood and C. M. Stafford, *Soft Matter*, 2007, **3**, 1163.
30 T. Ohzono, H. Monobe, H. Shiokawa, M. Fujiwara and Y. Shimizu, *Soft Matter*, 2009, **5**, 4658.
31 N. Pazoz-Pérez, W. Ni, A. Schweikart, R. A. Alvarez-Puebla, A. Fery and L. M. Liz-Marzán, *Chem. Sci.*, 2010, **1**, 174–178.

Chapter 8 Highly Uniform SERS Substrates formed by Wrinkle-Confined drying of Gold Colloids

Chemical Science

www.rsc.org/chemicalscience Volume 1 | Number 2 | August 2010 | Pages 141–280

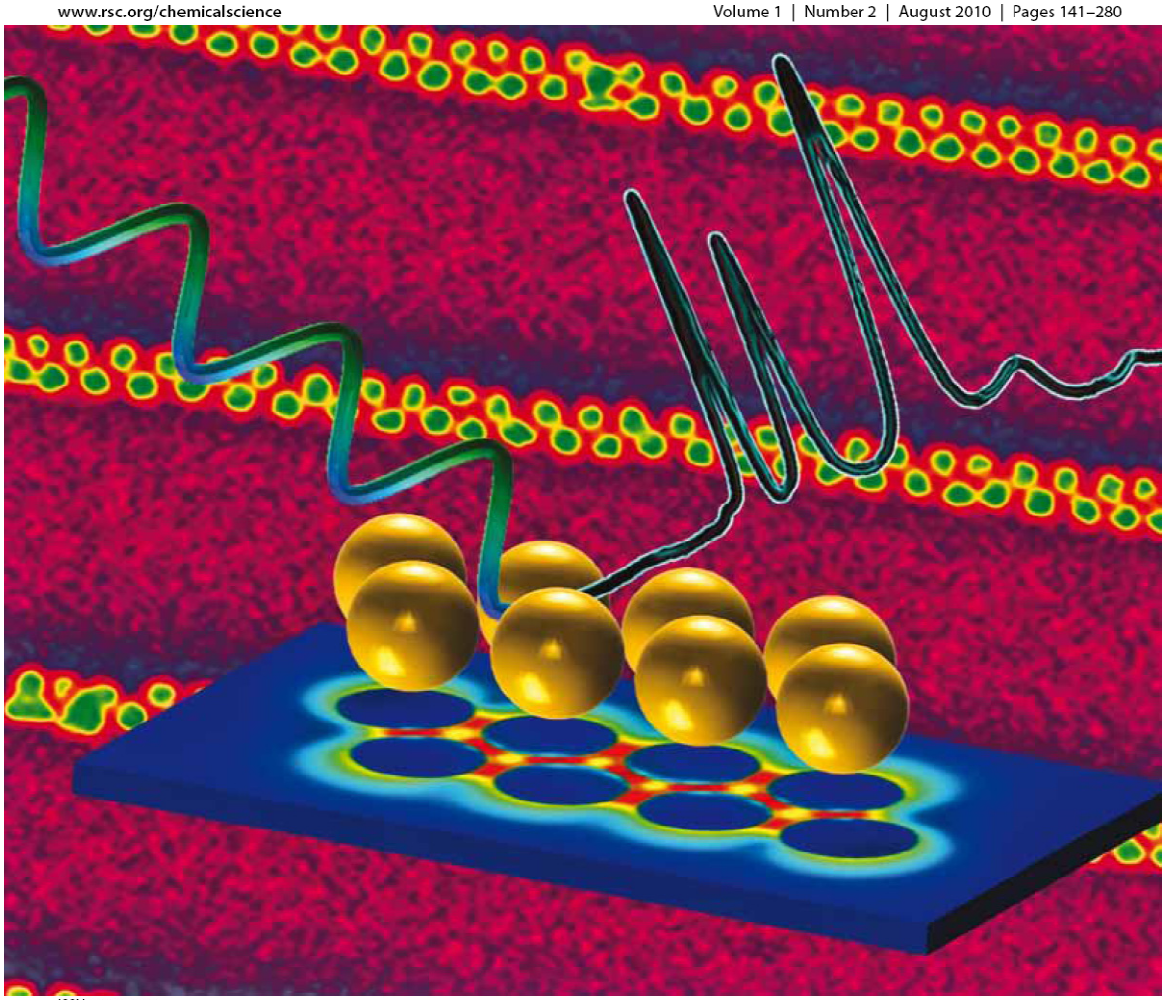

ISSN 2041-6520

RSC Publishing

2041-6520(2010)1:2;1-Z

EDGE ARTICLE www.rsc.org/chemicalscience | Chemical Science

Highly uniform SERS substrates formed by wrinkle-confined drying of gold colloids†

Nicolás Pazos-Pérez,[a] Weihai Ni,[b] Alexandra Schweikart,[a] Ramón A. Alvarez-Puebla,*[b] Andreas Fery*[a] and Luis M. Liz-Marzán*[b]

Received 15th January 2010, Accepted 23rd April 2010
DOI: 10.1039/c0sc00132e

SERS substrates were fabricated through self-assembly of gold nanoparticles upon solution-drying in a periodic confining structure. The technique leads to uniform, parallel linear nanoparticle arrays with the precise arrangement defined through the dimensions of the particles and the grooves, which provide high and uniform SERS enhancement over extended areas.

Despite the extraordinary detection limits provided by surface-enhanced Raman scattering (SERS),[1–5] quantitative applications of this ultrasensitive analytical technique are still restricted by critical limitations, in particular related to the uniformity of the substrates and the corresponding reproducibility in the measurements.[6,7] A wide variety of substrates have been engineered to optimize the necessary metallic nanostructures so that high electromagnetic fields can be obtained as required to enhance the Raman signal.[8–10] Besides the popular gold or silver island films, obtained by physical vapor deposition,[11] a number of other interesting methods such as layer-by-layer (LbL) assembly, electron beam lithography (EBL), nanoimprint lithography (NIL) or nanoparticle self-assembly have been widely reported to provide high enhancing fields which can even lead to single molecule detection.[8–10,12] While the vast majority of these substrates focus on the problem of achieving large SERS enhancements, other requirements such as reproducibility of the signal intensity are seldom addressed. Only a few of these substrates are capable of providing reproducible SERS signal intensities over wide areas, and still offer high enhancement factors (EF) for increased sensitivity. Substrates aimed for ultradetection comprise, in most cases, nanostructured metals with a fractal distribution of so-called hot spots, which are spatial regions where the electromagnetic field is extremely intense due to plasmon coupling between neighboring nanoparticles. On the other hand, when quantitative analysis is the target, random hot spot distribution needs to be avoided through high homogeneity in the morphology (shape and size) of the metallic nanostructures and typically with no interaction (plasmon coupling) between them.[13–15] This restriction is mainly due to the difficulty of preparing substrates through reproducible aggregation so that hot spots could always be created in the same manner. An approach to solve this has been patterning of substrates by EBL.[16] However, while the intensity was indeed very reproducible point to point, it was not competitive with that provided by randomly aggregated films. Other interesting alternatives to control SERS intensity include the use of plasmon standing waves[17] or Wood anomalies in gratings;[18] however, both methods sacrifice intensity in order to achieve reproducibility. Thus, to date, the closest solution to this problem is probably the use of nanosphere lithography coupled to film over nanospheres (NSL-FON), mainly developed by Van Duyne's Group.[19,20] These substrates have been proven to work as quantitative ultrasensitive platforms,[21,22] but are still restricted regarding nanoparticle morphology to the triangles (truncated tetrahedrons) generated in the interstices between the organized polystyrene beads, as well as to the size of such nanostructures, which is in turn determined by the size of the beads. Other promising methods have being reported, such as electrodeposition on template surfaces,[23] or block copolymer micelle nanolithography.[24] Therefore, organization of pre-synthesized nanoparticle colloids using modern lithographic techniques appears as a viable alternative to NSL-FON, if both the size and shape of the particles, as well as their organization on the substrate can be properly controlled. In this context, we introduce in this paper the combination of controlled particle assembly with chemical synthesis of monodisperse gold colloids to fabricate nanostructured substrates with a highly uniform and reproducible distribution of hot spots over large areas.

We have recently demonstrated that wrinkled surfaces are efficient templates toward controlled assembly of particles from solution by either dip coating[25] or spin coating.[26] In this work the assembly process was further simplified by casting a concentrated gold nanoparticle colloid onto the desired surface and confining it by the elastomeric stamp during drying.[27] The assembly of gold nanoparticles using wrinkled polydimethylsiloxane (PDMS) for confining colloidal solutions during drying is sketched in Scheme 1. Wrinkles of different wavelengths (~340 and ~500 nm) and depths (~23 and ~77 nm, respectively), as measured by AFM (see ESI†) were created by plasma-oxidation of stretched PDMS samples and subsequent relaxation.[28,29] Briefly, the PDMS precursor and curing agent were mixed and placed in a flat glass box where they were cured overnight.

[a]*Physical Chemistry Department, University of Bayreuth, Universitätsstrasse 30, 95445 Bayreuth, Germany. E-mail: andreas.fery@uni-bayreuth.de*
[b]*Departamento de Química Física, and Unidad Asociada CSIC-Universidade de Vigo, 36310 Vigo, Spain. E-mail: ramon.alvarez@uvigo.es; lmarzan@uvigo.es; Fax: +34 9868 12556; Tel: +34 9868 12298*

† Electronic supplementary information (ESI) available: Materials and methods; AFM analysis of wrinkled PDMS stamps; TEM images and localized surface plasmon resonances for the gold nanoparticles as prepared; other orientations for the electric field intensity enhancement contours; and, LSPR, SEM and optical and SERS images for a 9 nm gold island film. See DOI: 10.1039/c0sc00132e

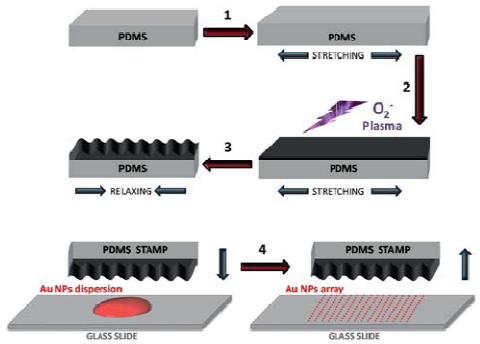

Scheme 1 Preparation of the wrinkled PDMS stamp (1–3) and formation of gold nanoparticle arrays (4). Wrinkling process: A PDMS substrate is uniaxially stretched (1), and then treated with oxygen plasma to cross-link the top layer into a harder, thin SiO_x film (2). The substrate is then relaxed to its original size forming wrinkles on the surface due to the hardness of the silica layer (3). Confining: A gold nanoparticle solution, drop-cast onto a glass slide, is confined with a wrinkled PDMS stamp (4). After solvent evaporation, the stamp is removed yielding a parallel arrangement of gold nanoparticles ordered in linear arrays.

Thereafter, the mixture was heated up in an oven at 60 °C for two hours and then cooled down to room temperature. After cutting the substrate in strips (30 × 8 mm), it was uniaxially stretched to 125% of its original size.[30] Subsequently, the PDMS surface was treated with oxygen plasma to promote the formation of a silica layer.[31] Finally, upon relaxation of the PDMS film to its initial size, wrinkle formation was completed in the outer SiO_x layer of the substrate. Notably, by controlling the duration of the plasma treatment, the width of the generated grooves could be controlled. A critical parameter in this process is the size and shape monodispersity of the particles in the colloid, which can be readily achieved for various morphologies, in particular using controlled seeded growth.[32–35] While other shapes can be used following the same procedure, we have restricted ourselves in this work to gold nanospheres (66 nm diameter), as a proof of concept. Reasons for selecting this size included the effect of nanoparticle volume for the enhancement of the SERS intensity,

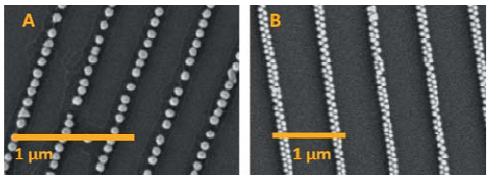

Fig. 1 Scanning electron microscopy (SEM) images of two different stamped films, comprising single-line (A) and double-line (B) arrays of gold nanoparticles, upon confinement of a monodisperse gold colloid with wrinkled stamps of varying dimensions. Wrinkle wavelength and depth were determined by AFM to be 340 and 23 nm in A; 500 and 77 nm in B.

since it has been reported that particles with a larger volume yield higher intensities.[36,37] Additionally, the isotropic nature of the spherical shape allows for a homogeneous distribution of the plasmonic electromagnetic field over their entire volume, in contrast with what has been recently reported about field focalization (*i.e.* nanoantenna effect) in some anisotropic shapes such as triangles, rods or stars.[3,38,39] The latter is a key factor toward reproducibility of the intensity as the homogeneous distribution of the electric field should give rise to homogeneous hot spots regardless of the precise volumes of the particles that are interacting in each particular probe site. Gold nanoparticles were prepared *via* seed mediated growth, in the presence of cetyltrimethylammonium bromide (CTAB), following the method previously reported by Rodriguez-Fernandez *et al.* (see details in the ESI†).[40] This synthesis yields stable aqueous colloids of monodisperse nanoparticles with an average diameter of 66 nm, and a localized surface plasmon resonance (LSPR) band centred at 539 nm. In order to achieve a dense nanoparticle array during the stamping process, gold colloidal dispersions with high particle concentrations are required.[27] Thus, the original colloid was concentrated 50 fold by careful centrifugation, to reach a final concentration in gold of 3.75 mg mL^{-1}. A small volume (10 µL) of the concentrated colloid was cast onto a clean glass surface and stamped for 12 h, leading to evaporation of the solvent and organization of the particles inside the wrinkles. This process was carried out with two different stamps prepared by simply tuning the time of exposure to the oxygen plasma. Fig. 1 shows representative SEM micrographs of the materials obtained upon stamping, showing in both cases a periodic assembly of the nanoparticles into parallel lines. However, while the first one (Fig. 1A) shows a homogeneous pattern of single-particle lines, in the second sample (Fig. 1B), the lines are composed by two alternate rows of particles. This is due to the different size of the grooves, which is a direct consequence of the time of plasma treatment.[29] Detailed SEM analysis indicated that the average interparticle distance is 8 nm for both samples, which is consistent with the values for CTAB stabilized colloids reported in the literature.[41]

Fig. 2 displays a summary of the optical characterization and theoretical modelling for both (single- and double-line) nanoparticle arrays. As expected, the optical properties (determined as scattering intensity from uniform regions using a dark field microspectroscopy setup as described in the ESI†) are affected by the details of the arrangement within each assembly. In both samples, the LSPR was found to be red-shifted with respect to the dilute gold colloid, as a consequence of plasmon coupling due to interactions between the electromagnetic fields of neighbouring particles.[42] Interestingly, there are no significant differences between them, with maxima at 593 and 601 nm for the single-line and double-line arrays, respectively, though the double-line array yields a wider scattering band. Aggregation is well known to promote the formation of hot spots where high electromagnetic fields arise.[2,43,44] For the specific arrangements obtained in this work, it is relatively simple to calculate the respective far field extinction spectra and the corresponding plasmonic near field enhancement at the maximum LSPR scattering wavelength, through modelling by means of the finite-difference time-domain (FDTD) method. For the calculation, two models were constructed in agreement with the experimental dimensions

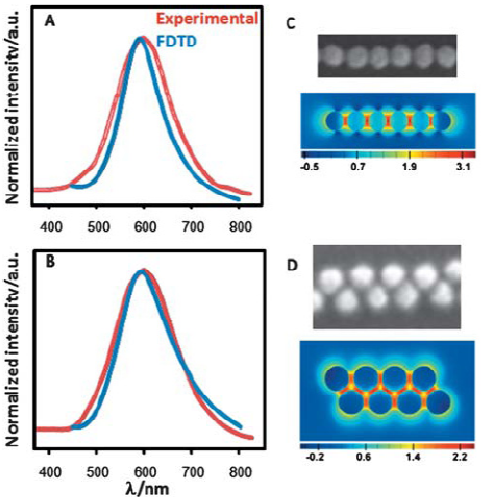

Fig. 2 (A,B) Normalized experimental and calculated localized surface plasmon resonance bands for single-line (A) and double-line (B) stamped films. (C,D) Electric field intensity enhancement contours at a logarithmic scale for a single-line (C) Au nanoparticle array (excitation polarization along the x axis; mesh size 1 nm) and double-line (D) Au nanoparticle array (the profile was averaged over excitation polarizations at 0, 90, −58, and 58 degrees referred to the *x* axis; mesh size is 1.5 nm; contours are plotted in the *xy* plane).

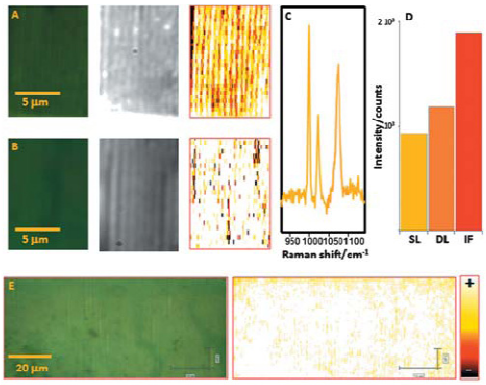

Fig. 3 (A,B) Optical, dark field and SERS images (λ_{ex}: 633 nm; normalized intensity at 1072 cm^{-1}; 8.5 × 12.5 μm^2, step size 200 and 500 nm for *x* and *y*, respectively, with a total of 1062 spectra) for single-line (A) and double-line (B) nanoparticle arrays. (C) Representative SERS spectrum of benzenethiol. (D) Comparison of intensities between single-line (SL) and double-line (DL) nanoparticle arrays and a physically evaporated (IF) 9 nm gold island film; see electronic supplementary information for details.† (E) SERS mapping over a large area of particles arranged in single lines (λ_{ex}: 633 nm; normalized intensity at 1072 cm^{-1}; 105 × 45 μm^2, step size 200 and 500 nm for *x* and *y*, respectively, with a total of 47 250 spectra). Scale bar is the same for all the SERS maps.

determined by SEM. The single-line array was simulated by a linear array of six nanoparticles (66 nm diameter), with an interparticle gap distance of 8 nm (Fig. 2C). The model for the double-line array comprised eight nanoparticles linearly aligned in two alternate rows, with a closest gap distance of 8 nm (Fig. 2D). Both model systems are fully consistent with SEM micrographs and the theoretical LSPR bands are in extremely good agreement with the experimental values (Fig. 2A,B), which strongly supports the validity of the models. Near field enhancement profiles, plotted at their corresponding LSPR maximum wavelengths, reveal that the electromagnetic field within the particle arrays is unevenly distributed, with significant enhancements precisely located at the gaps between nanoparticles, generating strong hot spots, in full agreement with the electromagnetic model in SERS.[45]

On the basis of the registered LSPR bands for the nanostructured substrates, the optical enhancing properties were tested using a laser excitation wavelength of 633 nm, upon exposure of the substrates to benzenethiol (BT) in gas phase. As a control, the same experiment was carried out on a physically evaporated gold island film, which is a conventional SERS substrate. It is important to point out that both dark field optical characterization and SERS mapping were carried out on the same specific areas of each substrate. Fig. 3A,B shows the white light, dark field and SERS images (normalized intensity at 1072 cm^{-1}; Fig. 3C) obtained for the single- and double-line arrays. The first observation is that the SERS spectrum of BT, characterized by the CH bending (1022 cm^{-1}) and the ring breathings (999 and 1072 cm^{-1}), could be readily acquired from all points in the image. Further, in both cases the intensity of the SERS signal was highly uniform, in strong contrast to that obtained for the gold island film (Figure S5†). On the other hand, considering the average intensity (Fig. 3D), the island film was still found to outperform the nanoparticle arrays (almost double intensity). However, it should be taken into account that the sample preparation for SERS measurements (*i.e.* gas adsorption of a thiolated analyte) ensures that the probe creates a perfect Langmuir monolayer on the whole accessible gold surface. Thus, samples with a larger gold content will retain more analyte, with the subsequent increase in the SERS signal. Due to the ordered nature of the linear arrays and the high homogeneity in size and shape of the colloidal sample, it is possible to estimate the number of particles per sampled area. On the basis of the numerical aperture of the objective (0.9), the beam waist of the 100× objective is 430 nm with a 633 nm excitation laser line. Under such conditions and considering that the distance between grooves is 340 and 500 nm for single-line and double-line arrays as experimentally measured with SEM, a maximum of 1 line is probed in each scan. Moreover, the number of particles per sampled area (430 × 430 nm^2) was experimentally counted to be around 6 and 12 for each sample, which is consistent with that theoretically expected (5.8 particles) by assuming a total particle diameter of 74 nm (particle + gap). Unfortunately, this method cannot be applied to the irregular gold film, but for a semiquantitative comparison we can consider that an area of 430 × 430 nm would contain 46

particles of the same size in cubic packing or 50 in hexagonal packing. With those numbers in mind we can carry out a correction of the overall intensity into "intensity per particle", with the following results: 155, 99 and 41 counts for single-line, double-line and island film, respectively. As a consequence, the normalized enhancement by the single-line and double-line arrays is respectively three-fold and two-fold larger than that for an ideal island film. Additionally, this result suggests that the interaction resulting from order within a line is considerably more efficient than that created by the same particles ordered in a plane, in very good agreement with the electric field enhancement values estimated from FDTD. Fig. 2 C and D show that, whereas in both conformations hot spots are created at the gaps between particles, the electromagnetic field generated by the single-line array is up to one order of magnitude larger than that created by the double-line array. This concept becomes particularly important in ultrasensitive analysis since by simply decreasing the amount of nanostructured optical enhancer the detection limit will be increased because the formation of a monolayer will require a lower amount of analyte.[46] Finally, an additional demonstration of the homogenous intensity provided by the substrate was obtained by sampling a large area of the single-line array. The results (Fig. 3E) clearly demonstrate that with this assembly method it is possible to control the organization of the colloidal particles on the substrate, with a consequent control over the formation of hot spots and the resulting SERS intensity, thus paving the road for the large scale development of highly-sensitive quantitative platforms, which have remained elusive so far.

Homogeneously wrinkled stamps can be used to produce linear arrays of gold nanoparticles over large areas by confined drying of nanoparticle solutions. Depending on the dimensions of the grooves, the nanoparticles can be arranged into either single-line or double-line arrays, giving rise to marginally different optical response through plasmon coupling. Characterization of the SERS efficiency demonstrates high and extremely uniform enhancements for both types of assemblies, with higher values for the single-line arrays. This technique may become the method of choice for carrying out quantitative analysis while maintaining low detection limits.

Cristina Fernández-López is acknowledged for synthesizing the gold colloids. R.A.A.-P. acknowledges the RyC program (MEC, Spain). This work has been funded by the Spanish Ministerio de Ciencia e Innovación (Grants MAT2007-62696 and MAT2008-05755), the Xunta de Galicia (PGIDIT06TMT31402PR and 08TMT008314PR), and from the EU (NANODIRECT, grant number CP-FP 213948-2). A.F. and A.S. acknowledge funding from the German science foundation within the collaborative research project SFB 481, TP A14 and A.F. acknowledges funding from the German science foundation within the collaborative research project SFB 840, TP B5.

Notes and references

1 N. P. Pieczonka and R. F. Aroca, *Chem. Soc. Rev.*, 2008, **37**, 946–954.
2 L. Brus, *Acc. Chem. Res.*, 2008, **41**, 1742–1749.
3 L. Rodríguez-Lorenzo, R. A. Alvarez-Puebla, I. Pastoriza-Santos, S. Mazzucco, O. Stephan, M. Kociak, L. M. Liz-Marzán and F. J. García de Abajo, *J. Am. Chem. Soc.*, 2009, **131**, 4616–4618.
4 J. Kneipp, H. Kneipp and K. Kneipp, *Chem. Soc. Rev.*, 2008, **37**, 1052–1060.
5 X. M. Qian and S. M. Nie, *Chem. Soc. Rev.*, 2008, **37**, 912–920.
6 N. P. Pieczonka and R. F. Aroca, *ChemPhysChem*, 2005, **6**, 2473–2484.
7 R. A. Alvarez-Puebla and L. M. Liz-Marzán, *Small*, 2010, **6**, 604–610.
8 M. J. Banholzer, J. E. Millstone, L. Qin and C. A. Mirkin, *Chem. Soc. Rev.*, 2008, **37**, 885–897.
9 R. A. Tripp, R. A. Dluhy and Y. Zhao, *Nano Today*, 2008, **3**, 31–37.
10 S. Abalde-Cela, S. Ho, B. Rodriguez-Gonzalez, M. A. Correa-Duarte, R. A. Alvarez-Puebla, L. M. Liz-Marzan and N. A. Kotov, *Angew. Chem., Int. Ed.*, 2009, **48**, 5326–5329.
11 V. L. Schlegel and T. M. Cotton, *Anal. Chem.*, 1991, **63**, 241–247.
12 H. Ko, S. Singamaneni and V. V. Tsukruk, *Small*, 2008, **4**, 1576–1599.
13 R. A. Alvarez-Puebla, R. Contreras-Cáceres, I. Pastoriza-Santos, J. Pérez-Juste and L. M. Liz-Marzán, *Angew. Chem., Int. Ed.*, 2009, **48**, 138–143.
14 R. M. Jarvis, H. E. Johnson, E. Olembe, A. Panneerselvam, M. A. Malik, M. Afzaal, P. O'Brien and R. Goodacre, *Analyst*, 2008, **133**, 1449–1452.
15 S. E. Bell and N. M. Sirimuthu, *Chem. Soc. Rev.*, 2008, **37**, 1012–1024.
16 M. A. De Jesús, K. S. Giesfeldt, J. M. Oran, N. A. Abu-Hatab, N. V. Lavrik and M. J. Sepaniak, *Appl. Spectrosc.*, 2005, **59**, 1501–1508.
17 M. Abdelsalam, P. N. Bartlett, A. E. Russell, J. J. Baumberg, E. J. Calvo, N. G. Tognalli and A. Fainstein, *Langmuir*, 2008, **24**, 7018–7023.
18 A. G. Brolo, E. Arctander, R. Gordon, B. Leathem and K. L. Kavanagh, *Nano Lett.*, 2004, **4**, 2015–2018.
19 J. P. Camden, J. A. Dieringer, J. Zhao and R. P. Van Duyne, *Acc. Chem. Res.*, 2008, **41**, 1653–1661.
20 Y. Fang, N. H. Seong and D. D. Dlott, *Science*, 2008, **321**, 388–392.
21 K. E. Shafer-Peltier, C. L. Haynes, M. R. Glucksberg and R. P. Van Duyne, *J. Am. Chem. Soc.*, 2003, **125**, 588–593.
22 K. B. Biggs, J. P. Camden, J. N. Anker and R. P. Van Duyne, *J. Phys. Chem. A*, 2009, **113**, 4581–4586.
23 S. Mahajan, J. J. Baumberg, A. E. Russell and P. N. Bartlett, *Phys. Chem. Chem. Phys.*, 2007, **9**, 6016–6020.
24 A. Sánchez-Iglesias, P. Aldeanueva-Potel, W. Ni, J. Pérez-Juste, I. Pastoriza-Santos, R. A. Alvarez-Puebla, B. N. Mbenkum and L. M. Liz-Marzán, *Nano Today*, 2010, **5**, 21–27.
25 C. Lu, H. Möhwald and A. Fery, *Soft Matter*, 2007, **3**, 1530–1536.
26 A. Horn, H. G. Schoberth, S. Hiltl, A. Chiche, Q. Wang, A. Schweikart, A. Fery and A. Böker, *Faraday Discuss.*, 2009, **143**, 143–150.
27 A. Schweikart, A. Fortini, A. Wittemann, M. Schmidt and A. Fery, Manuscript submitted.
28 J. Genzer and J. Groenewold, *Soft Matter*, 2006, **2**, 310–323.
29 A. Schweikart and A. Fery, *Microchim. Acta*, 2009, **165**, 249–263.
30 J. Genzer and K. Efimenko, *Science*, 2000, **290**, 2130–2133.
31 D. B. H. Chua, H. T. Ng and S. F. Y. Li, *Appl. Phys. Lett.*, 2000, **76**, 721–723.
32 L. M. Liz-Marzán, *Langmuir*, 2006, **22**, 32–41.
33 M. Grzelczak, J. Perez-Juste, P. Mulvaney and L. M. Liz-Marzan, *Chem. Soc. Rev.*, 2008, **37**, 1783–1791.
34 I. Pastoriza-Santos and L. M. Liz-Marzán, *Adv. Funct. Mater.*, 2009, **19**, 679–688.
35 C. J. Murphy, T. K. Sau, A. M. Gole, C. J. Orendorff, J. Gao, L. Gou, S. E. Hunyadi and T. Li, *J. Phys. Chem. B*, 2005, **109**, 13857–13870.
36 P. N. Njoki, I.-I. S. Lim, D. Mott, H.-Y. Park, B. Khan, S. Mishra, R. Sujakumar, J. Luo and C.-J. Zhong, *J. Phys. Chem. C*, 2007, **111**, 14664–14669.
37 J. Rodríguez-Fernández, A. M. Funston, J. Pérez-Juste, R. A. Alvarez-Puebla, L. M. Liz-Marzán and P. Mulvaney, *Phys. Chem. Chem. Phys.*, 2009, **11**, 5909–5914.
38 J. Nelayah, M. Kociak, O. Stéphan, F. J. García de Abajo, M. Tencé, L. Henrard, D. Taverna, I. Pastoriza-Santos, L. M. Liz-Marzán and C. Colliex, *Nat. Phys.*, 2007, **3**, 348–353.

39 G. W. Bryant, F. J. García de Abajo and J. Aizpurua, *Nano Lett.*, 2008, **8**, 631–636.
40 J. Rodríguez-Fernández, J. Pérez-Juste, F. J. García de Abajo and L. M. Liz-Marzán, *Langmuir*, 2006, **22**, 7007–7010.
41 H. Wang, J. Kundu and N. J. Halas, *Angew. Chem., Int. Ed.*, 2007, **46**, 9040–9044.
42 T. Ung, L. M. Liz-Marzán and P. Mulvaney, *J. Phys. Chem. B*, 2001, **105**, 3441–3452.
43 G. Braun, I. Pavel, A. R. Morrill, D. S. Seferos, G. C. Bazan, N. O. Reich and M. Moskovits, *J. Am. Chem. Soc.*, 2007, **129**, 7760–7761.
44 J. M. Baik, S. J. Lee and M. Moskovits, *Nano Lett.*, 2009, **9**, 672–676.
45 M. Moskovits, *J. Raman Spectrosc.*, 2005, **36**, 485–496.
46 M. Spuch-Calvar, L. Rodríguez-Lorenzo, M. P. Morales, R. A. Alvarez-Puebla and L. M. Liz-Marzán, *J. Phys. Chem. C*, 2009, **113**, 3373–3377.

Electronic Supplementary Information for:

Highly uniform SERS substrates formed by wrinkle-confined drying of gold colloids

Nicolás Pazos-Pérez[a], Weihai Ni[b], Alexandra Schweikart[a], Ramón A. Alvarez-Puebla[b,*], Andreas Fery[a,*], and Luis M. Liz-Marzán[b,*]

[a] *Physical Chemistry Department, University of Bayreuth, Universitätsstrasse 30, 95445 Bayreuth, Germany. E-mail: andreas.fery@uni-bayreuth.de*

[b] *Departamento de Química Física, and Unidad Asociada CSIC-Universidade de Vigo, 36310 Vigo, Spain. Fax: 34 9818 12556; Tel: 34 986 12298; E-mail: ramon.alvarez@uvigo.es; lmarzan@uvigo.es*

Materials and Methods:

Chemicals: Hydrogen tetrachloroaurate(III) trihydrate ($HAuCl_4 \cdot 3H_2O$), ascorbic acid, cetyltrimethylammonium bromide (CTAB), trisodium citrate dihydrate, isopropanol and benzenethiol (BT) were supplied by Sigma-Aldrich. Polydimethylsiloxane (PDMS) Sylgard (184) silicon elastomer, curing agent and precursor were purchased from Dow Corning, USA. Mucasol was obtained from Merz. All reactants were used without further purification. Milli-Q water (18 MΩ cm^{-1}) was used in all aqueous solutions. The reaction vessels were washed with aqua regia prior to all the experiments. All chemicals were analytical grade or better.

Preparation of monodisperse gold nanoparticles: Spherical gold nanoparticles were prepared via a seed mediated approach following the method previously reported by Rodriguez-Fernandez et al..[1] Briefly, a seed solution of ~12 nm particles ([Au]=0.5 mM) was prepared by citrate reduction and then diluted to double the initial volume with a 0.03 M CTAB solution. Overgrowth of the seeds, was carried out by adding (at 35 °C) the seed solution to a growth solution containing $HAuCl_4$ (2.5 10^{-4} M), CTAB (0.015 M), and ascorbic acid (5 10^{-4} M). The mean diameter of the obtained gold particles was 66 nm (Figure S1). Prior to the stamping process, the particle concentration was increased as follows: 30 mL of the obtained gold dispersion was centrifuged (7000 rpm, 10 min) and redispersed in a total volume of 0.6 mL, with a final gold concentration of 3.75 mg/mL.

Fabrication of PDMS stamps:[2-3] The PDMS elastomer was prepared by mixing Sylgard 184 with a 10:1 ratio by mass of prepolymer to curing agent. The mixture was stirred and filled in a carefully cleaned, flat Petri dish. After 24 h at room temperature and baking at 60 °C for 2 h, the cross-linked PDMS was cut into 30 mm × 8 mm stripes. These were stretched uniaxially in a custom-made apparatus to a strain of 125% of their intial length.[4] The stretched substrates were oxidized during either 50 or 150 s in oxygen plasma at 0.2 mbar using a plasma etcher operating at 0.1 kW (flecto10, Plasma Technology, Germany).[5] After cooling, the samples were relaxed with a strain releasing rate of 240 µm/s. The hydrophilic stamps were used directly after plasma treatment.

Nanoparticle stamping: The glass slides used as substrates for the stamping process were previously cleaned with a strong surfactant (mucasol), milli-Q water, and isopropanol. The glass slides were then sonicated for 15 min in a mixture of milli-Q water (75%) and isopropanol (25%), followed by the well known Standard Clean 1 (SC-1 or RCA 1)[6], comprising the treatment with a mixture of H_2O, H_2O_2, NH_4OH (5:1:1) at 70 °C during 15 min and extensive washing with milli-Q water. The gold colloid (10µL, 3.75 mg/mL) was drop-cast onto a glass slide and allowed to spread. Thereafter, the wrinkled PDMS stamp was placed on the substrate and left undisturbed for 12 h.

Characterization: UV-VIS spectroscopy (PerkinElmer, Lambda 19), transmission and scanning electron microscopy (TEM, LEO 922 EFTEM operating at 200 kV and LEO 1530 FE-SEM, Zeiss, respectively), were applied to characterize the optical response, structure, and size of the nanoparticles and their arrays. AFM images were obtained using a commercial atomic force microscope (Dimension™ 3100M equiped with a Nanoscope IIIm controler, Veeco Instruments Inc., USA) operating in the tapping mode. Silicon cantilevers with a force constant of typically 35-47.2 N/m (OMCL-AC160TS, Olympus, Japan, typical frequency of 303 kHz) were utilized.

Dark-field imaging and spectroscopy on individual Au nanoparticle arrays were carried out on an inverted optical microscope (ZEISS Observer A1) equipped with an Acton SpectraPro 2150i monochromator and a Princeton Instruments Pixis 1024 charge-coupled device (CCD), which was thermoelectrically cooled to -50 °C. Au nanoparticle arrays on glass slides were illuminated by white light from a 100 W tungsten lamp through a dark-field condenser (NA = 0.8). The scattered light was collected with a 40× objective (LD Plan-NEOFLUAR, NA = 0.6) and reflected to the entrance slit of the monochromator for imaging and spectroscopy. Scattering spectra from individual Au nanoparticle arrays were corrected by subtracting background spectra taken from the adjacent regions containing no Au nanoparticles.

Near field calculation: Localized surface plasmon scattering spectra and electric field enhancement at the Au nanoparticle arrays were calculated using the finite-difference time-domain (FDTD) method. In the calculation, the arrays were modelled as spherical Au nanoparticles linearly aligned on a glass substrate. Based on the SEM experimental measurements, the diameter of the nanoparticles was set at 66 nm. The dielectric function used for Au in the calculation was described by the free electron Drude model with parameters

set to match the standard experimental values.[7] The refractive index of the surrounding media, air, and the glass substrate were taken to be 1.0 and 1.52, respectively. The incident light was parallel along the normal to the substrate. The mesh size used in the calculation was set to 1 nm for single-line arrays and 1.5 nm for double-line arrays, respectively. The gap distance between neighbouring nanoparticles within each array was 8 nm, corresponding to that determined from SEM images.

SERS characterization: Benzenethiol was adsorbed, from the gas phase, on the whole surface of the metallic samples by casting a drop of BT (0.1 M in ethanol) in a Petri dish where the substrate was also contained. SERS spectra were collected in backscattering geometry with a Renishaw Invia Reflex system equipped with 2D-CCD detector and a Leica confocal microscope. The spectrograph uses a high resolution grating (1800 g cm^{-1}) with additional bandpass filter optics. Excitation of the sample was carried out with a 633 nm He-Ne laser line, with acquisition times of 200 ms and power at the sample of about 1mW, using the Renishaw's StreamLine accesory. The laser was focused onto the sample with a 100× objective. For comparison, gold island films of 9 nm mass thickness were prepared in a Balzers BSV 080 glow discharge evaporation unit. The metal films were deposited on preheated (200 °C) glass slides (Corning). During film deposition, the background pressure was maintained at 10^{-6} Torr, and the deposition rate (0.5 Å s^{-1}) was monitored using an XTC Inficon quartz crystal oscillator.

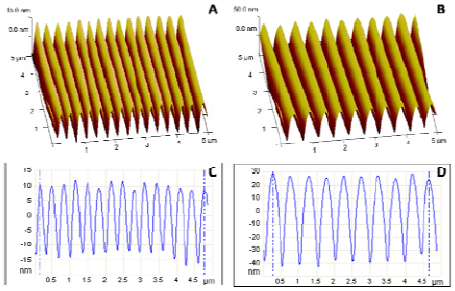

Figure S1. AFM 3D topographic maps from the height images (A,B) and height profiles (C,D) for wrinkled PDMS stamp after an exposure time of 50 and 150 s to the oxygen plasma.

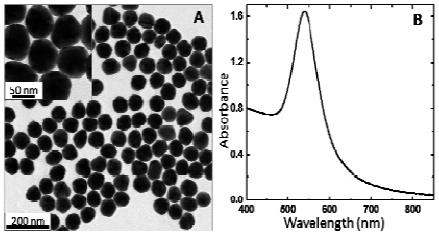

Figure S2. TEM micrograph (A) and UV-vis-NIR spectrum of the employed 66 nm gold nanoparticle colloid.

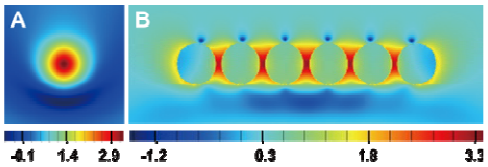

Figure S3. Electric field intensity enhancement contours at a logarithmic scale for a single-line Au nanoparticle array. The nanoparticle array consists of six nanoparticles which are linearly aligned in a row with a gap distance of 8 nm. The diameter of the nanoparticles is 66 nm. Projections are shown in the yz plane (A) and xz plane (B) of the Au nanoparticles array. The mesh size is 1 nm.

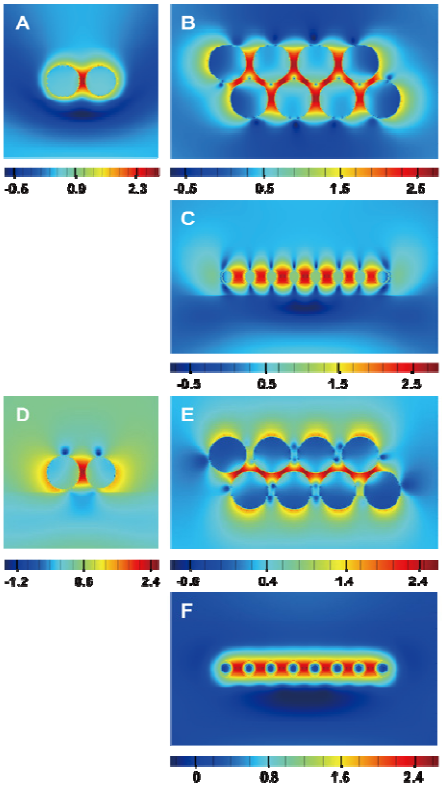

Figure S4. Electric field intensity enhancement contours at a logarithmic scale for a double-line Au nanoparticle array. The array consists of eight nanoparticles linearly aligned in two alternate rows with a closest gap distance of 8 nm. (A-C) yz, xy, and xz projections of E-field enhancement maps for the double-line array, with excitation polarization in the x direction. (D-F) yz, xy, and xz projections of E-field enhancement maps for excitation polarization in the y direction.

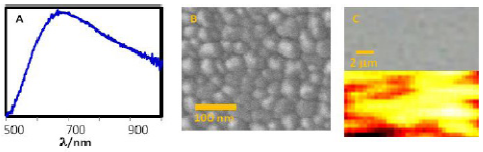

Figure S5. Vis-NIR spectrum (A), SEM image (B), and optical and SERS imaging of a 9 nm gold island film

Notes and references

1. J. Rodriguez Fernandez, J. Perez Juste, F. J. Garcia de Abajo and L. M. Liz Marzan, *Langmuir*, 2006, **22**, 7007 7010.
2. M. Pretzl, A. Schweikart, C. Hanske, A. Chiche, U. Zettl, A. Horn, A. Boker and A. Fery, *Langmuir*, 2008, **24**, 12748-12753.
3. A. Schweikart and A. Fery, *Microchim Acta*, 2009, **165**, 249-263.
4. J. Genzer and K. Efimenko, *Science*, 2000, **290**, 2130-2133.
5. D. B. H. Chua, H. T. Ng and S. F. Y. Li, *Applied Physics Letters*, 2000, **76**, 721-723.
6. W. Kern and D. A. Puotinen, *RCA Rewiew*, 1970, **31**, 187.
7. P. B. Johnson and R. W. Christy, *Phys. Rev. B*, 1972, **6**, 4370-4379.

Chapter 9 Controlling inter-Nanoparticle Coupling by Wrinkle-Assisted Assembly

Soft Matter

www.rsc.org/softmatter Volume 7 | Number 9 | 7 May 2011 | Pages 4073–4516

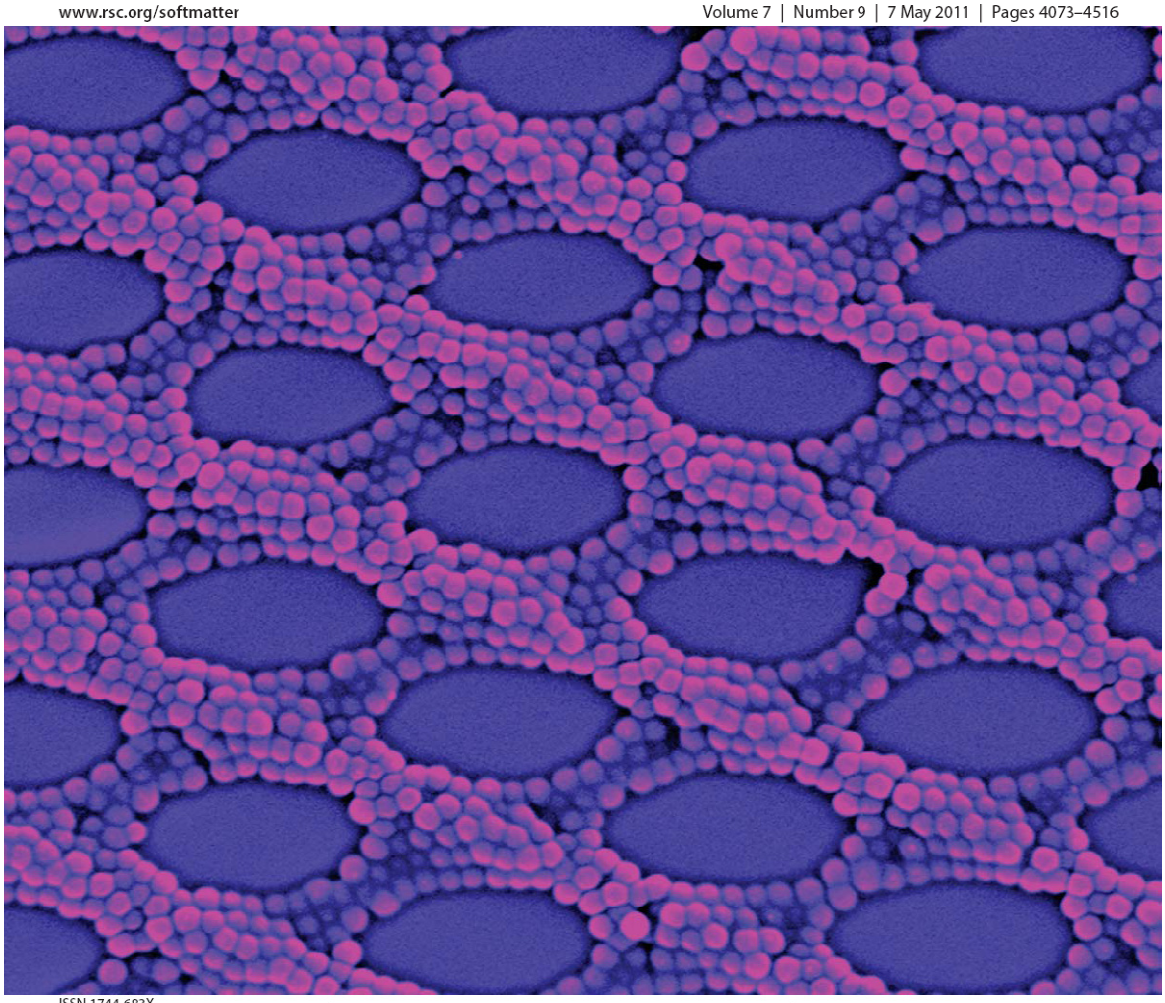

ISSN 1744-683X

RSC Publishing

HIGHLIGHT
Fery *et al.*
Controlling inter-nanoparticle coupling by wrinkle-assisted assembly

Soft Matter

Dynamic Article Links

Cite this: *Soft Matter*, 2011, **7**, 4093

www.rsc.org/softmatter

HIGHLIGHT

Controlling inter-nanoparticle coupling by wrinkle-assisted assembly

Alexandra Schweikart,[a] Nicolás Pazos-Pérez,[a] Ramón A. Alvarez-Puebla[b] and Andreas Fery*[a]

DOI: 10.1039/c0sm01359e

This highlight focuses on recent advances in controlling inter-nanoparticle coupling effects by template-assisted organization of colloidal particles. We show that the use of templates formed by wrinkling allows circumventing drawbacks of classical lithographic approaches for template formation like the large number of processing steps and poor scalability. Subsequently, we illustrate that confinement effects can be used for creating particle assemblies with excellent short and long range order. This allows controlling inter-particle coupling effects. As an example, we focus on plasmonic coupling in gold nanoparticle arrays. We demonstrate that these arrays can be applied to develop efficient and homogenous substrates for surface enhanced Raman scattering (SERS).

1 Introduction

The enormous progress in the preparation of highly monodisperse nanoparticles of different shapes, sizes and materials has made considering their large scale assembly possible.[1–8] The organization of nanoparticles into ordered or even hierarchical structures is one of the current challenges in nanotechnology. Many novel electronic, optic, mechanic or magnetic properties arise only in such assemblies where inter-particle coupling or long range cooperative behavior can be tailored by a controlled short and/or long range order. Typical examples are structures with meta-material properties or controlled plasmonic properties.[9–18]

In general, a large variety of techniques have been developed in order to accomplish these aims, see ref. 19 for a recent review. Amongst those, the use of templating surfaces, although efficient for creating complex assemblies in 1D, 2D or (partially) 3D, is often considered to be of "limited scalability" with a "very high complexity/cost".[19] These drawbacks are to a large degree connected with the use of lithographically manufactured templates.[14,17,20–30] In this highlight, we focus on the use of wrinkled template patterns which overcomes some of these problems. We discuss the physical mechanisms involved in particle assembly in these substrates. As an application example, the use of gold nanoparticle-arrays for surface-enhanced Raman scattering (SERS) sensing will be introduced.[5]

2 Topographical patterning of substrates by controlled wrinkling

Wrinkles with well-defined wavelength can be produced by coating an elastomeric material with a thin hard layer and exposing the system to strain.[31] This effect provides a versatile approach for structuring surfaces on the micron or submicron level. It typically requires few processing steps and allows for good scalability: applications of this surface instability for topographical patterning have been frequently reported, including tunable optical phase gratings[32] or microfluidic sieves.[33]

Wrinkling is in this case caused by a well-known buckling instability.[31,34,35] This has been already theoretically described as a stress-driven phenomenon by using the classical Euler buckling of an elastic column.[36–38] Depending on the type of constraints, the elastic energy is minimized by the fundamental buckling mode. For most systems currently used, a thin elastic film is bonded to a thick elastic substrate. In this case, the buckling instability is constrained by the substrate. Buckling or wrinkling of the film requires continuous deformation of the substrate while delaminating of the film is avoided. Given these conditions, substrates structured by wrinkling can be infinite in size. Energetic analysis provides the critical stress ε_c required to observe wrinkling.[34,37]

$$\varepsilon_c = \sqrt[3]{\frac{3E_s\left(1-\nu_f^2\right)}{8E_f\left(1-\nu_s^2\right)}}, \quad (1)$$

where E_f and E_s are the Young's moduli for the film and the substrate, respectively. Thus, according to Jiang and coworkers,[38] the wavelength λ and amplitude A of a wrinkled pattern can be described as

$$\lambda = \frac{\lambda_c}{(1+\varepsilon)(1+5\varepsilon(1+\varepsilon)/32)^{1/3}}, \quad (2)$$

[a]*Physical Chemistry Department, University of Bayreuth, 95445, Bayreuth, Germany. E-mail: andreas.fery@uni-bayreuth.de; Fax: +49 (0)921552059*

[b]*Departamento de Química Física, Unidad Asociada CSIC-Universidade de Vigo, 36310, Vigo, Spain. E-mail: ramon.alvarez@uvigo.es*

and

$$A = \frac{A_c}{\sqrt{1+\varepsilon(1+5\varepsilon(1+\varepsilon)/32)^{1/3}}}. \quad (3)$$

This model assumes a non-linear strain–displacement relation in the film (as well as in the substrate) and describes the stress–strain relation in the substrate by the non-linear neo-Hookean law. Importantly, the initial strain free (or stress free) state for the film and substrate is different as the film is free of forces when mounted onto the strained substrate, while the substrate is free of strain after releasing the stress.

However, for low values of the strain ε, the wavelength λ and the amplitude A approximate:

$$\lambda_c = 2\pi h \sqrt[3]{\frac{E_f\left(1-\nu_s^2\right)}{3E_S\left(1-\nu_f^2\right)}}, \quad (4)$$

and

$$A_c = h\sqrt[3]{\frac{\varepsilon}{\varepsilon_c}-1}. \quad (5)$$

The nature of the strain field plays a dramatic role for the type of the resulting topology. Wrinkles typically are oriented perpendicular to the axis of principal compressive strain. Fig. 1 summarizes the most common strain fields induced to pattern surfaces as reported elsewhere. In the simplest case of an isotropic strain field, disordered wavy structures appear as reported by Whitesides and others.[32,39,40] Such strain fields can be induced by thermal expansion and subsequent cooling of a thermoresponsive flexible material coated with a thin metal film in the expanded state. Anisotropic strain fields can be either single or multiaxial. Single-axial strain fields are known to yield line topologies; biaxial strain fields render chevrons topologies.[41,42] Localized strains will result in spoke-like patterns or target-like radial patterns.[43–45] More complex patterns with different levels of hierarchy, such as checkerboards, may be as well prepared from prepatterned surfaces exposed to a second strain field.[46]

Besides the strain field, another source of diversity arises from the variety of materials' properties, namely elastic constants of substrate E_s and thin film E_f. Controlled wrinkling requires a substrate much thicker than the film with a mismatch in the elastic constants E_s and E_f ($E_f \gg E_s$). Materials which are reversibly deformable are requested as a supporting material whereas the hard film has to be homogenous in thickness and composition to provide uniformity.

In experimental work, these requirements have been satisfied by a variety of systems: as a hard film, silica-like layers induced by oxidation are classically used[31] but also metals,[39] polymers[47]and polyelectrolyte multilayer[48,49] have been considered as well as hybrid materials containing nanoparticles and biomolecules.[50,51] Different groups showed, how thermal wrinkling can be induced by heating a polymer above its glass transition temperature (T_g) inside an additional confining geometry.[52,53] Most of the literature, in fact, employ an elastomeric support (*e.g.* poly(dimethyl siloxane), PDMS) as base for the film to be structured by wrinkling.

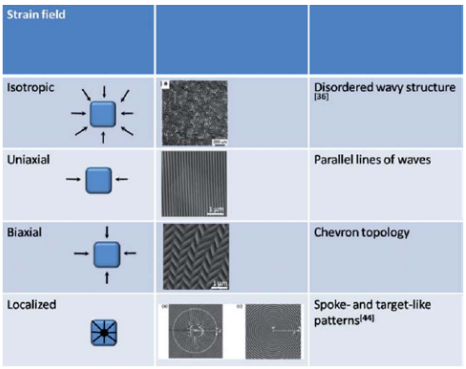

Fig. 1 Examples for common strain fields applied upon wrinkling and corresponding microscopy images of the resulting pattern (reproduced with permission from ref. 36 and 44).

3 Self-assembly of colloidal particles by template assistance

Relief structures on substrates can be used to guide the self-assembly of particles by physical constraints.[54–58] Recent reviews by Koh,[14] by Sun and Yang[17] and also by Velev and Gupta[19] focus on strategies for controlled placement of nanoscale building blocks using mainly templates created by lithographic techniques. Different driving forces for assembly processes are reported, among which the most promising are capillary forces, shear flow, electrostatic forces and electric fields.[59–62]

In recent work we have shown that wrinkles can be used to pattern nanoparticles out of suspensions in a similar fashion: nanoparticles can either be assembled directly in wrinkles or these wrinkled templates can be used to assist structure formation on flat surfaces by means of printing or confinement.

In the first case, dip- or spin-coating have been applied. In both procedures, it is crucial to match the wavelength and amplitude of the wrinkled template with the particle dimensions.[63] To avoid random particle attachment, interactions between particles and substrate should be repulsive. If this is the case, particles are driven to assemble in the wrinkles' grooves by capillary forces upon drying. Thus, dense lines of particles are formed. These lines represent one- and two-dimensional colloidal crystals with tunable spacing between the lines according to the periodicity of the wrinkled template (Fig. 2). In this specific example, wrinkles were induced in a thin layer of polyelectrolyte multilayer (PEM) by a stretch–retraction process. This process deformed the PEM plastically and wrinkling occurred consequently. The advantages of using PEM as support for the particle assemblies are feasible periodicities between 1.5 μm and 15 μm and also subsequent annealing of PEM in H_2O as water acts as a plasticizer and

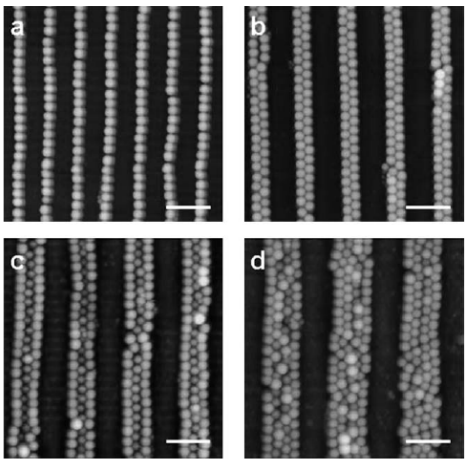

Fig. 2 AFM images of selective deposition of 380 nm sized colloidal particles on PEM wrinkled films with different periodicities. Scale bars = 2 μm; height scales = 910 (a), 860 (b), 680 (c), and 1020 nm (d), respectively (reproduced with permission from ref. 63).

interpenetrates the polymer chains. Nevertheless, dip-coating is a rather slow assembly method done at retraction speeds as slow as 10 μm s^{-1}. Horn and coworkers showed, however, how a faster spin coating experiment can trap rod-like bionanoparticles (Tobacco Mosaic Virus) into grooves of wrinkled substrates.[64] The use of radial forces to guide the assembly process reduces the parameters for successful selective coverage of the wrinkled surface. Appropriate wetting of the surface as well as the height of a liquid film spin cast onto the substrate is important. The height of the liquid film can be selected by the spin speed. If the height exceeds the amplitude of the wrinkles, no selectivity will be observed.

If it is smaller or comparable to this amplitude, rolls of liquid are formed in the wrinkle grooves. Suspended particles will consequently assemble as the liquid in the channels evaporates. In both cases—spin coating and dip coating—the particles are trapped inside the wrinkled structure. In some cases, however, it is desirable to create particle patterns on flat substrates. The use of wrinkled substrates for micron contact printing processes has already been demonstrated.[65] In this case, material is transferred from the elevated parts of the wrinkled structure onto the substrate. Printing processes can, however, be as well used to transfer particles from the grooves onto a flat substrate: Hyun and coworkers demonstrated that particles assembled in wrinkles, in a similar process as described above, can be transferred onto flat substrates by a printing process.[66] Horn and coworkers modified the process for patterning of bionanoparticles.[67]

All these processes consist of two steps: an assembly step at first followed by a printing step. We have recently introduced wrinkle confined drying as a one-step process:[68] a suspension containing nanoparticles is confined between a wrinkled substrate and a flat surface (hydrophilized glass). If the liquid wets the surfaces of the adjacent walls, the resulting channels are filled with nanoparticle suspension. The system is subsequently left to dry and the wrinkled substrate is removed.

The area where particles are assembled on the glass substrate is comparable to the area where the substrate is structured by wrinkling as can be seen from the boundary of the particular color (Fig. 3A and B). The difference in interference colors indicates different (colloidal) periodicities.

In these experiments, the spacing between the particle lines can be tuned by varying the wavelength of the wrinkles. We found that the periodicity of the colloidal structures matches the wrinkles' periodicity. Scanning electron microscopy was carried out to analyze the structures (Fig. 3C–G, left column). However, much more surprisingly, we found that very different patterns can be created from the same stamp when using solutions of different particle concentrations. At low volume fractions single lines of particles (Fig. 3C) are observed. When the particle concentration increases particles organize into double lines (Fig. 3D). Further, three dimensional pyramidal superstructures with different particle densities can as well be obtained and controlled by an additional increase of the volume fraction (Fig. 3E–G).

Monte Carlo simulations using hard spheres with similar geometrical parameters to those used in the experiments confirmed that packing effects of the confined particles play a dominant role in the assembly mechanism.[70,71] Fig. 3 (middle and right column) displays the corresponding simulation results.

More complex, grid-like structures appear after confining the colloidal suspension between two wrinkled surfaces with crossed orientation. Again, the corresponding simulation fitted well with the experimental observations for crossing two stamps at 90° or 45° angle (Fig. 4).

4 Towards applications: case study SERS substrates

In the following we will—amongst the many areas mentioned in the Introduction—focus on the application of ordered metal nanoparticles for surface enhanced Raman scattering spectroscopy. While the applicability of the approach is by far not limited to this particular area, it can serve as a case study.

Metallic nanoparticles can give rise to localized surface plasmon resonances (LSPRs). The interaction of LSPR with analytes can be used to boost the efficiency of analytical techniques. This principle is exploited in a new family of ultrasensitive analytical techniques, the so-called surface-enhanced spectroscopies.[72] Among this family of techniques that include the surface-enhanced fluorescence (SEF), surface-enhanced infrared absorption (SEIRA) and the surface-enhanced Raman scattering

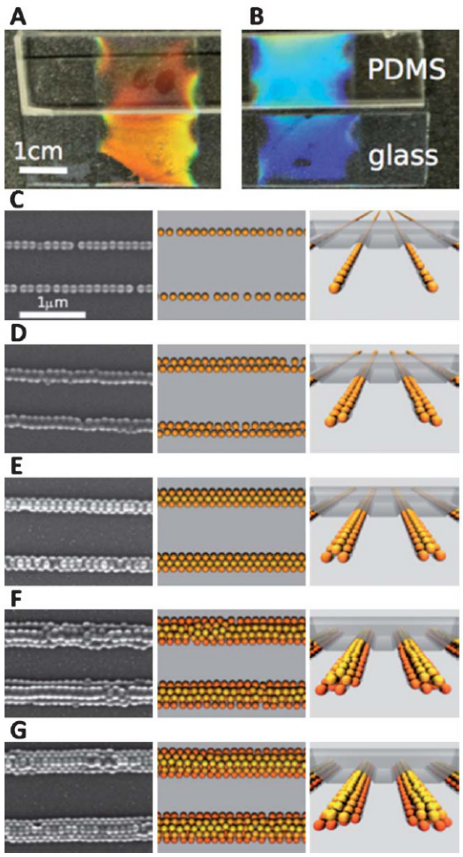

Fig. 3 Digital camera pictures (A and B) of wrinkled PDMS stamps. The different iridescent colours in (A) and (B) stem from periodically structured features of the surface with different wavelengths (956 nm and 765 nm, respectively). (C–G) show sequence of structures found experimentally with SEM (left column) and in simulations, shown from the top (middle column) and along the channels (right column). The concentration increases from (C) to (G), leading to structures that range from single-file wires to prisms with triangular cross-section. The transparent grey shape represents the sinusoidal wall and is shown only partially for clarity (reproduced with permission from ref. 69).

(SERS) spectroscopy, SERS is by far the most attractive tool as it puts together the possibility of ultrasensitive detection, down to the single molecule, in a single data set that includes all the structural characteristics of the molecular system under study (*i.e.* the vibrational spectra). Further, SERS analysis can be carried out under environmental and biological conditions of pressure and temperature and in complex samples without any previous separation.[73]

However, SERS ultradetection is typically performed on nanostructured metal surfaces, where plasmon hot-spots (regions where the interaction of the electromagnetic field of two or more nanoparticles is extremely high) are generated. The main problem is that in most SERS platforms these hot spots are often randomly distributed and little is known about the precise geometry or number in a given illuminated area of the plasmonic substrate. This prevents accurate, quantitative SERS analysis.

Recent attempts to produce quantitative, high-yield SERS have relied on optical field concentration at the gaps between aggregated particles,[74] but these systems are typically difficult to control, and their reproducibility is ruined by inescapable finite distributions of particle sizes and gap widths.[75] Other imaginative approaches using plasmon standing waves[76] and Wood anomalies in gratings[77] sacrifice the maximum achievable enhancement to gain controllability in return. On the other hand, tipped nanoparticles had been used as well as single-particle hot spots due to their inherent capacity for concentrating light at the apex of their tips.[7,78] A wide variety of substrates have been designed to optimize the necessary metallic nanostructures so that high electromagnetic fields can be obtained as required to enhance the Raman signal.[79–81] Besides the popular gold or silver island films, obtained by physical vapor deposition,[82] a number of other interesting methods such as layer-by-layer (LbL) assembly, electron beam lithography (EBL), nanoimprint lithography (NIL), 3D porous structures loaded with particles,[83,84] or nanoparticle self-assembly have been widely reported to provide high enhancing fields which can even lead to single molecule detection,[79–81,85] but which solve the problem of reproducibility of the signal intensity.

Still portable, quantitative, and highly active at-large platforms for conventional SERS analysis are required. Organization of pre-synthesized colloidal nanoparticles using modern TASA technique appears as a viable alternative to existing approaches. We have recently applied the wrinkle-confined drying approach which was introduced in Section 3 for patterned deposition of gold nanoparticles.

A critical parameter in this process is the size and shape monodispersity of the particles in the colloid, which can be readily achieved for various morphologies, in particular using controlled seeded growth.[86–89] The latter is a key factor toward reproducibility of the intensity as the homogeneous distribution of the electric field should give rise to homogeneous hot spots regardless of the

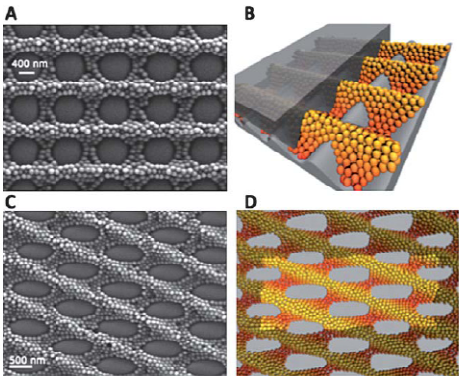

Fig. 4 (A) SEM image of a dried colloidal suspension that was confined between two crossed wrinkled stamps. (B) Perspective view of a simulation configuration of hard spheres confined between two sinusoidal walls with crossed orientations. Half of the upper wall is cut away for clarity. (C) As in (A) but for two stamps that were crossed by an angle of 45°. (D) Top view of the simulation configuration corresponding to (C). Particles that belong to periodic images are shaded grey. Note the chiral nature of the structure in (C) and (D); this cannot be transformed by rotations and translations only into its chiral partner with a crossing angle of −45° (reproduced with permission from ref. 69).

precise volumes of the particles that are interacting in each particular probe site. Fig. 5 shows representative SEM micrographs of the materials obtained upon confined drying gold nanospheres in parallel lines. Detailed SEM analysis indicated that the average interparticle distance is 8 nm for both samples, which is consistent with the values for CTAB stabilized colloids reported in the literature.[90] As expected, the optical properties (determined as scattering intensity from uniform regions using a dark field microspectroscopy setup) are deeply affected by the details of the arrangement within each assembly. In both samples, the LSPR was found to be red-shifted with respect to the dilute gold colloid, as a consequence of plasmon coupling due to interactions between the electromagnetic fields of neighbouring particles.[91] Interestingly, there are no significant differences between them, with maxima at 593 and 601 nm for the single-line and double-line arrays, respectively, though the double-line array yields a wider scattering band. Aggregation is well known to promote the formation of hot spots where high electromagnetic fields arise.[92–94] LSPR modeling by means of the finite-difference time-domain (FDTD) method shows an extremely good agreement with the experimental values (Fig. 5). Near field enhancement profiles, plotted at their corresponding LSPR maximum wavelengths, reveal that the electromagnetic field within the particle arrays is unevenly distributed, with significant enhancements precisely located at the gaps between nanoparticles, generating strong hot spots, in full agreement with the electromagnetic model in SERS.[95] On the basis of the registered LSPR bands for the nanostructured substrates, the optical enhancing properties were tested using a laser excitation wavelength of 633 nm, upon exposure of the substrates to a common SERS probe, benzenethiol (BT). Fig. 6 shows the SERS mappings obtained for the single-line array and the gold island film. For single and double lines, the SERS spectrum of BT could be readily acquired from all points in the image. Further, in both cases the intensity of the SERS signal was highly uniform, in strong contrast to that obtained for the gold island film used as an analytical blank (Fig. 6B). The normalized enhancement by the single-line and double-line arrays is respectively three-fold and two-fold larger than that for an ideal island film. Additionally, this result suggests that the interaction resulting

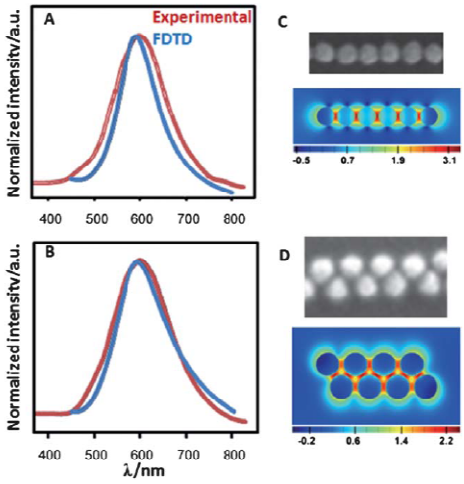

Fig. 5 (A and B) Normalized experimental and calculated localized surface plasmon resonance bands for single-line (A) and double-line (B) arrays of particles. Electric field intensity enhancement contours at a logarithmic scale for a single-line (C) Au nanoparticle array (excitation polarization along the *x* axis; mesh size 1 nm) and double-line (D) Au nanoparticle array (the profile was averaged over excitation polarizations at 0, 90, −58, and 58 degrees referred to the *x* axis; mesh size is 1.5 nm; contours are plotted in the *x*–*y* plane) (reproduced with permission from ref. 5).

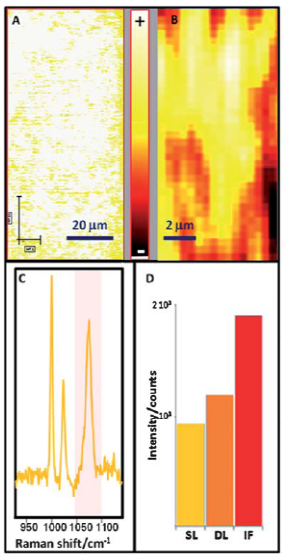

Fig. 6 (A) SERS mapping of a single-line imprinted film over a large area (λ_{ex}: 633 nm; normalized intensity at 1072 cm^{-1}; 105 × 45 μm^2, step size 200 and 500 nm for x and y, respectively, with a total of 47 250 spectra). (B) SERS mapping of 9 nm gold island film used for comparison. (C) Representative SERS spectrum of benzenethiol. (D) Intensities for single, double lines and islands film. Scale bar is the same for all the SERS maps (reproduced with permission from ref. 5).

from order within a line is considerably more efficient than that created by the same particles ordered in a plane, in very good agreement with the electric field enhancement values estimated from FDTD. Fig. 5C and D show that, whereas in both conformations hot spots are created at the gaps between particles, the electromagnetic field generated by the single line array is up to one order of magnitude larger than that created by the double line array. This concept becomes particularly important in ultrasensitive analysis since by simply decreasing the amount of nanostructured optical enhancer the detection limit will be increased because the formation of a monolayer will require a lower amount of analyte.[96] An additional demonstration of the homogenous intensity provided by the substrate over a large area of the single-line array clearly demonstrate that with this assembly method it is possible to control the organization of the colloidal particles on the substrate, with a consequent control over the formation of hot spots and the resulting SERS intensity, thus paving the road for the large scale development of highly sensitive quantitative platforms, which have remained elusive so far.

5 Conclusions and outlook

We have highlighted recent developments in the area of template assisted assembly of nanoparticles. We focused on the application of templates formed by controlled mechanical instabilities (wrinkling). This approach provides a simple and cost-effective solution for template formation with good scalability, while sub-micron periodicities are standardized. Recent results demonstrate that a broad variety of nanoparticle patterns is formed using these templates and that confinement effects play a dominating role in the development of the final structure. We demonstrated how simple macroscopic control parameters like (bulk) particle concentration can be used to fine-tune the structure of nanoparticle assemblies. As a first example, which allows taking advantage of this structural control for applications, we have introduced the use of gold-nanoparticle patterns as substrates for Surface enhanced Raman Spectroscopy (SERS). Here, wrinkle assisted nanoparticle assembly allowed controlling plasmonic properties of the resulting patterns. In contrast to existing approaches, enhancement factors for SERS turned out to be highly homogenous. This is a result of the high monodispersity of the used gold nanoparticles and of the lateral homogeneity of the patterns.

The potential of the approach goes of course beyond the specific example highlighted here. As mentioned in the Introduction, there is high demand for approaches that allow for controlling inter-nanoparticle coupling in many areas of optics and electronics. Still, features and shortcomings of the particular approach can be discussed well using this example. Wrinkling as lithography-free template formation has the potential of massively reducing the cost and complexity of template assisted nanoparticle assembly. Macroscopic sizes of these substrates are within reach. Still, lithographical approaches offer a broader variety of pattern shapes. More complex deformation scenarios or the use of patterned/mechanically anisotropic substrates can relief these restrictions to a certain degree, but still the pattern versatility cannot compete with classical top-down assembly methods. As well, pattern fidelity is lower and patterns tend to have more defects. However, for a broad class of applications, where the presence of local defects is not critical, the approach is well suited. The assembly mechanisms introduced here are in general not fundamentally different from classical template assisted particle assembly. While recent work shows that in some cases structures can be predicted well considering confinement effects, the complete assembly process is governed by a complex interplay of capillary and other colloidal forces during confinement. Here we are still far from a complete understanding. For those cases in which structure formation is dominated by confinement effects, however, structures can be predicted by rather simple means. In particular, the resulting structures are largely independent from the precise chemical nature of the nanoparticles, which makes the approach rather generic.

Acknowledgements

This work was funded by the Spanish Ministerio de Ciencia e Innovacion (MAT2008-05755) and the Xunta de Galicia (08TMT008314PR). The work was supported by the German science foundation within SFB 840, TP B5.

References

1 M. Karg, I. Pastoriza-Santos, L. M. Liz-Marzan and T. Hellweg, *ChemPhysChem*, 2006, **7**, 2298–2301.
2 I. Pastoriza-Santos and L. M. Liz-Marzan, *Adv. Funct. Mater.*, 2009, **19**, 679–688.
3 N. Pazos-Perez, D. Baranov, S. Irsen, M. Hilgendorff, L. M. Liz-Marzan and M. Giersig, *Langmuir*, 2008, **24**, 9855–9860.
4 N. Pazos-Perez, Y. Gao, M. Hilgendorff, S. Irsen, J. Perez-Juste, M. Spasova, M. Farle, L. M. Liz-Marzan and M. Giersig, *Chem. Mater.*, 2007, **19**, 4415–4422.
5 N. Pazos-Perez, W. Ni, A. Schweikart, R. A. Alvarez-Puebla, A. Fery and L. M. Liz-Marzan, *Chem. Sci.*, 2010, **1**, 174–178.
6 N. Pazos-Perez, B. Rodriguez-Gonzalez, M. Hilgendorff, M. Giersig and L. M. Liz-

Marzan, *J. Mater. Chem.*, 2010, **20**, 61–64.
7 N. Pazos-Pérez, S. Barbosa, L. Rodríguez-Lorenzo, P. Aldeanueva-Potel, J. Pérez-Juste, I. Pastoriza-Santos, R. n. A. Alvarez-Puebla and L. M. Liz-Marzán, *J. Phys. Chem. Lett.*, 2010, **1**, 24–27.
8 A. Shavel and L. M. Liz-Marzan, *Phys. Chem. Chem. Phys.*, 2009, **11**, 3762–3766.
9 R. A. Alvarez-Puebla and L. M. Liz-Marzan, *Energy Environ. Sci.*, 2010, **3**, 1011–1017.
10 H. A. Atwater and A. Polman, *Nat. Mater.*, 2010, **9**, 205–213.
11 J. M. Baik, M. Zielke, M. H. Kim, K. L. Turner, A. M. Wodtke and M. Moskovits, *ACS Nano*, 2010, **4**, 3117–3122.
12 N. Engheta, *Science*, 2007, **317**, 1698–1702.
13 S. H. Ko, I. Park, H. Pan, C. P. Grigoropoulos, A. P. Pisano, C. K. Luscombe and J. M. J. Fréchet, *Nano Lett.*, 2007, **7**, 1869–1877.
14 S. J. Koh, *Nanoscale Res. Lett.*, 2007, **2**, 519–545.
15 S. Mitragotri and J. Lahann, *Nat. Mater.*, 2008, **8**, 15–23.
16 J. A. Schuller, E. S. Barnard, W. Cai, Y. C. Jun, J. S. White and M. L. Brongersma, *Nat. Mater.*, 2010, **9**, 193–204.
17 Z. Sun and B. Yang, *Nanoscale Res. Lett.*, 2006, **1**, 46–56.
18 Y. Wang, C. A. Mirkin and S.-J. Park, *ACS Nano*, 2009, **3**, 1049–1056.
19 O. D. Velev and S. Gupta, *Adv. Mater.*, 2009, **21**, 1897–1905.
20 A. Hung and S. Stupp, *Nano Lett.*, 2007, **7**, 1165–1171.
21 E. Kim, Y. N. Xia and G. M. Whitesides, *Adv. Mater.*, 1996, **8**, 245–247.
22 W. M. Lackowski, P. Ghosh and R. M. Crooks, *J. Am. Chem. Soc.*, 1999, **121**, 1419–1420.
23 B. Michel, A. Bernard, A. Bietsch, E. Delamarche, M. Geissler, D. Juncker, H. Kind, J. P. Renault, H. Rothuizen, H. Schmid, P. Schmidt-Winkel, R. Stutz and H. Wolf, *IBM J. Res. Dev.*, 2001, **45**, 697–719.
24 Y. N. Xia and G. M. Whitesides, *Annu. Rev. Mater. Sci.*, 1998, **28**, 153–184.
25 Y. D. Yin, Y. Lu, B. Gates and Y. N. Xia, *J. Am. Chem. Soc.*, 2001, **123**, 8718–8729.
26 Z. J. Hu and A. M. Jonas, *Soft Matter*, 2010, **6**, 21–28.
27 A. Kosiorek, W. Kandulski, H. Glaczynska and M. Giersig, *Small*, 2005, **1**, 439–444.
28 A. Kosiorek, W. Kandulski, P. Chudzinski, K. Kempa and M. Giersig, *Nano Lett.*, 2004, **4**, 1359–1363.
29 J. Melngailis, *J. Vac. Sci. Technol., B: Microelectron. Process. Phenom.*, 1987, **5**, 469–495.
30 D. C. Duffy, J. C. McDonald, O. J. A. Schueller and G. M. Whitesides, *Anal. Chem.*, 1998, **70**, 4974–4984.
31 J. Genzer and J. Groenewold, *Soft Matter*, 2006, **2**, 310–323.
32 N. Bowden, W. T. S. Huck, K. E. Paul and G. M. Whitesides, *Appl. Phys. Lett.*, 1999, **75**, 2557–2559.
33 K. Efimenko, M. Rackaitis, E. Manias, A. Vaziri, L. Mahadevan and J. Genzer, *Nat. Mater.*, 2005, **4**, 293–297.
34 J. Groenewold, *Phys. A (Amsterdam, Neth.)*, 2001, **298**, 32–45.
35 E. Cerda, K. Ravi-Chandar and L. Mahadevan, *Nature*, 2002, **419**, 579–580.
36 A. L. Volynskii, S. Bazhenov, O. V. Lebedeva and N. F. Bakeev, *J. Mater. Sci.*, 2000, **35**, 547–554.
37 R. Huang, *J. Mech. Phys. Solids*, 2005, **53**, 63–89.
38 H. Q. Jiang, D. Y. Khang, J. Z. Song, Y. G. Sun, Y. G. Huang and J. A. Rogers, *Proc. Natl. Acad. Sci. U. S. A.*, 2007, **104**, 15607–15612.
39 N. Bowden, S. Brittain, A. G. Evans, J. W. Hutchinson and G. M. Whitesides, *Nature*, 1998, **393**, 146–149.
40 P. Bodo and J.-E. Sundgren, *Thin Solid Films*, 1986, **136**, 147–159.
41 X. Chen and J. W. Hutchinson, *J. Appl. Mech., Trans ASME*, 2004, **71**, 597–603.
42 P. C. Lin and S. Yang, *Appl. Phys. Lett.*, 2007, **90**, 241903.
43 J. Y. Chung, A. J. Nolte and C. M. Stafford, *Adv. Mater.*, 2009, **21**, 1358–1362.
44 J. Huang, M. Juszkiewicz, W. H. de Jeu, E. Cerda, T. Emrick, N. Menon and T. P. Russell, *Science*, 2007, **317**, 650–653.
45 C. Lu, H. Möhwald and A. Fery, *Chem. Mater.*, 2008, **20**, 7052–7059.
46 A. Chiche, C. M. Stafford and J. T. Cabral, *Soft Matter*, 2008, **4**, 2360–2364.
47 C. M. Stafford, C. Harrison, K. L. Beers, A. Karim, E. J. Amis, M. R. Vanlandingham, H. C. Kim, W. Volksen, R. D. Miller and E. E. Simonyi, *Nat. Mater.*, 2004, **3**, 545–550.
48 A. J. Nolte, R. E. Cohen and M. F. Rubner, *Macromolecules*, 2006, **39**, 4841–4847.
49 A. J. Nolte, M. F. Rubner and R. E. Cohen, *Macromolecules*, 2005, **38**, 5367–5370.
50 C. Jiang, S. Singamaneni, E. Merrick and V. V. Tsukruk, *Nano Lett.*, 2006, **6**, 2254–2259.
51 C. Y. Jiang, X. Y. Wang, R. Gunawidjaja, Y. H. Lin, M. K. Gupta, D. L. Kaplan, R. R. Naik and V. V. Tsukruk, *Adv. Funct. Mater.*, 2007, **17**, 2229–2237.
52 E. P. Chan, K. A. Page, S. H. Im, D. L. Patton, R. Huang and C. M. Stafford, *Soft Matter*, 2009, **5**, 4638–4641.
53 P. J. Yoo, K. Y. Suh, S. Y. Park and H. H. Lee, *Adv. Mater.*, 2002, **14**, 1383–1387.
54 G. A. Ozin and S. M. Yang, *Adv. Funct. Mater.*, 2001, **11**, 95–104.
55 S. M. Yang, H. Miguez and G. A. Ozin, *Adv. Funct. Mater.*, 2002, **12**, 425–431.
56 Y. N. Xia, Y. D. Yin, Y. Lu and J. McLellan, *Adv. Funct. Mater.*, 2003, **13**, 907–918.
57 A. vanBlaaderen, R. Ruel and P. Wiltzius, *Nature*, 1997, **385**, 321–324.
58 X. V. Li, R. M. Cole, C. A. Milhano, P. N. Bartlett, B. F. Soares, J. J. Baumberg and C. H. de Groot, *Nanotechnology*, 2009, **20**, 285–309.
59 L. N. Donselaar, A. P. Philipse and J. Suurmond, *Langmuir*, 1997, **13**, 6018–6025.
60 N. D. Denkov, O. D. Velev, P. A. Kralchevsky, I. B. Ivanov, H. Yoshimura and K. Nagayama, *Langmuir*, 1992, **8**, 3183–3190.
61 J. C. Hulteen and R. P. Vanduyne, *J. Vac. Sci. Technol., A*, 1995, **13**, 1553–1558.
62 A. M. Kalsin, M. Fialkowski, M. Paszewski, S. K. Smoukov, K. J. M. Bishop and B. A. Grzybowski, *Science*, 2006, **312**, 420–424.
63 C. H. Lu, H. Mohwald and A. Fery, *Soft Matter*, 2007, **3**, 1530–1536.
64 A. Horn, H. G. Schoberth, S. Hiltl, A. Chiche, Q. Wang, A. Schweikart, A. Fery and A. Boker, *Faraday Discuss.*, 2009, **143**, 143–150.
65 M. Pretzl, A. Schweikart, C. Hanske, A. Chiche, U. Zettl, A. Horn, A. Boker and A. Fery, *Langmuir*, 2008, **24**, 12748–12753.
66 D. C. Hyun, G. D. Moon, E. C. Cho and U. Y. Jeong, *Adv. Funct. Mater.*, 2009, **19**, 2155–2162.
67 A. Horn, S. Hiltl, A. Fery and A. Boker, *Small*, 2010, **6**, 2122–2125.
68 A. Schweikart, A. Fortini, A. Wittemann, M. Schmidt and A. Fery, *Soft Matter*, 2010, **6**, 5860–5863.
69 A. Schweikart, A. Fortini, A. Wittemann, M. Schmidt and A. Fery, *Soft Matter*, 2010, **6**, 5860–5863.
70 A. Fortini and M. Dijkstra, *J. Phys. Condens. Matter.*, 2006, **18**, L371–L378.
71 M. Schmidt and H. Lowen, *Phys. Rev. Lett.*, 1996, **76**, 4552–4555.
72 R. F. Aroca, *Surface Enhanced Vibrational Spectroscopy*, Wiley, New York, 2006.
73 S. Abalde-Cela, P. Aldeanueva-Potel, C. Mateo-Mateo, L. Rodríguez-Lorenzo, R. A. Alvarez-Puebla and L. M. Liz-Marzán, *J. R. Soc., Interface*, 2010, **7**, S435–S450.
74 H. Xu, E. J. Bjerneld, M. Käll and L. Borjesson, *Phys. Rev. Lett.*, 1999, **83**, 4357–4360.
75 G. Braun, I. Pavel, A. R. Morrill, D. S. Seferos, G. C. Bazan, N. O. Reich and M. Moskovits, *J. Am. Chem. Soc.*, 2007, **129**, 7760–7761.
76 M. Abdelsalam, P. N. Bartlett, A. E. Russell, J. J. Baumberg, E. J. Calvo, N. s. G. Tognalli and A. Fainstein, *Langmuir*, 2008, **24**, 7018–7023.
77 A. G. Brolo, E. Arctander, R. Gordon, B. Leathem and K. L. Kavanagh, *Nano Lett.*, 2004, **4**, 2015–2018.
78 L. Rodriguez-Lorenzo, R. A. Alvarez-Puebla, I. Pastoriza-Santos, S. Mazzucco, O. Stephan, M. Kociak, L. M. Liz-Marzan and F. J. Garcia de Abajo, *J. Am. Chem. Soc.*, 2009, **131**, 4616–4618.
79 M. J. Banholzer, J. E. Millstone, L. Qin and C. A. Mirkin, *Chem. Soc. Rev.*, 2008, **37**, 885–897.
80 R. A. Tripp, R. A. Dluhy and Y. Zhao, *Nano Today*, 2008, **3**, 31–37.
81 S. Abalde-Cela, S. Ho, B. Rodriguez-Gonzalez, M. A. Correa-Duarte, R. A. Alvarez-Puebla, L. M. Liz-Marzan and N. A. Kotov, *Angew. Chem., Int. Ed.*, 2009, **48**, 5326–5329.
82 V. L. Schlegel and T. M. Cotton, *Anal. Chem.*, 1991, **63**, 241–247.
83 H. Ko, S. Chang and V. V. Tsukruk, *ACS Nano*, 2009, **3**, 181–188.

84 H. Ko and V. V. Tsukruk, *Small*, 2008, **4**, 1980–1984.
85 H. Ko, S. Singamaneni and V. V. Tsukruk, *Small*, 2008, **4**, 1576–1599.
86 L. M. Liz-Marzan, *Langmuir*, 2006, **22**, 32–41.
87 M. Grzelczak, J. Perez-Juste, P. Mulvaney and L. M. Liz-Marzan, *Chem. Soc. Rev.*, 2008, **37**, 1783–1791.
88 I. Pastoriza-Santos and L. M. Liz-Marzán, *Adv. Funct. Mater.*, 2009, **19**, 679–688.
89 C. J. Murphy, T. K. Sau, A. M. Gole, C. J. Orendorff, J. Gao, L. Gou, S. E. Hunyadi and T. Li, *J. Phys. Chem. B*, 2005, **109**, 13857–13870.
90 H. Wang, J. Kundu and N. J. Halas, *Angew. Chem., Int. Ed.*, 2007, **46**, 9040–9044.
91 T. Ung, L. M. Liz-Marzan and P. Mulvaney, *J. Phys. Chem. B*, 2001, **105**, 3441–3452.
92 L. Brus, *Acc. Chem. Res.*, 2008, **41**, 1742–1749.
93 G. Braun, I. Pavel, A. R. Morrill, D. S. Seferos, G. C. Bazan, N. O. Reich and M. Moskovits, *J. Am. Chem. Soc.*, 2007, **129**, 7760–7761.
94 J. M. Baik, S. J. Lee and M. Moskovits, *Nano Lett.*, 2009, **9**, 672–676.
95 M. Moskovits, *J. Raman Spectrosc.*, 2005, **36**, 485–496.
96 M. Spuch-Calvar, L. Rodríguez-Lorenzo, M. P. Morales, R. n. A. Álvarez-Puebla and L. M. Liz-Marzán, *J. Phys. Chem. C*, 2009, **113**, 3373–3377.

List of Publications and Patents

Pretzl, M.; Schweikart, A.; Hanske, C.; Chiche, A.; Zettl, U.; Horn, A.; Böker, A.; Fery, A., A Lithography-Free Pathway for Chemical Microstructuring of Macromolecules from Aqueous Solution Based on Wrinkling. *Langmuir* **2008,** *24*, 12748-12753.
Microchimica Acta 2009.

Horn, A.; Schoberth, H. G.; Hiltl, S.; Chiche, A.; Wang, Q.; Schweikart, A.; Fery, A.; Böker, A., Nanostructured wrinkled surfaces for templating bionanoparticles-controlling and quantifying the degree of order. *Faraday Discussions* **2009,** *143*, 143-150.

Schweikart, A.; Fery, A., Controlled wrinkling as a novel method for the fabrication of patterned surfaces. *Microchim Acta* **2009,** *165*, 249-263.

Schweikart, A.; Zimin, D.; Handge, U. A.; Bennemann, M.; Altstädt, V.; Fery, A.; Koch, K., Fabrication of Artificial Petal Sculptures by Replication of Sub-micron Surface Wrinkles. *Macromolecular Chemistry and Physics* **2010,** *211*, 259-264.

Pazos-Perez, N.; Ni, W.; Schweikart, A.; Alvarez-Puebla, R. A.; Fery, A.; Liz-Marzán, L. M., Highly uniform SERS substrates formed by wrinkle-confined drying of gold colloids. *Chemical Science* **2010,** *1*, 174-178.

Schweikart, A.; Fortini, A.; Wittemann, A.; Schmidt, M.; Fery, A., Nanoparticle assembly by confinement in wrinkles: experiment and simulations. *Soft Matter* **2010,** *6*, 5860-5863.

Schweikart, A.; Horn, A.; Böker, A.; Fery, A., Controlled Wrinkling as a Novel Method for the Fabrication of Patterned Surfaces. *Complex Macromolecular Systems I* **2010**, *227*, 75-99.

Schweikart, A.; Pazos-Perez, N.; Ni, W.; Alvarez-Puebla, R. A.; Fery, A., Controlling inter-nanoparticle coupling by wrinkle-assisted assembly. *Soft Matter*, **2011**, *7*, 4093-4100.

Schweikart, A., Fery, A.; International Patent PCT/EP2010/007400; **2010**, submitted.

Acknowledgements

Während der letzten drei Jahre, die diese Arbeit nun gereift ist hatte ich viele Helfer und Freunde, denen ich an dieser Stelle danken möchte:

Zuallererst bedanke ich mich herzlich bei meinem Betreuer und Mentor Prof. Dr. Andreas Fery, für die große Freiheit in der Forschung, die Motivation und intensive Betreuung. Ich konnte meine Dissertation kreativ gestalten und dennoch jederzeit um Rat fragen. Seine Arbeitsweise und wissenschaftliche Begeisterung haben mich stets inspiriert. Auch die Möglichkeit an zahlreichen nationalen und internationalen Konferenzen teilzunehmen hat mich begeistert und letztendlich diese Arbeit geprägt.

Bei Prof. Dr. Matthias Schmidt und Andrea Fortini bedanke ich mich für die interessanten Einblicke in die Welt der Computersimulation und die Ausdauer bei der Arbeit an unserer Veröffentlichung. Dieser Dank gilt auch Alexander Wittemann, der mich zudem gemeinsam mit Simone Wagner mit Partikeln versorgte. Für Partikel-Synthese und gute Ideen möchte ich mich auch bei Prof. Dr. Thomas Hellweg und Matthias Karg bedanken. Unseren spanischen Kooperationspartnern Ramón Alvarez-Puebla, Weihai Ni und Prof. Dr. Luis Liz-Marzán danke ich für die produktive Zusammenarbeit. Weitete Projekte entstanden zusammen mit Kerstin Koch und Michael Bennemann aus Bonn, danke dafür. Walter Zimmermann und Falko Ziebert danke ich für ihre Berechnungen und Simulationen. Denys Zimin und Ulrich Handge sowie Prof. Dr. Volker Altstädt danke ich für die Zusammenarbeit und die Bereitstellung der hydraulischen Pressen in der FAN.

Allen Mitarbeitern in der PCII möchte ich herzlich danken, angefangen bei den Bacheloranden, Diplomanden und Studienarbeitern, die mir mit ihren Abreiten im Labor sehr geholfen haben: Moritz Tebbe, Tobias Honold, Judith Fischer und Nicole Fleischmann. Nicolás Pazos-Pérez danke ich für die Partikelsynthese, Diskussionen und die gemeinsame Arbeit. Vielen Dank an die Truppe im BZKG, die die letzten drei Jahre zu einem Labor-und Büroabenteuer gemacht haben: Daniel Kluge und Johann Erath für die vielen hilfreichen Diskussionen, Melanie Pretzl, Öznur Kaftan und Christoph Hanske für Hilfe im Labor sowie Stephan Schmidt für viele gute Ideen und Gespräche. Lieben Dank an Sybille Zimmermann, das Herzstück der PCII, für all die Unterstützung und Motivation. Werner Reichstein danke ich

für die Einweisung und Hilfe am REM und die Hilfe bei vielen technischen Fragen. Markus Hund danke ich für die Hilfe am AFM.

Thank you, Jonathon Clearwater for the English proofreading.

Großen Dank ans Kletterteam, das mir immer Motivation und Halt gegeben hat, vor allem am anderen Ende des Seils: Johannes Ingrisch, Tamara Bähr, Christopher Igel, Jürgen Leonbacher, Christopher Wollnik, Thomas Bayer, Dirk Uhlig, Felix Fromm, Ralf Kaiser, Harald Pfüller, die wunderbare Steffanie Zierer und viele mehr. Danke an meinen Bruder, der mich durch seine überragenden IT-Kenntnisse vor dem sicheren Wahnsinn bei der Fertigstellung dieser Arbeit bewahren konnte.

Zuletzt danke ich meiner Lieben Familie für ihre uneingeschränkte Unterstützung in den letzten Jahren.

Danke!

Erklärung

Hiermit erkläre ich, dass ich die vorliegende Arbeit selbständig verfasst, und keine anderen als die angegebenen Quellen und Hilfsmittel benutzt habe.

Ferner erkläre ich, dass ich weder an der Universität Bayreuth noch anderweitig mit oder ohne Erfolg versucht habe, eine Dissertation einzureichen oder eine Doktorprüfung abzulegen.

Bayreuth im Januar 2011

…….

Alexandra Schweikart